UNIVERSITÀ
DEGLI STUDI
FIRENZE

Universität für Bodenkultur Wien
University of Natural Resources
and Applied Life Sciences, Vienna

Joint PhD in Civil and Environmental Engineering

University of Florence
CYCLE XXXII COORDINATOR Prof. Borri Claudio

Natural Resources and Life Sciences

University of Natural Resources and Applied Life Sciences, Vienna

Joint research doctoral thesis
University of Florence
University of Natural Resources and Applied Life Sciences, Vienna

The root reinforcement in a distributed slope stability model: effects on regional-scale simulations

Doctoral Candidate

Dr. Masi Elena Benedetta

Supervisors

Prof. Caporali Enrica

Prof. Wu Wei

Prof. Catani Filippo

Prof. Salciarini Diana

Coordinator

Prof. Borri Claudio

Years 2016/2019

Table of contents

Acknowledgements

Firstly, I would like to express my sincere gratitude to my advisors Prof. Enrica Caporali, Prof Wei Wu, Prof. Filippo Catani and Prof Diana Salciarini for their support during my doctoral path. I am very grateful to them to have shared their in-depth knowledge and experience, which were inspirational for my studies and researches.

Warm and heartfelt thanks go to Prof. Veronica Tofani and Ph.D. Guglielmo Rossi for closely following the research and discussing from time to time about the path to take.

I thank my office mates for making even the most demanding deadlines enjoyable.

I would like to thank Fabio, for understanding my “head” absence of the latest period, telling him that I will come back to myself. One day. Maybe.

And, last but not least, I would like to thank my family for having always respected and supported my choices, even when they weren't entirely convinced to.

1 Abstract

The shallow landslides are hazardous mass movements commonly triggered by intense rainfall. The hazardousness of these events is mainly due to their common evolution in rapid mass movements as debris avalanches and flows and to the frequently occurring in the form of clusters of events. Because of their characteristics, the forecasting is a particularly valuable tool to protect people and infrastructures from this kind of landslide events.

The presence of vegetation on hillslopes significantly reduces the slopes susceptibility to the shallow landslides, and the stabilising action is mainly due to the reinforcement of the soil by the roots. The spatial variation of the root reinforcement should be therefore considered in distributed slope stability analyses. However, the natural variability of the parameter makes it challenging to insert the root reinforcement into the models.

Many approaches to the problem were tested, but nowadays there are still lacking a distributed slope stability model capable of very quick processing in which the root reinforcement is considered and an approach to estimate the root cohesion at the regional scale that it has been tested in very wide areas and for long period-simulations.

In this study, we present the effect of the root cohesion on slope stability simulations at the regional scale obtained using a physically-based distributed slope stability model, the HIRESSS (HIgh REsolution Slope Stability Simulator). The HIRESSS model was selected for the purposes, being capable of rapid processing even in wide areas thanks to the parallel structure of its code. The simulator was modified to insert the root reinforcement among the geotechnical parameters considered to computing the factor of safety in probabilistic terms, and for this purpose a commonly adopted model for the root cohesion was chosen.

To build a map of the root cohesion for the study areas, the distribution of plant species in the area was obtained from vegetation distribution map and in situ surveys, then a value of root cohesion and a range of variation was defined for each plant species based on the most recent literature in this field, finally, to reproduce the natural variability, the root reinforcement was treated as variable in Monte Carlo simulations, as well as the other geotechnical parameters.

The results of the simulations for the study areas were processed and analysed in order to evaluate the effect of the root cohesion on the failure probabilities and the adopted approach to estimate the root cohesion at the regional scale. The comparative analyses carried out on the results of the simulations performed inserting or not the root reinforcement brought out little differences between the two from the point of view the failure probabilities, particularly when the saturated conditions of the soil are reached.

Based on the findings of this research, it is considered that a root cohesion model different to the one adopted is preferable in the context of the shallow landslides, in applications in which working with failure probabilities (instead of factor of safety values) is desirable, and in areas similar to the ones of the study.

2 Introduction

2.1 Problem statement

Vegetation plays a crucial role in protecting people, settlements and infrastructures from hydrogeomorphic hazards. It strongly affects mechanical and hydrological soil behaviour, particularly related to shallow landslides. The research within the framework of slopes stability has increasingly pointed towards the analysis and quantification of the influence exerted by the vegetation on the mechanisms involved in the triggering of such phenomena.

The vegetal communities have a stabilizing action in the vadose zone of the slopes, mainly due to i) the influence on soil suction by the root water uptake, ii) the reinforcement of the soil by the root network (increase of the tensile strength), iii) the anchoring of shallowest layers to the profound and eventually more stable substrates, iv) the surcharge due to weight of plant biomass (aerial part and root system) that increases normal (to the slope) stresses, v) the rainfall interception by canopy and evapotranspiration (reduction of the delivery rates of intense precipitation and lowering of the water table).

On the other hand, some effects due to the presence of vegetation have a destabilising action, as vi) the increasing of the parallel stresses due to the plant weight, vii) the transmission of bending moments by canopy through stems and roots, viii) the wedging of roots into fractures. But nonetheless, except for particular contexts, it is largely recognised that the presence of plant constitutes a mitigating element for the slope instability. In this sense, the root reinforcement (c_r, the increase of the tensile strength of soils due to the root network) is the most relevant from the mechanical point of view (Vergani et al., 2017; Gray and Sotir, 1996).

The shallow landslides are frequent mass movements widespread all over the world. They commonly start as soil slips interesting only some tens of cubic meters of terrain at the beginning of their trigger. These landslides represent one of the most hazardous landslide categories, mainly because they can evolve into rapid mass movements assuming characteristics of debris avalanches and flows. Indeed commonly, this kind of landslides highly increases their velocity moving downstream and interest rising volumes of mobilised material. Furthermore, these landslides are mainly triggered by intense rainfall, so that rarely single failures happen, rather multiple and diffused landslide events are triggered in the region hit by the rainfall. Some of the most known catastrophic regional landslide events consisted of clusters of debris avalanches and debris flows triggered by heavy rainfall. The spectrum of site conditions favourable to the shallow landslides triggering is very wide since these

kinds of mass movements can occur on slopes of very different morphology, with different vegetation cover and characterised by different land uses.

Due to the abundance of areas susceptible to these kinds of landslides and their characteristics, the scientific community based the research on two main approaches to support the administrations and civil protection agencies in the mitigation of the risk: the hazard assessment in support of the land management and the forecasting of temporal and spatial distribution of the events for warning systems. The prediction of shallow landslides is performed by means of approaches know as empirical or using physically-based slope stability model. The first category consists of statistical techniques searching functional relations between the triggering factors (as the rainfall intensity/duration) and the actual events occurred in a specific area to define warning thresholds. To the second category belong the approaches that combine hydrological models and slope stability analyses to predict hazard areas. Commonly, the stability model is based on the infinite slope model. The soil moisture dynamics is generally based on a modified version of the steady-state wetness index (Montgomery and Dietrich 1994; Pack et al. 1998; Borga et al. 2002; Arnone et al. 2011) or an approximation of the Richards equation (Iverson 2000; Baum et al. 2002; Simoni et al. 2008). Such models provide slope stability evaluations based on the Factor of Safety (FS) (e.g. Pack et al. 1998; Baum et al. 2002) or as a function of the transmissivity (seepage flow) and rainfall rate (e.g. Montgomery and Dietrich 1994; Borga et al. 2002).

The insertion of the influence of vegetation in the distributed physical models represents a significant and still open challenge for the research. The most useful application of these stability model is in the framework of forecasting and analysis on landslides in vast areas, for civil protection purposes. Plants are complex organisms that intercourse many and complex relations with the environment. So that, whatever is the particular aspect (parameter) considered among the effects of vegetation on slope stability, the spatial variability of the parameter is considerable, and its evaluation in broad areas represents a significant limit in the insertion of the vegetation influence in distributed slope stability analysis and forecasts.

2.2 The rationale of the research

The presence of vegetation on hillslopes significantly reduces the slopes susceptibility to rainfall triggered shallow landslides. The stabilising action is mainly due to the reinforcement of the soil by the roots (increase of the shear strength). The challenges associated with natural variability in root reinforcement makes it challenging to insert the root reinforcement into slope stability models,

especially when large areas are considered. Many approaches to the problem were tested, as e.g.: extrapolating an average or uniform distribution of point measurements to estimate cohesion (Montgomery and Dietrich, 1994; Pack et al., 1998); using size, geometry and distribution of the plants to estimate local minima in root strength (Roering et al., 2003; Sakals and Sidle, 2004; Cislaghi et al., 2017; Temgoua et al., 2017); relating remotely sensed metrics of vegetation to the root reinforcement (Chiang and Chang, 2011; Hwang *et al*., 2015); applying eco-hydrologic models to estimate the reinforcement at slope or regional scale (Preti *et al*., 2010; Lepore *et al*., 2013; Tron *et al*., 2014, Arnone *et al*., 2016).

The present study arises with the purpose to try to overcome two main lacks in this field: the lack of a distributed slope stability model capable of a very quick processing in which the root reinforcement is considered; an efficient approach to estimate the root cohesion that it has been tested in very wide areas and simulating long periods. The main finality is to provide increasingly efficient and accurate shallow landslides forecasting tools to the territory administrations and civil protection agencies.

Considering the importance of regional forecasting of the rainfall triggered shallow landslides, the relevant role of vegetation on slope stability and the mentioned lacks in this field, the purposes of the present research are: i) individuating a distributed slope stability model capable of supporting quick computes even in case of extensive areas and modifying the model to consider the root reinforcement patterns in regional slope stability analysis; ii) individuating an efficient approach to estimate the root reinforcement at regional scale, favouring methods applicable using already available territory information or derivable in reasonable time; iii) evaluating the effect of the insertion of the root reinforcement on the results of regional slope stability simulations of long periods, to assess the adopted approach to estimate the root reinforcement in wide areas and the eventual improvements made to the distributed slope stability model about its forecasting capabilities.

3 Shallow landslides

This study aims at shallow soil slides triggered by heavy rainfall, events known as “shallow landslides”. Shallow landslides are mass movements of small thickness (0.3–2 m) and small scar areas (Campbell, 1975; Moser and Hohensinn, 1983; Ellen, 1988, Crosta, 1998) mainly triggered by intense rainfall events. The infiltration of abundant water into the soil determines the growth of pore pressure (Sidle and Swanston, 1982) that decreases the effective normal stress and the apparent cohesion (Fredlund, 1987). Shallow landslides are therefore usually not caused by an increase in the shear stress but rather by a decrease of the effective normal stress due to increasing pore pressures (Anderson and Reimer, 1995) and the loss of apparent cohesion (Fredlund, 1987). These changes can result in the development of a failure surface within the soil layers or at the contact with the bedrock. Another destabilising cause can be the variation of the external forces system due to earthquakes, erosion or human activities.

3.1 Triggering and cinematic

Occurrence timing and distribution in the space of shallow landslides are controlled by two categories of variables: the (almost) static variables and the dynamic variables. The static variables, as soil thickness, hydrological and mechanical characteristics of bedrock and the overlying soil, topographic characteristics (elevation, slope, distribution and size of convergence and divergence areas), affect the susceptibility of slopes to failure and the spatial distribution of the mass movements. The dynamic variables, like the degree of soil saturation and the cohesion due to the partial saturation, control the landslides triggering.

Almost-static variables:

- mechanical characteristics: properties as internal friction angle and soil unit weight influence the mechanical soil strength affecting the landslide susceptibility;
- hydrological characteristics: the permeability of soil is a fundamental factor that controls surface and underground water circulation, it depends on grain size distribution of soils, sediments arrangement, rock discontinuity and porosity, soil and rocks geological history; considering the aspects directly affecting the susceptibility to failure, soil permeability strictly influences time needed to reach the saturated conditions, therefore the critical pore pressure;

– geological structure, morphology and topography: the slope gradient significantly affects the stability of soil and triggering thresholds; superficial and bedrock topography can control superficial and groundwater flows and affect moisture condition of soil (Pierson, 1980; Renau & Dietrich, 1997; Montgomery & Dietrich, 1994); a steep slope can reach instability quicker than a gentle slope, however, reaching critical pore water pressure by the rainfall infiltration is more difficult for the first because runoff and water discharge are favoured; the arrangement of the terrain layers is also crucial as the presence of one or more impermeable layers can cause a rapid saturation of the upper layers reaching the critical pore pressure (Iverson & LaHusen, 1989; Iverson et al., 1997; Iverson, 1997; Iverson et al., 2000; Takahashi, 1981).

Dynamic variables:

– water content and flow direction: initial moisture condition of soil affects slope stability and trigger timing of the movement; rise of the water table, variations in groundwater seepage or change in flow directions from recharge to discharge areas can trigger shallow landslides (Zêzere et al., 1999; Tsai & Yang, 2006; Tsai, 2008);

– cohesion: soil cohesion (both the effective and the apparent cohesion) changes with the moisture state of a soil (Krahn et al. 1989; Rahardjo et al. 1995; Rao 1996; Kim et al. 2004); regarding the effective cohesion, the dependence behaviour with water content depends on the type of soil; indeed, as silty soils dry, the cohesion decreases, as clayey soils lose water, cohesion generally increases (Krahn et al. 1989; Rahardjo et al. 1995; Rao 1996; Kim et al. 2004); drops and rises of the water table determine the presence or not of the apparent cohesion affecting the strength of soils; even if the additional soil strength due to roots (root cohesion) is generally assumed as a constant value, recent studies began to evidence that the mechanical properties of root systems are suction dependent (at least under certain conditions) (Mahannopkul and Jotisankasa, 2018).

Generally, once the failure happened this kind of landslides assume the characteristics of debris avalanches that can evolve or not into debris flows (the Varnes classification of landslide types updated by Hungr et al., 2013). Small debris flows from different sources then can group into channels (Figure 1) critically increasing mass displacement, destructive power and reaching extremely high velocity (up to 20 m/s) (Hungr et al., 2001). Typically, the mobilised soil mass increases its volume during the downward propagation, due to processes as liquefaction, dilatancy, undrained loading and erosion of the substrate (Ellen and Fleming, 1987; Ellen, 1988, Crosta, 1998; Wieczorek et al., 2000).

Debris avalanches generally start as debris slides, and the failure concerns residual, colluvial or pyroclastic terrains. Once the failure happened, undrained loading continues to interest new further downstream and laterally portions of terrain as the eroded material moves down the slope, so that a small initial landslide can involve a large segment of the slope during the successive phases. Indeed, the paths widen downslope, as the undrained loading destabilises an increasing width of the slope segment (Hungr et al., 2014).

Figure 1. The cluster of debris avalanches and debris flows of January 2010 in the Serrana Region of Brazil (Courtesy of A.L. Coelho-Netto, Federal University of Rio de Janeiro). From Hungr et al. 2013

Once and if the soil material reaches a steep channel and continues to move into it (debris flow), the bed of the invested channel becomes subject to very rapid undrained loading.

In some cases, the loading is abrupt enough that it could be characterised as impact loading (Sassa, 1985) so that even coarser material can be subjected to important increases of the pore-pressure. As the debris flow moves downstream, further soil material is increasingly added to the flow. At the end of the event, almost the entire bulk of the material involved in the debris flow usually originates from the path, while the volume coming from the initial slide is insignificant.

Debris flows behave as unsteady, nonuniform flows (e.g. Costa & Williams 1984). Coarse debris tends to accumulate at surge fronts as a result of grain-size segregation and migration processes within the flow. Cobbles and boulder move forward mostly by sliding and tumbling. The water-saturated debris behind the flow fronts is, on average, finer-grained and it moves as a liquefied mass. Levees can form where debris flows overtop channels faces. Depositional lobes form where the frictional

resistance imposed by the coarse-grained material of the flow front is high enough to halt the motion of the behind liquefied debris (Iverson, 2003). Generally, the flow begins to stop when the slope angle becomes lower than 3°. During the stopping phase, while the frontal section of the flow is slowing down, the material from the behind sections can overlay the front.

3.2 Risk and mitigation

Shallow soil failures and successive debris avalanches and flows can be triggered by rainstorms of high intensity and short duration, by prolonged rainfall of moderate-intensity or snow melting (Moser and Hohensinn, 1983; Crosta, 1998; Crosta and Frattini, 2008). Generally, in the area interested by the meteorological event, the development of clusters of this kind of landslides is frequent. These landslide events are the cause of economic losses and casualties. They damage cultivations, settlements and pose a hazard to the safety of people. Some of the most catastrophic regional landslide disasters occur as clusters of debris avalanches and debris flows during heavy rainstorms or earthquakes (another potential triggering factor).

Due to the abundance of susceptible area, the high numerousness and areal density when they happened, the high velocity of the movements, shallow soil failures and successive debris avalanches and flows are one of the most hazardous natural phenomena (Costa, 1984; Johnson and Rodine, 1984).

Considering these facts, the most efficient approaches to mitigating the shallow landslides risk are predominantly the following: the hazard assessment to direct and guide the land management and the forecasting of the temporal and spatial distribution of the events for warning systems.

4 Vegetation effects on slope stability

Vegetation plays a crucial role in slope stability, affecting soil behaviour through many hydrological and mechanical processes. At the catchment scale, the hydrological effects of interception, suction, evapotranspiration and infiltration strongly affect runoff processes, while at the local scale, the mechanical effect of root reinforcement is the leading factor for slope stability.

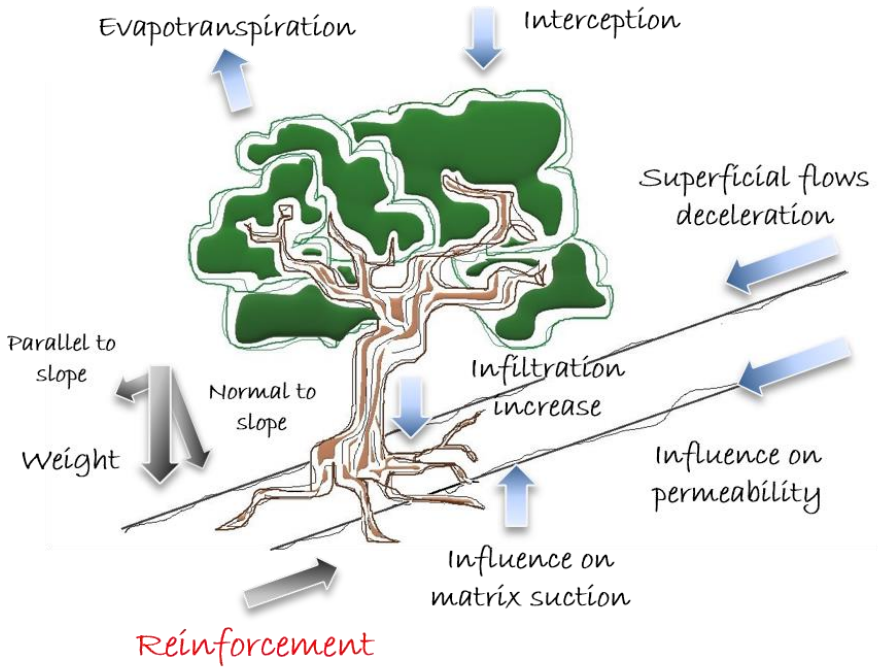

Figure 2. Mechanical and hydrological effects of vegetation affecting the slope stability.

4.1 Hydrological effects

The main hydrological effect of vegetation is the reduction of the soil moisture content, with the consequence of delaying the onset of the soil saturation levels that can trigger mass movements (Forbes and Broadhead, 2011).

The processes causing this effect are:

- interception and evaporation: these processes worked by the canopies reduce the amount of effective rainfall reaching the ground; light rainfall may be nearly all intercepted by branches and foliage, while during high-intensity rainfall, trees can intercept up to 0–5 mm (Keim and Skaugset, 2003);

- suction and transpiration: trees can reduce soil moisture levels from distances of up to three times the radius of the crown suctioning water through the root system (Gray and Sotir, 1996); in regions where precipitation consistently exceeds the potential evapotranspiration (cold temperate and subalpine climates), the reduction of the soil moisture through transpiration and evaporation is negligible, nevertheless, in case of moderate rainfall events, evapotranspiration may reduce soil moisture before the rainfall, increasing the amount of water that can be stored in the soil (Dhakal and Sidle, 2003);
- infiltration and subsurface flow: flow pipes and channels formed by root decay can help slopes to drain faster (Vergani and Graf, 2015); on the other side, root channels also increase infiltration rate and soil moisture content, raising landslide hazards.

4.2 Mechanical effects

The mechanical behaviour of soil can be affected by the following processes worked by vegetation:

- soil reinforcement by roots: root systems of plants increase the shear strength of soils through a combined action by the large and the small roots, large woody roots can anchor the superficial soil layers to more stable substrates crossing potential planes of weakness, small roots strengthen the bonds with the soil particles increasing the overall cohesion of the matrix soil-roots; the reinforcement by roots can work on the basal or lateral failure plane of a landslide or;
- buttressing and arching: roots and stems of woody vegetation can counteract downslope shear forces working as buttress piles or arch abutments (Gray and Sotir, 1996).
- surcharge: vegetation (particularly the trees) weight increases both the normal and the tangential forces acting on slope, but generally the influence on the overall stability is negligible (Selby, 1993; Stokes et al., 2008); indeed, for instance, the surcharge due to the weight of mature forest of beech is unlikely higher than 2.5 kPa, the equivalent of a layer of stony soil 15 cm thick (O'Loughlin, 1974; Dhakal, 2003).

4.3 Effects by roots

Roots play a leading role in many of the abovementioned effects. Roots indeed play control on soil properties by *i)* influencing soil suction: soil moisture is reduced by the root-water uptake that consequently induces an increase in the soil matric suction, also causing changes in the soil shear strength (Gan et al., 1988) and hydraulic conductivity (Ng and Leung, 2012); *ii)* changing soil structures, as the roots occupy the soil pore spaces (Scanlan and Hinz, 2010, Scholl et al., 2014), retain water (Taleisnik et al., 1999) and release exudates (Grayston et al., 1997, Traoré et al., 2000); *iii)* increasing soil shear strength, essentially the cohesion parameter (root reinforcement) (e.g. Gray and Sotir, 1996; Montgomery et al., 2000; Norris et al., 2005). It is worth remembering that the presence of the root induces changes in the SWRC through the process just mentioned, as the soil water retention curve (SWRC) depends on soil pore size and its distribution (Romero et al., 1999, Ng and Pang, 2000, Leung et al., 2015).

4.3.1 Root reinforcement

Soil reinforcement by roots is generally recognised as the main contribution of vegetation to slope stability. The root system represents the part of plants tasked with anchoring (among other fundamental functions) the vegetation to the soil. The combination of earth, roots and bonds forms a reinforced soil matrix in which stress can be transferred from the soil to the roots, increasing the overall strength of the matrix (Greenway, 1987). Therefore, the strength of rooted soil depends on soil strength, root strength, and strength of the bonds between soil and roots (Waldron, 1977; Waldron and Dakessian, 1981; Ennos, 1990). The strengthening effect of a matrix by fibres of different material is achieved if the two materials have different tensile and compressive strength properties (Beaudoin, 1990). In the case of the reinforced matrix soil-roots, the soil is strong in compression but weak in tension, plant roots are instead weak in compression but strong in tension. The magnitude of root reinforcement is a function of the following factors: i) root density; ii) root tensile strength; iii) root tensile modulus; iv) root length/diameter ratio; v) soil–root bond strength; alignment – angularity/straightness of the roots, and vii) orientation of the roots relative to the direction of principal strains. Experiments have shown that root tensile strengths decrease exponentially with increasing root diameter (e.g Waldron and Dakessian, 1981; Greenway, 1987; Coppin and Richards, 1990; Gray and Sotir, 1996; Genet et al., 2005; Pollen and Simon, 2005; De Baets et al., 2008; Fan and Su, 2008; Hales et al., 2009). Typical tensile strength values range from 4 to 20 MPa for grass roots and 5–70 MPa for tree roots (Coppin and Richards, 1990).

The relationship between root diameter and root tensile strength is usually best described using a power-law function of the form:

$$T_r = ad^b \qquad (1)$$

where T_r is the ultimate tensile strength (MPa), d the root diameter (mm), and a and b the regression parameters. The results from root tensile strength studies suggest that, at the smallest root diameters, grass roots have the highest tensile strength and shrubs the lowest. The tensile strengths of grass and tree species tend to converge at root diameters above 5 mm (Mao et al., 2012). For root diameters greater than 1 mm, grass roots are, however, weaker per unit area than corresponding tree and shrub species. As root reinforcement is also function of the density of roots in soils, grasses may provide significant reinforcement to the shallower layers of soil where thousands of fine grass roots are concentrated, providing significant reinforcement when potential failure planes are shallow. Conversely, the woody roots of trees and shrubs will reinforce over a greater depth of soil through a combination of both fine, fibrous roots and coarser, woody roots.

Different root diameters have a different influence on soil strengthening. During soil shearing, fine roots tend to break staying in the same position relative to the soil particles. Differently, coarse roots can be pulled out of the soil without breaking down (Ennos, 1990). A combination of dense, fine roots in the top layer (where resistance in tension is important) with coarse, deeply penetrating roots crossing potential shear surfaces is the most efficient to stabilise slopes and river banks (Reubens et al. 2007). The power relationship between tensile strength and root diameter can be explained by the scaling effect typical of the fracture mechanics and by another effect suggested by Genet et al. (2005): an additional explanation can be the different cellulose content in roots of varying diameters. Root architecture can also affect the distribution of tensile strengths in a given root network (Stokes and Mattheck, 1996). Hales et al. (2009) described a possible relation between root tensile strength and hillslope topography. Considering plants belonging to the same species, they found stronger tensile strength in plants located on convex noses of a hillslope relates to the ones located in concave hollows. The hypothesised explanation is the difference in the soil water potential of the topographic locations that is reflected in different root cellulose contents. Although a power-law relation between root diameter and tensile strength can commonly be seen for a given species at a given site, cellulose content, and thus root tensile strength, may also vary with environmental factors. These environmental factors include but are not limited to soil fertility, nutrient supply, soil moisture content, and soil mechanical factors such as bulk.

The first and most used approach to describe the reinforcement due to roots involved the use of perpendicular root models (Waldron, 1977; Wu et al., 1979) and the integration of the root

reinforcement as an additional term in the Mohr-Coulomb shear strength criterion for unsaturated soils (Fredlund et al., 1978):

$$S = c' + (\mu_a - \mu_w)\tan\varphi^b + (\sigma - \mu_a)\tan\varphi' + c_r \qquad (2)$$

where S is the soil-shearing resistance (kPa), c' the effective cohesion (kPa), μ_a the pore-air pressure (kPa), μ_w the porewater pressure (kPa), φ^b the angle describing the increase in shear strength due to a rise in matric suction (μ_a-μ_w) (°), σ the normal stress on the shear plane (kPa), φ' the effective soil friction angle (°), and c_r the increase in shear strength due to roots (kPa).

Assumptions of Waldron model (Waldron, 1977) are the vertical extension of all the roots across the horizontal shear zone and the action by the roots as loaded piles (as the soil is sheared, tension is transferred to them). In this model, the tension developed in each root is resolved into a tangential component (that increases the apparent cohesion) and a normal component (that increases the frictional resistance). The angle of each root with respect to the direction of the applied force is however important, as this determines the distribution of stresses within the root and consequently the maximum tensile strength before breaking (Niklas, 1992). Waldron (1977) model is therefore generalised to the case where roots may be oriented at any angle relative to the failure plane (Gray and Leiser, 1982):

$$c_r = T_r\left(\frac{A_r}{A}\right)[\sin(90-\psi) + \cos(90-\psi)\tan\sigma'] \qquad (3)$$

where T_r is the root failure strength (tensile, frictional, or compressive) of roots per unit area of soil (kPa), Ar/A the root area ratio(dimensionless), and ψ the angle of the root at rupture relative to the failure plane (°).

The angle of the root at rupture relative to the failure plane ψ is equal to:

$$\psi = \tan^{-1}\left(\frac{1}{\tan\theta + \frac{1}{\tan i}}\right), \qquad (4)$$

where θ is the angle of shear distortion (°) and i the initial root orientation relative to the failure plane (°). For cases where root orientation is 90°, the equation [3] is identical to the model of Waldron (1977). The use of simple perpendicular root models in cases where it may be assumed that the roots are randomly oriented in the soil is supported by Gray and Ohashi (1983): they showed that perpendicularly oriented fibres or randomly oriented fibres provided comparable reinforcement. Assuming all roots perpendicular to the failure plane, Wu et al. (1979) selected a constant value of 1.2 to replace the bracketed term (root orientation factor, R_f) and equation [3] became

$$C_r = 1.2\,T_r\left(\frac{A_r}{A}\right). \qquad (5)$$

Many researchers have explored the variability of R_f using different assumptions for σ' and θ: values selected by most authors have tended to be within the range of 1.0–1.2. Based on their studies, Pollen-Bankhead (2010) found that 1.0 is more appropriate than 1.2.

This theoretically based model allows rooting strength to be estimated based on the proportion of the soil area occupied by roots and measurements of the tensile strength of the roots themselves. The model is subject to the assumptions of limit equilibrium analysis, including the following: (1) shear deformation along the slip surface is restricted to a narrow zone; (2) roots of different size classes are flexible and linearly elastic with Young's modulus E; (3) roots are oriented perpendicular to the failure plane; (4) the full tensile strength of all roots is mobilized; (5) roots are well anchored and do not pull out when tensioned; and (6) the internal friction angle (φ) is unaffected by roots (Waldron and Dakessian, 1981; Greenway, 1987; Phillips and Watson, 1994). Model by Wu et al. (1979) tends to overestimate root reinforcement due to the assumptions of full tensile strength of each root mobilized during the soil shearing and the simultaneous breaking of all roots (Waldron and Dakessian, 1981; Greenway, 1987; Pollen et al., 2004; De Baets et al., 2008; Operstein and Frydman, 2000; Docker and Hubble, 2008). To solve this overestimation, Pollen and Simon (2005) and Pollen (2007) proposed the fibre-bundle model (FBM) (RipRoot) to consider the progressive root breaking during shear failure. This model used the measured diameters and tensile strengths of roots crossing the shear plane and the constant R_f of 1.2 used by Wu et al. (1979). The root reinforcement estimated using RipRoot (C_r) was then substituted into equation [2].

Pollen and Simon (2005) and Docker and Hubble (2008) observed that the magnitude of overestimation by equation [5] was species-specific: the simplified model of Wu et al. (1979) tended to provide better predictions for grasses. Schwarz et al. (2010b) applied an FBM approach to modelling of root reinforcement on slope stability in Tuscany, Italy: they confirmed that the Wu model overestimated root reinforcement and, therefore, over-predicted slope factor of safety by up to 10%, with this error increasing exponentially for smaller landslides (Schwarz et al., 2010b).

4.4 Methods of studying root systems

Nowadays a significant limit persists in properly including the root reinforcement effect in slope stability models, consisting of the difficulties to assess the spatial variations of the root density in soils. Several methods to quantitatively study the roots systems have been experimented and used, but they are highly time-consuming and, concerning the most advanced techniques, extremely expensive.

Commonly used methods to determine root density are the excavation of roots systems, the trench profile wall method and techniques based on samples washing for the separation from soils of

roots and the detection of the latter (Böhm, 1979). The extraction of soil samples and the successive separation of roots through washing and sieving (the most used method) determines the loss of considerable amounts of roots during its phases (Subedi et al., 2006).

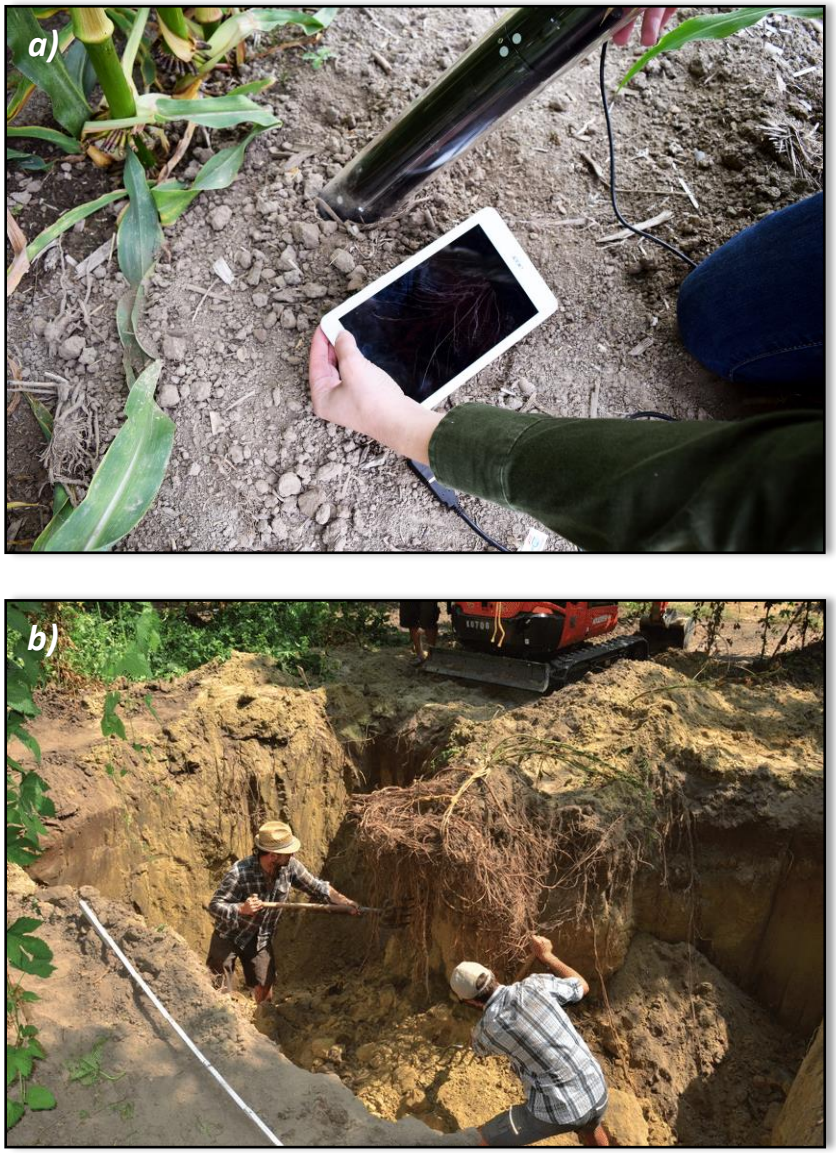

Figure 3. Methods to study roots system in situ. a) minirhizotron; b) roots excavation.

In the last decades, new techniques have been developed such as automated imaging analyses (Dowdy et al., 1998; Costa et al., 2000), portable minirhizotrons (transparent pipes slantwise inserted in soils, within which video-photo cameras are dropped), colour scanner systems (Pan et al., 1998). However, these techniques are still expensive, quite difficult to be managed and have not always proved to be completely reliable.

5 Forecasting models

As mentioned above, shallow landslides are unexpected and extremely dangerous events, so that forecasts to support warning systems are very useful tools to prevent fatalities in case of high-intensity rainfall events. A warning system that can run in real-time providing a reliable threat forecasting system for these landslides is one of the most desirable. Even if these types of landslides are more frequent in areas with specific combinations of morphologic and lithologic terrain characteristics, they can potentially trigger in every slope with soil. The combinations of parameters that can trigger shallow landslides are potentially infinite so that simplifying the problem is inevitable. The point is to find the best compromise between computational speed and reliability. Rapidity and reliability substantially depend on the adopted model for the triggering phases. There are two kinds of models to forecast the landslides triggering: statistical-empirical models and deterministic models.

5.1 Statistical-empirical models (or black-box models)

These models are based on an approach in which the physical processes involved in the landslide triggering are ignored, and a functional empirical correlation is searched between the primary cause (rainfall) and the effect (landslides), and because of that, they are called “black box” models. The rainfall represents one of the most important and the easiest to quantify factors influencing the triggering of landslides. Indeed, most of the black box models are based on an empirical or statistical study of the rainfall events that in the past triggered landslides in a specific area (Caine 1980; Wieczorek 1996; Aleotti 2004; Guzzetti et al. 2008; Brunetti et al. 2010).

The most diffused thresholds are based on the intensity and duration of critical precipitation (Caine 1980; Aleotti 2004; Guzzetti et al. 2008), but also cumulative rain is widely used (Innes 1983; Terlien 1998; Hong et al. 2005; Cardinali et al. 2006). The choice of the right parameters for defining thresholds depends primarily on the landslide typology. There is a general agreement in recognising that the shallow landslides are preferentially triggered by short and intense rainfalls (Campbell 1974; Crosta 1998), while deep-seated landslides are more commonly connected with prolonged and less severe rainfall events (Bonnard and Noverraz, 2001).

A threshold defines the minimum or maximum level of a triggering or controlling variable (in the context of shallow landslides, usually rainfall intensity or duration) needed for a slope failure to occur. A minimum threshold will define the lowest level needed for the landslide to occur and below which

no landslide will take place. A maximum threshold is the limit above which the landslide will always occur (Crozier, 1997; Reichenbach et al., 1998).

The implementation of this approach in a forecast system is based on the comparison of the expected amount of rainfall in a given area with the thresholds, in case a given threshold is exceeded, the warning system is activated. Usually, rainfall real-time or forecasted data are plotted on a chart with thresholds and continuously compared. 2

Based on their spatial or timing validity, thresholds can be qualified as:

- scale geographical thresholds (global, regional and local): global thresholds are usually extended to a global or continental area; regional thresholds are defined as large areas (thousands of square kilometres) grouped by similar climatic and meteorological characteristics (e.g. Jibson, 1989, Larsen and Simon, 1993; Paronuzzi et al. 1998; Calcaterra et al. 2000; Aleotti, 2004); local thresholds are based on focused analysis of small areas, typically basins or slopes, with meteorological and geomorphological homogeneity (e.g. Bolley and Oliaro, 1999; Annunziati et al. 2000; Montgomery et al. 2000; Floris et al. 2004; Giannecchini, 2005; Zezere et al., 2005);
- time range thresholds: the validity is only for certain time intervals; these limits generally correspond to minimum and maximum rain events duration that it is analysed to define the thresholds and vary from few hours (Cannon and Gartner, 2005) to months (Floris et al., 2004; Zezere et al., 2005);
- types of triggered landslides: thresholds usually refer to the triggering conditions for certain landslides: debris flows (Jibson, 1989), soil slips (Baum et al., 2005), lahars (Ardoleba and Martinez, 1996), collapses in rock (Paronuzzi and Gnech, 2007);
- rainfall parameters of the triggering events: some thresholds analyse only the meteorological phenomena that occur immediately before or contemporary to a landslide, this rainfall is called “critical event” (Aleotti, 2004); in this case, the key parameters are the duration and intensity of rainfall; antecedent precipitation can be used as another critical rainfall parameter, the periods of antecedent rain that is considered influential varies from a few days (Aleotti, 2004; Chleborad, 2003) to months (Cardinal et al., 2006) depending on type of landslides: deep landslides are more affected by long antecedent rains, while the shallow ones are more correlated with short and heavy rains.

5.2 Deterministic models (white box)

For a slope stability problem, deterministic model analysis is the process of calculating the factor of safety for a given nominal set of values of system parameters. The system parameters include the geometry information of the slope and the slip surface, soil properties and profile of soil layers. The deterministic slope stability models can improve the spatial and temporal resolutions of the statistical, empirical approach. In the deterministic approach, the processes involving the slope stability are described by mathematical relationships that consider geotechnical, hydrological and morphometric characteristics of the analysed slope. In this case, it is spoken about "white box" models: the cause (rainfall or other destabilising factors) and the effect (landslide triggering) are related to an assumed physical model. The physics-based method allows a spatially distributed approach capable of carrying out the stability analysis for each point of the studied area. Therefore, a deterministic model can perform slope stability analysis even over large areas, getting results with the spatial resolution of the physical input parameters. In the case of large areas, the main drawback of this approach is substantially the time needed for calculates. These models are indeed common for scientific research purposes where timing is not the primary target. For the application in warning systems, it is necessary to face problems not only related to the physics of shallow landslides but also of computer technology. A too complicated physical model, or the choice of very high spatial and temporal resolutions, can lead to long computation times. The scientific and technological challenge in the use of distributed deterministic model for civil protection is represented by the research of the best compromise between physics complexity, high-resolution analysis and processing speed.

As regards to the physical models for the slope failure, a most widely used approximation is the infinite slope of isotropic and homogeneous soil: it is assumed that the depth to bedrock is much smaller than the length of the slope.

Johnson and Rodine (1984) proposed one of the most well-known hypotheses for mobilisation of debris flows and shallow landslides, the Bingham model. This model assumes that triggering can only occur if the shear stress exceeds the Coulomb strength:

$$\tau > \sigma \tan(\varphi) + c' \qquad (1)$$

Where τ is the shear stress acting on a surface, σ is the effective normal stress, φ is the internal friction angle of material c' is the effective cohesion. The Bingham model assumes that the soil strength changes as a function of pore pressure and friction angle (Iverson, 1997). Takahashi (1978) proposed a model for slope failure based on Bagnold's concept (1954) of dispersive stress, principally represented by a coulomb failure model for a fully saturated and cohesion-less soil with slope parallel

seepage. As a main assumption, the soil is fully saturated, and the water flows across the slope and on the slope surface. This model particularly suitable for debris flows triggered by flash floods in relatively gently slopes due to the surface-water surcharge (Iverson, 1997).

As abovementioned, debris flows are commonly described as flows of a two-phase mixture (solid and fluid) material. It is assumed they are triggered by pore pressure growth beyond hydrostatic values. Some authors assume that once the cohesion bonds are broken, the pore pressure can rise enough to liquefy the soil (Denlinger et al., 1990). Others postulate that the mobilisation of debris flows may occur only when the contraction of loose soils increases pore pressure until they reach a critical state (Casagrande, 1979; Sassa, 1984). Furthermore, the infiltrating water adds weight playing a mechanical role, mainly where the cohesion contributes significantly to the Coulomb soil strength (Iverson, 1997).

The pore pressure increase in a slope can occur in two ways: by direct infiltration of water from the surface (mainly a vertical flow) and by groundwater flow from adjacent portions (horizontal flows from the closest saturated areas). The increase in pore pressure for the elevation of the regional water table up to shallow soil depth. Models used for the groundwater flow in distributed slope stability analysis commonly use a simplification: soils and rocks are considered as continuous porous media that obey Darcy's law. Even if flow distribution and speed in natural slopes are deeply influenced by rock fractures, root channels and animal burrows (Pierson, 1983), It is nearly impossible to know all the preferential paths of flows, even harder in case of large areas and near real-time.

Topography plays an important role in driving surface and groundwater flows and Montgomery & Dietrich (1994) proposed a model that explicitly considers the topographic influence on soil saturation and slope stability. They use the hydrologic model TOPOG (O'Loughlin, 1986) to predict the degree of soil saturation in response to rainfall for topographic elements defined by the intersection of contours and flow tube boundaries. Using the approach of TOPOG model is possible to include the topographic control on the pore pressure to estimate the slope stability with the infinite slope model while treating the subsurface flow in the steady-state. Nevertheless, Montgomery and Dietrich's approach do not consider the transient movement of soil water. The steady flow condition is unrealistic for the major part of natural slopes during and immediately after a rainfall event, this simplification can have therefore a negative influence on the results.

Other models use instead unsteady flows: Okimura's model (Okimura et al., 1985) uses a finite difference approach to describe the groundwater flow, Wu and Sidle model (Wu et al., 1995) couples the infinite slope stability approach with a groundwater kinematic wave model and a continuous change vegetation root strength model. This model works for varying soil depth and hydraulic conductivity but neglects the unsaturated zone. Casadei links a dynamic and spatially distributed

shallow subsurface runoff model to an infinite slope model to predict the spatial distribution of shallow landslides also considering evapotranspiration and unsaturated zone storage (Casadei et al., 2003). The major part of the abovementioned models, the pore pressure as deriving from the rising of a saturated layer above a fixed slip surface. Others have proposed models that instead consider the pore pressure as generated by the advance of a wetting front coming from the top. The most common approach is based on two main models: the Green-Ampt infiltration model (Green et al., 1911), which infers the movements of the wetting front and finds the critical depth of triggering within the soil (Pradel et al., 1993), and Richards equation-based models. Many authors use different solutions to the Richards equation (Richards, 1931) to represent the movement of water in unsaturated soils and to assess the effect of transient rainfall on the timing and location of landslides (Iverson, 2000; Simoni et al., 2008).

Distributed slope stability models apply algorithms and equations to every cell of the study area, usually represented by a regular square grid that can have a side from few to thousands of meters. Sometimes it is necessary doing analysis at different depths for each pixel which means the computation can be extremely time-consuming depending on the extension of the area, the thickness of soil, spatial and temporal resolution and complexity of the equations. Many software products have been developed to handle this large amount of computations to apply stability models on a large scale. All these products use general forms of physical model equations introducing some approximations. SHALSTAB, SHAllow Landslide STABility model, is a popular distributed slope stability analysis tool (Dietrich et al., 1998) intended to be used within an ESRI-ArcGIS software environment. It is based on a distributed steady-state description of the hydrological fluxes coupled with an infinite slope analysis. This model is spatially predictive because it is not suited to forecast the timing of landslide triggering. SINMAP, Stability Index MAPping, and SINMAP 2 are other add-on tools for the ESRI-ArcGIS software. These tools are based on the infinite slope stability model, and the groundwater pore pressures are obtained from a topographically based steady-state model of hydrology (Pack et al., 1998, 2001). SINMAP allows an uncertainty of the variables through the specification of lower and upper bounds that define uniform probability distributions. SEEP/W is a stand-alone finite element software that resolves the Richards equations to account for transient groundwater flow. This software analyses groundwater seepage and excess pore-water pressure dissipation within porous materials and can model both saturated and unsaturated flow (Krahn, 2004). SEEP/ W is efficient in resolving saturated-unsaturated and time-dependent problems and in combination with the software SLOPE/W it performs the slope stability analysis adopting the limit equilibrium method. This software is suitable for the single slope scale (Tofani et al., 2006) not for distributed analysis. TRIGRS, Transient Rainfall Infiltration and Grid-based Regional Slope stability model, computes the transient pore pressure

distribution due to rainfall infiltration using the method proposed by Iverson (Baum et al., 2002). The results are stored in a distributed map of the factor of safety. TRIGRS is widely used by many authors for regional landslide hazard assessment (Baum et al., 2005; Salciarini et al., 2006; Chien-Yuan et al., 2005) and analysis under the approximation of nearly saturated soil, presence of flow field and isotropic, and homogeneous hydrologic properties (Baum et al., 2002). GEOtop-FS uses the hydrological distributed model GEOtop (Rigon et al., 2006) to compute pore pressure distribution by an approximate solution of the Richards equation and an infinite slope stability analysis to calculate the distributed factor of safety. The approximate solution of the Richards equation used by the software works in saturated soil conditions. The factor of safety of GEOtop-FS is computed in a probabilistic approach assigning statistical distributions to soil parameters instead of a single deterministic value. All these software programs use different models, approximations and programming languages but they have one common characteristic: all are suitable only for research purposes. In all these cases, speed is not the primary objective. Even using modern computational hardware, the computational time can take a very long time (days for a relatively small area at high spatial and temporal resolution), and it is impossible to use these programs in real-time and for warning system purposes.

HIRESSS simulator (Rossi, 2013) is a software capable of working at a regional scale in near real-time. The physical core of the software is made up of two parts: hydrological and geotechnical. The hydrological model is based on an analytical solution of an approximated form of the Richards equation under the wet condition hypothesis, and it is introduced as a modelled form of hydraulic diffusivity to improve the hydrological response. The geotechnical stability model is based on an infinite slope model that takes the unsaturated soil condition into account. HIRESSS uses Monte Carlo simulations to manage the typical uncertainty in the values of the input geotechnical and hydrological parameters, which is a common weak point of deterministic models. This software can use the computational power offered by multicore and multiprocessor hardware to perform simulations in reasonable runtimes, thanks to the structure of its code capable of running parallel processing.

6 Materials and methods

As mentioned in the previous sections, the main issue in considering the root reinforcement (or root cohesion) in the slope stability analysis (particularly in large areas) and landslides forecasting is the practical impossibility to evaluate the spatial variations of the parameter, mostly for its aboveground nature, the inevitable damages dealt to possible samples during the field campaigns, the extreme complexity of the natural conditions not reproducible in laboratories. Indeed, the below and above-ground conditions that determine the soil reinforcement are extremely variable in time and space and the involved elements countless. Field measurements of root properties in a single hillslope can return results varying of an order of magnitude, even in case of plants of same species, sizing and age (Hales et al., 2009; Hales and Miniat, 2017; Schmidt et al., 2001; Genet et al., 2008). The extreme variability is due to different root biomass and diameter distributions reflecting different distributions of nutritive elements and water, to the presence and positioning of eventual physical barriers within the soil (Stone and Kalisz, 1991; Osman and Barakbah, 2011) and the different sun exposure of the plants. This natural variability, the difficulties in the measurements and the uncertainty in root reinforcement models make the inclusion of the root reinforcement into slope stability models a very big challenge.

The spatial distribution uncertainty of root reinforcement that limits regional landslide forecasting is a well-known problem affecting other physical parameters such as cohesion, friction angle, and soil depth. It is worthwhile mentioning here that in steep terrain with colluvial soils (very prone to landslide at our latitudes), commonly, friction angles occupy a relatively narrow range of values (few grades), while as aforementioned, root cohesion can vary by one order of magnitude.

Several approaches have been developed and experimented to overcoming these limits in considering the root reinforcement at the regional scale.

Some of the most recent studies in this field tried to exploit the potentialities of remote sensing techniques to evaluate the root reinforcement through analysis of the aboveground parts of plants. Indeed, the remote sensing of aboveground parts of plants (geometry, biomass density and health state) is advanced enough to result useful to the cause. Estimation of biomass by remote sensing techniques can be traced back to the 1970s (Rouse et al. 1974).

Hwang et al. 2015 utilised lidar (light detecting and ranging) technology to estimate canopy height information and produce a spatially distributed root cohesion model. They developed an approach to characterise spatial patterns of total belowground biomass based on empirically derived allometric relationship developed from soil pit measurements: the vertical distribution of roots and tensile strength (the essential parameters to evaluate the root cohesion) were sampled at soil pits and

related to canopy height. Based on their studies, canopy height information from lidar can be effectively used to derive spatial patterns of root cohesion and improve shallow landslides forecasting in forested areas.

Another class of remote sensing approaches to the problem is based on the vegetation indexes (VIs), since they reflect the spectral characteristics of the vegetation–soil system. In recent decades, VIs have been indeed widely used to estimate aboveground biomass in large areas (Todd, Hoffer, and Milchunas 1998; Gao et al. 2013; Jiang et al. 2015). Most common critics moved to this approach deal with the influence of the background soil on the estimated VIs values. These critics represent the research question of the work by Wang et al. 2018: their aim was to improve grass-land above ground biomass modifying 'traditional' VIs (Difference Vegetation Index (DVI), Modified Soil-Adjusted Vegetation Index (MSAVI), Normalized Differential Vegetation Index (NDVI), the Ratio Vegetation Index (RVI)) to minimize the influence of soil background. They estimated the vegetation cover of 156 sites (1m x 1m sample plots) modifying the four mentioned VIs (obtaining modified vegetation indexes MVIs) to maximise the differences between vegetated and non-vegetated areas. The MVIs were then regressed with the sample-scale aboveground biomass (AGB) using different functions. They have found that the MVI-AGB models estimate better the AGB than the VI-AGB models and they individuated in the logarithmic MNDVI-AGB model the best one for their study area.

A further application of the NDVI to estimate the spatial pattern of root cohesion is described by Chiang and Chang, 2011. In their study on the potential impact of climate change on typhoon-triggered landslides, they used root cohesion values derived from NDVI values for the distributed calculation of the safety factor. According to the method used by Huang et al., 2006, Chiang and Chang, 2011 estimated the spatial variation of root cohesion retrieving the NDVI values and applying a linear transformation to the full spectrum values (−1.0 to 1.0) by setting the minimum value at 0.0 kPa and the maximum at 50.0 kPa of root cohesion.

The remote sensing techniques are not the only tools used to estimate root cohesion regional patterns. Hales, 2018 develops a model of root reinforcement of slopes, using distributions of biomass measured at the biome level (Schenk and Jackson, 2002), root tensile strength values of different vegetation species from previous studies, and deriving the root densities from the global wood density database (Chave et al., 2009; Hwang et al., 2005). The values of root cohesion resulting from the application of the model were subjected to a sensitivity analysis, demonstrating that tensile strength and root density (the parameters determining the natural variability of root cohesion on slopes) affect greeter the modelled cohesions than the parameters associated with model uncertainty (the reduction parameter that accounts for the well-known overestimation of root reinforcement by the Wu method)

Cislaghi et al., 2017 included the root reinforcement variability in a probabilistic 3D stability model developing the following multi-step procedure: (i) generation of maps with tree locations (a set of random forest configurations for each cell is calculated by Monte Carlo simulations, considering real forest characteristics as density of trees, diameter at breast height, minimal distance between the trees); (ii) calibration of a root distribution model based on field-collected data and the generated tree location maps; (iii) application of a root reinforcement model (the Fibre Bundle Model) which combines the density of roots of different diameters within the soil and the mechanical characteristics of roots.

Arnone et al., 2016 chose an eco-hydrological approach instead: they derived the root reinforcement values from eco-hydrologically based estimates of root biomass using a topological root branching model. To estimate the amount of roots and the distribution of diameters with depth (in order to apply the Fibre Bundle Model), the authors based on the Leonardo's rule, according to which the cross-sectional area of a trunk or branch of a tree is equal to the sum of the cross-sectional areas of the branches at any higher level (Richter, 1970).

6.1 Approach to solving the root reinforcement evaluation at the basin scale

The main scopes of this study are to identify an efficient method to consider the effect of the root reinforcement on slope stability at the regional scale, to inserting the parameter in a shallow landslide forecasting model and testing the eventual improvements of its forecasting capabilities.

Considering the approaches already explored and described by the scientific community, the advantages and drawbacks of either procedure and the characteristics of the chosen slope stability simulator, we individuated an approach to evaluate the root reinforcement at the regional scale, consisting in the following steps:

I. identifying the plant species of the study area and determining their distribution from in situ observations and already existing vegetational maps;
II. searching for each plant species of the area the root cohesion values measured and reported in the literature;
III. assigning root cohesion mean value and variation range to each subarea according to the dominant plant species;
IV. reproducing the natural spatial variability of the parameter through Monte Carlo simulations.

Root tensile strength of plant species was widely studied through in situ and laboratory tests (Genet et al., 2005; Genet et al., 2008; Genet et al., 2011; Hales et al., 2009; Hales et al., 2013; Hales

and Miniat, 2017; Anderson et al., 1989; Schmidt et al., 2001; Riestenberg, 1994; Bischetti et al., 2005; Bischetti et al., 2009; Norris, 2005; Zhang et al., 2012; De Baets et al., 2008; Burylo et al., 2011; Tosi, 2007). The estimate of root cohesion values also needs the knowledge of root profiles (root densities at different depth), so that root cohesion values are not very common in the literature. For this study, root cohesion values are taken from Bischetti et al., 2009, Burylo et al., 2011, Norris, 2005 when the plant species of the study area corresponded to the ones considered in these studies, differently from Hales, 2018 considering biome-level root cohesion values.

The Monte Carlo simulations are made by the distributed slope stability model chosen for this study, HIRESSS, which treats every geotechnical and hydrological input static data through Monte Carlo simulations to manage the intrinsic uncertainty of these parameters.

6.2 HIRESSS (HIgh REsolution Slope Stability Simulator)

In this study, HIRESSS simulator was chosen to perform the slope stability analysis because of its features such as i) the capability of computing the factor of safety at each time step and not only at the end of the rainfall event; ii) the variable-depth computation of slope stability; iii) the taking into account of the contribution of soil suction in unsaturated conditions; iv) the probabilistic treatment of the uncertainties in the main hydrological and mechanical parameters and, thus, of the factor of safety; v) high processing speed even for extensive area analysis.

The simulator processing is based on a physical model composed of two parts: hydrological and geotechnical (Figure 4). The hydrological model receives the rainfall data as dynamical input and provides the pressure head as a perturbation to the geotechnical model, that provides results in factor of safety (FS) terms.

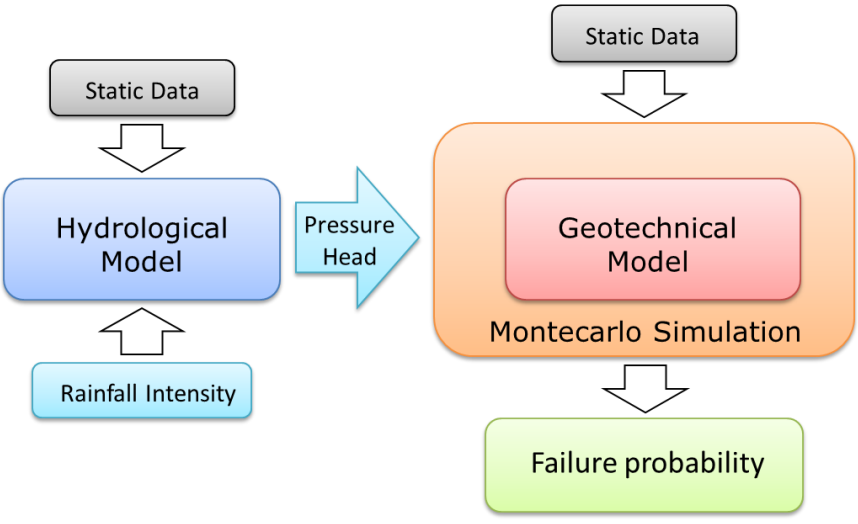

Figure 4. HIRESSS physical model structure.

The factor of safety is defined as:

$$FS = \frac{resisting\ forces}{driving\ forces} \qquad (2)$$

The safety factor is a dimensionless parameter that indicates the onset of an instability condition when it assumes the value 1 being the destabilising forces equal to the stabilising forces.

The structure of the software is inspired by the work of Iverson (Iverson, 2000) also used in the TRIGRS software. The hydrological model is based on an analytical solution of an approximated form of Richards equation under the wet condition hypothesis, and it is introduced as a modelled form of hydraulic diffusivity. The geotechnical model is based on an infinite slope model that considers the unsaturated conditions. During the stability analysis, the proposed model considers the increase in strength and cohesion due to matric suction in unsaturated soil due to negative pressure head. Moreover, the soil mass variation on partially saturated soil caused by the water infiltration is modelled. The model then provides for Monte Carlo simulations to manage the typical geotechnical parameters incertitude. The Monte Carlo simulation manages a probability distribution of the input parameter, and the ending results of the simulator are slope failure probabilities.

6.2.1 Physical model and Monte Carlo simulations

The hydrological model of HIRESSS is based on an analytical solution of an approximate form of the Richards equations, which describes the flow of water in an unsaturated porous medium due to the actions of gravity and capillarity neglecting the flow of the non-wetting phase, usually air.

Using the coordinate system (Figure 5) where z is normal to the slope (soil depth), x is tangent to the local surface slope, and y is tangential to the local topographic contour, the three-dimensional mixed water content form of the equation is:

$$\frac{\partial h}{\partial t}\frac{d\theta}{dh} = \frac{\partial}{\partial x}\left[K_L(h)\left(\frac{\partial h}{\partial x} - \sin\alpha\right)\right] + \frac{\partial}{\partial y}\left[(K_L)(h)\left(\frac{\partial h}{\partial y}\right)\right] + \frac{\partial}{\partial z}\left[(K_z)(h)\left(\frac{\partial h}{\partial z} - \cos\alpha\right)\right], \qquad (3)$$

where h is the groundwater pressure head, θ is the soil water volumetric content, t is time, α is the slope angle, K_L and K_Z are respectively the hydraulic conductivity in the lateral directions (x and y) and the hydraulic conductivity in slope-normal direction (z).

The general form of the Richards equation is a non-linear partial differential equation that does not have an analytical solution. Because the techniques that allow getting a solution for this general form without approximation hypothesis (the finite difference “FDM” and the finite elements “FEM”) require many computations, the developers of HIRESSS considered acceptable for the final scope to use an approximate analytical solution in favour of short computation time.

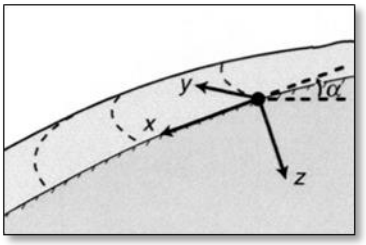

Figure 5. The coordinate system used in the physical model. Modified after Rossi, 2010.

The hydraulic part of the model is hence based on the following equations obtained through some approximations from equation 1 and valid under certain conditions:

$$\frac{\partial h}{\partial t} = (D_0 \, cos^2\alpha)\frac{\partial^2 h}{\partial z^2} \ , \qquad (4)$$

where D_0 is the maximum diffusivity, $D_0 = K_{sat}/C_0$ (whose solution is known in thermodynamics, Carslaw, 1955) and

$$D_0 = \frac{h_b K_{sat}}{\lambda(100 \cdot n - \theta_r)} \ , \qquad (5)$$

where θ_s is rewritten in function of the saturation degree and the porosity (θ=Sn).

The geotechnical model is based on the limit equilibrium method for an infinite slope. Having the shallow landslides a low depth compared to length and width, the assumption of a simplified geometry of the slide characterised by a planar slip surface on an infinitely extended planar slope (laterally and distally) is acceptable. The infinite slope approach assumes that the failure is the result of translational sliding, the failure plane and the water table are parallel to the ground surface and that the failure occurs along a single layer of infinite length.

The hydrological model computes the pressure head in relation to the depth, therefore, it is possible to evaluate the stability at different y values.

For points in unsaturated conditions, the model uses the following modelisation. The equilibrium equations for each axis, x and y, of the reference system in Figure 5 can be written as:

$$\begin{cases} m(y)gcos(\alpha) - F_N = 0 \\ m(y)gsin(\alpha) - F_A - F_C = 0 \end{cases} , \qquad (6)$$

where $m(y)$ is the mass of the columns of y depth soils, F_N the normal force, F_A the friction force and F_C the effective cohesion forces. Solving this equilibrium system, considering Fredlund et al., 1993 and doing the simplification of considering a two-state model of soil density (wet or dry), it is possible to write the condition of stability as:

$$1 \leq \frac{\tan\varphi}{\tan\alpha} + \frac{c\prime}{\gamma_{NS} y \sin\alpha} + \frac{(u_a - u_w)\tan\varphi^b}{\gamma_{NS} y \ sin \ \alpha} \ . \qquad (7)$$

From equation (5), neglecting the air pressure, considering Vanapalli et al., 1996 and Van Genuchten, 1980, we obtain the relationship used by HIRESSS for the factor of safety of unsaturated soil:

$$FS = \frac{\tan\varphi}{\tan\alpha} + \frac{c\prime}{\gamma_{NS} y \sin\alpha} + \frac{\gamma_w h \tan(\varphi)\left(\frac{1}{\left[1+\left(h_b^{-1}|h|\right)^{(\lambda-1)}\right]^{\left(\frac{\lambda}{\lambda+1}\right)}}\right)}{\gamma_{NS}\, y\, sin\ \alpha} \quad . \tag{8}$$

In saturated conditions (therefore with positive pressure head), the static equilibrium equations (4) become:

$$\begin{cases} m(y)gcos(\alpha) - F_N - F_{hyd} = 0 \\ m(y)gsin(\alpha) - F_A - F_C = 0 \end{cases} , \tag{9}$$

where the F_{hyd} is the hydrostatic force.

Starting from this equilibrium system and operating as above, we obtained the relationship used by HIRESSS for the factor of safety of a saturated depth point:

$$FS = \frac{\tan\varphi}{\tan\alpha} + \frac{c\prime}{[\gamma_{NS}(y-h)+\gamma_s h]\sin\alpha} - \frac{\gamma_w h \tan(\varphi)}{[\gamma_{NS}(y-h)+\gamma_{\ s} h]\, sin\ \alpha} \quad . \tag{10}$$

The main drawback of deterministic models is the uncertainty of the input data: the reliability of the results is strongly connected to the quality of the input parameter data needed by the physical model. Soil properties are extremely variable in space, an extended in situ measurements campaign can help in the reduction of the incertitude, but it is not resolutive, even more in case of huge areas. Developers of HIRESSS decided to face the problem using the Monte Carlo simulations technique. Monte Carlo methods are a class of computational algorithms that use repeated random sampling to compute their results. Monte Carlo methods are useful for modelling phenomena with significant uncertainty in the input data and allows to determine how random variation, lack of knowledge, or error affect the sensitivity, performance, or reliability of the system being modelled. It is a successful and reliable method in risk analysis when compared to alternative methods or human intuition. The input parameters are randomly generated from probability distributions that most closely match data we already have, or best represents our current state of knowledge in order to simulate the process of sampling from an actual population. This technique has a procedural scheme consisting in: i) definition of a domain for the data inputs and a probability distribution curve or an equiprobable uniform range of values; ii) randomly generation of data inputs from the domain using the specified

probability distribution chosen; iii) deterministic computation using the random inputs; iv) repetition of the first three points n times; v) aggregation of the results.

6.2.2 Model changes to consider the root reinforcement

HIRESSS model was modified to consider the effect of the root reinforcement to the stability of slopes. As reported in the Section 4.3.1, the root reinforcement can be considered as a component of the total cohesion of soil (e.g. Waldron and Dakessian, 1981; Gray and Ohashi, 1983; Operstein and Frydaman, 2000; Giadrossich et al., 2010). Considering this, the original FS (factor of safety) equations (Rossi et al., 2013) were modified considering the root reinforcement (c_r) as follows:

$$c_{tot} = c' + c_r \qquad (11)$$

where c_{tot} is the total cohesion of the soil; c' is the "standard cohesion", the component of cohesion commonly measured with laboratory test as the direct shear test. The root reinforcement (or root cohesion) can be considered equal to:

$$c_r = kT_r(A_r)\,, \qquad (12)$$

where T_r is the root failure strength (tensile, frictional, or compressive) of roots per unit area of soil, A_r/A is the root area ratio (proportion of area occupied by roots per unit area of soil), k is a coefficient dependent on the effective soil friction angle and the orientation of roots. The measure of c_r varies with vegetal species; within a single species, the measure depends on how plants respond to environmental characteristics and fluctuations. Therefore, the new equation for FS at unsaturated conditions is as follows:

$$FS = \frac{\tan\varphi}{\tan\alpha} + \frac{c_{tot}}{\gamma_{NS} y \sin\alpha} + \frac{\gamma_w h \tan(\varphi)\left(\frac{1}{\left[1+\left(h_b^{-1}|h|\right)^{(\lambda-1)}\right]^{\left(\frac{\lambda}{\lambda+1}\right)}}\right)}{\gamma_{NS}\, y\, sin\ \alpha}\,. \qquad (13)$$

In the saturated conditions, the equation for FS becomes:

$$FS = \frac{\tan\varphi}{\tan\alpha} + \frac{c_{tot}}{[\gamma_{NS}(y-h)+\gamma_s h]\sin\alpha} - \frac{\gamma_w h \tan(\varphi)}{[\gamma_{NS}(y-h)+\gamma_{\ s} h]\, sin\ \alpha}\,. \qquad (14)$$

7 Test Areas

7.1 Valle d'Aosta

The first study area is in the eastern part of the Valle D'Aosta, a region of northern Italy, it has an extension of about 837 km^2, and it is called "alert zone B" by the regional civil protection authorities (Figure 6). The area is delimited at the north-east corner by the Italian slopes of Monte Rosa (4634 m a.s.l), and it is characterised by three main valleys: Champorcher Valley, Gressoney Valley, and Ayas Valley. The Champorcher Valley lies on the right side of the Dora Baltea catchment and represents the southern part of the study area. The Gressoney and Ayas valleys occupy the central and the northern parts of the area showing a north-south orientation.

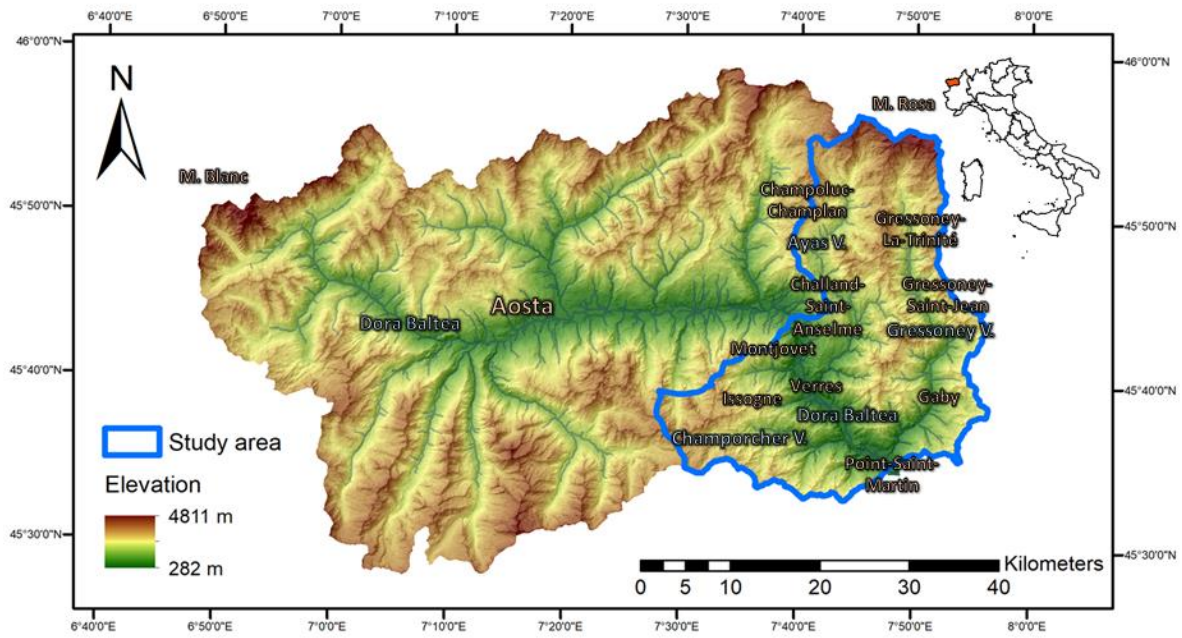

Figure 6. The Valle d'Aosta region in northwest Italy. Evidenced in blue, the study area "alert zone B".

7.1.1 Geological setting and landslides

The Valle d'Aosta region (3200 km^2) is part of the alpine chain, passing through the principal Europe-vergent Austroalpine-Penninic structural domain of the Western Alps. The region presents a complete section of the orogenic prism including (i) the Austroalpine domain; (ii) the ophiolitic

Piedmont zone; and (iii) the Pennidic domain. These tectonic-metamorphic units composed of a complex pile of nappes, which present a post-collisional tectonic activity and a neo-tectonic dislocation system activation (Bistacchi et al. 2001).

Figure 7 shows the lithological map of the study area obtained by reclassifying the geological units according to 11 lithological groups: landslides, calcareous schist, alluvial deposits, glacial deposits, colluvial deposits, glacier, granites, mica schists, greenstone, black schists, and serpentinites. The main outcropping lithologies of the study area are metamorphic and intrusive rocks: granites, metagranites, schists, and serpentinite.

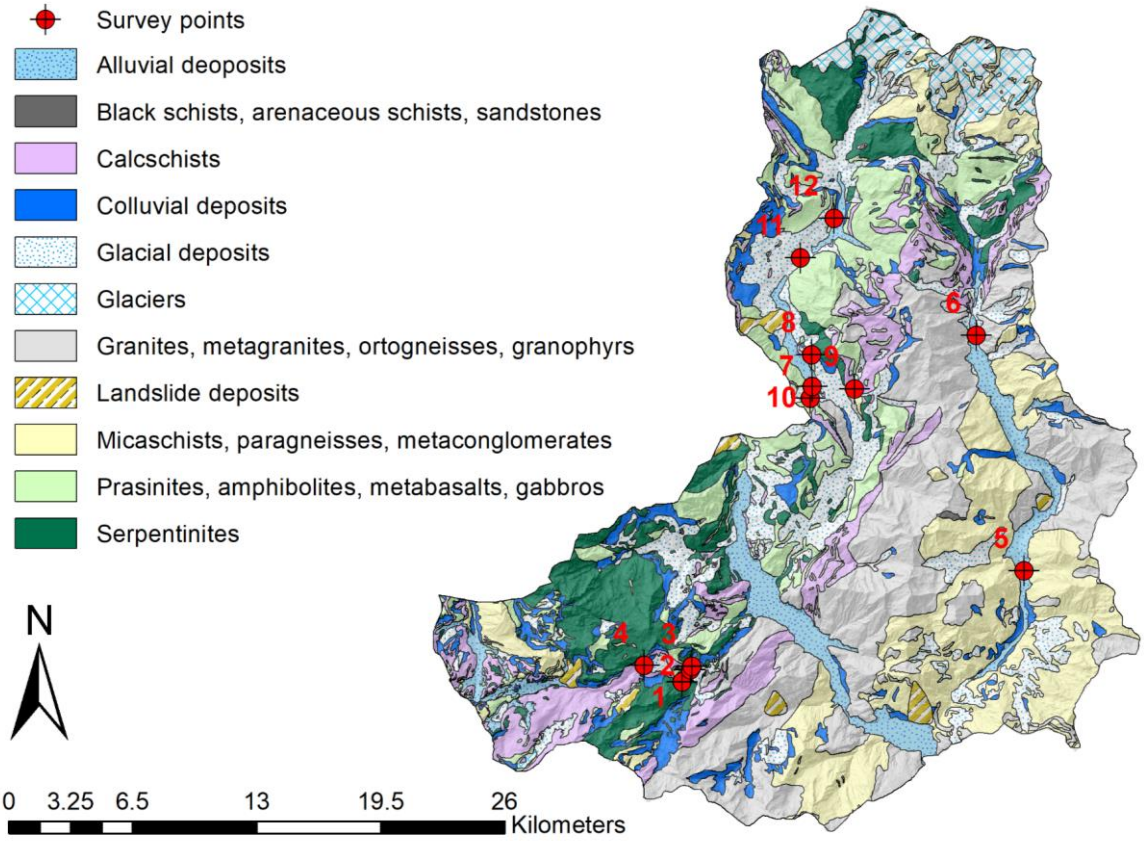

Figure 7. Spatial distribution of survey points compared to the lithology.

The geomorphology of the study area is characterised by steep slopes and valleys shaped by glaciers. The glacial modelling is shown in the U-shape of the Lys and Ayas valleys, and the erosive depositional forms found in the Ayas Valley. The three valleys' watercourses, the Lys Creek, the Evançon Creek, and the Dora Baltea River, contributed to the glacial deposits modelling with the formation of alluvial fans.

Due to its geological and climatic features, the area is very prone to landsliding: rockfalls, deep-seated gravitational slope deformations, rocks avalanches, debris avalanches, debris flows, and debris

slides are the main mass movements to which the area is subjected (Catasto dei Dissesti Regionale – from Val d'Aosta Regional Authorities). 18% of the Valle d'Aosta territory is affected by landslides (Triglia, 2010).

7.1.2 Vegetation and climate

The massifs dominating the Valle d'Aosta landscape act as morphological boundaries and deeply influence the local climatic conditions. The high peaks limit the access of air masses from the Mediterranean Sea or the Atlantic Ocean, causing a clear difference in the rain and snow precipitation regimes (Mercalli, 2016). Indeed, the climate is characterized by wide range of temperatures and rainfall/snowfall (min, max and average values of 1000–1100 mm/year) in mountainous and marginal sector, while, in correspondence of the principal valley bottom, the weather conditions are associable to a temperate climate with relatively lower rainfall (lower than 600 mm/year).

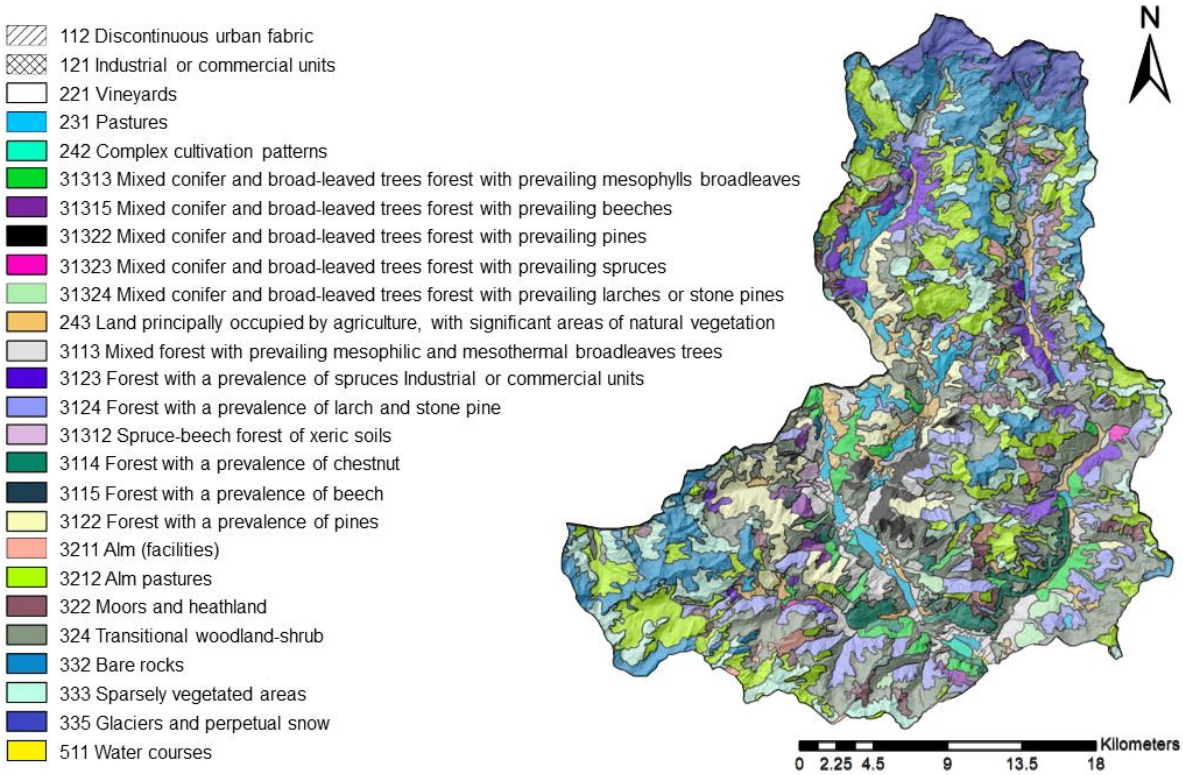

Figure 8. Study area land cover and vegetation, classes numbering according to CORINE Land Cover classification (Corine Land Cover 2012, 4th and 5th levels by ISPRA, http://groupware.sinanet.isprambiente.it/uso-copertura-e-consumo-di-suolo/library/copertura-del suolo/corine-land-cover).

As typical in alpine valleys, the study area has a prevalence of highly vegetated areas, while human settlement distribution is located at the valley bottom. The land cover is prevalently represented by forest, natural grassland, and rocky outcrops with little or no vegetation (Figure 8). Most common forest categories are mixed-coniferous forests (30% of the total forested area), larch forests, mixed broad-leaved forests, and broad-leaved mixed coniferous forests. The coniferous trees are the most common, representing more than 90% of the Aosta Valley forests: larch (Larix decidua Mill.), Norway spruce (Picea abies (L.) Karst,), Scots pine (Pinus sylvestris L.), cembra pine (Pinus cembra L.) and silver fir (Abies alba Mill.) are the dominant species (Camerano et al., 2007).

7.1.3 Data collection

The input parameters needed by HIRESSS to perform the stability simulations can be divided into two classes: the static data and the dynamical data. The static data are represented by geotechnical and morphological parameters of the areas, while the dynamical data are represented by rainfall intensity. The spatial and temporal resolutions for the data depend not only on the available information but also on the operator choices dictated by the requirements. In this application, the spatial resolution was 10 meters (this means that HIRESSS computed the stability analysis in pixels of 10 m per 10 m), while the time step of the rainfall intensity data was one hour.

The HIRESSS model loads the static and dynamical data as raster maps in which the parameters have been adequately spatialized (Figure 9). The parameters are: slope gradient, effective cohesion (c'), root cohesion (c_r), friction angle (ϕ'), dry unit weight (γ_d), soil thickness (dbt), hydraulic conductivity (k_s), initial soil saturation (S), pore size index (λ), bubbling pressure (h_b), effective porosity (n), residual water content (q_r), eventual outcrop rock mask and rainfall intensity.

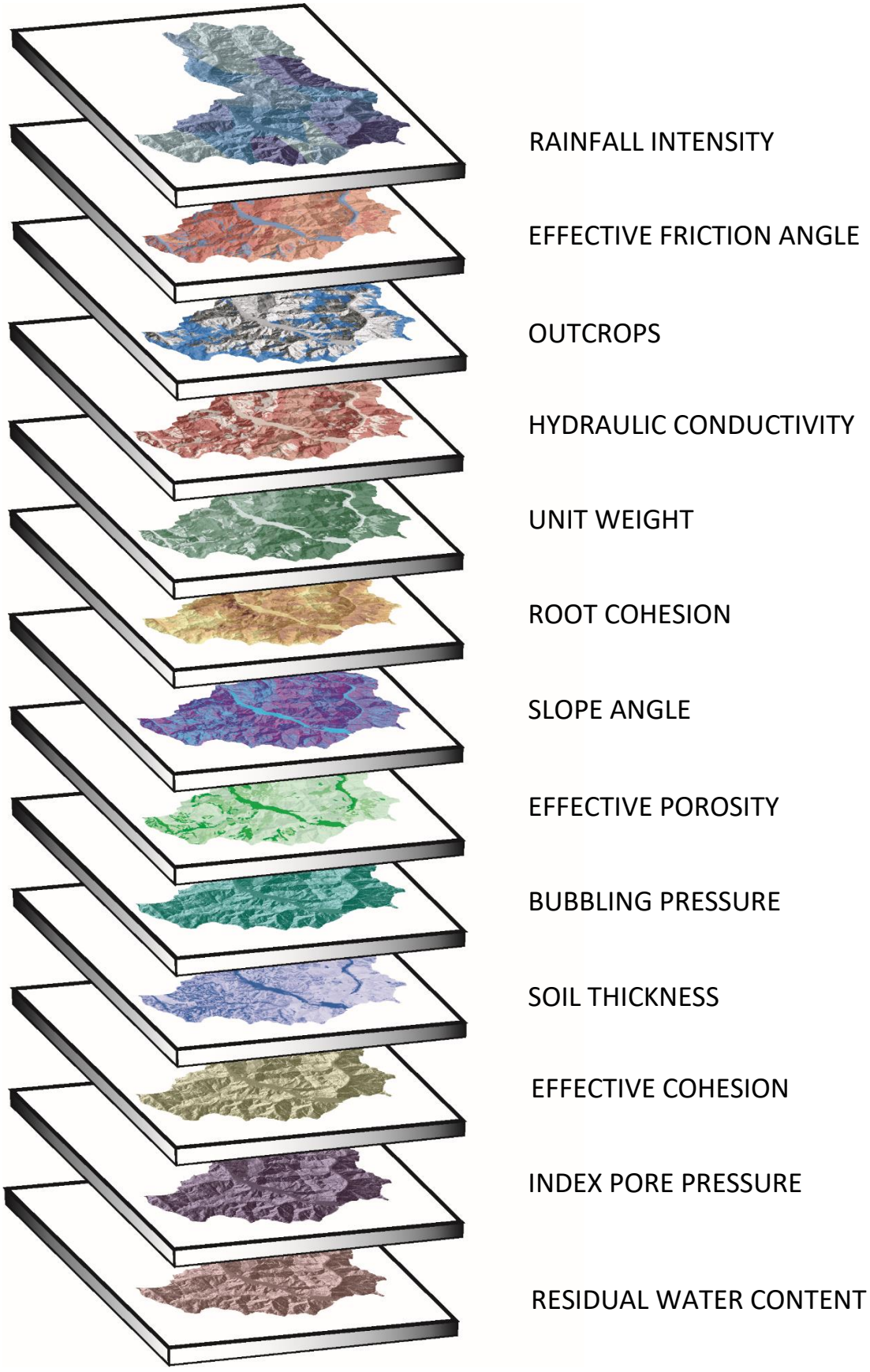

Figure 9. HIRESSS Input data as raster maps.

7.1.4 Static data

The slope gradient was obtained from a DEM (digital elevation model) with a resolution of 10 meters and dated 2006. Effective cohesion, friction angle, hydraulic conductivity, effective porosity, and dry unit weight were derived from in situ measurements and laboratory tests on samples.

The *in-situ* campaign was performed in 12 selected survey points (Bicocchi et al., 2016; Tofani et al., 2017) during August and September 2016 (Figure 7). The survey points were selected considering (i) physiography, (ii) landslides occurrence, and (iii) lithology of the area. The following analyses were conducted:

- registration of the geographical position was undertaken using a GPS and photographic documentation of the site characteristics (morphology and vegetation);
- the *in-situ* measurement of the saturated hydraulic conductivity (k_s) was carried out utilising the constant head well permeameter method using an Amoozemeter (Amoozegar, 1989);
- the sampling of an aliquot (∼2 kg each) of the material was conducted for laboratory tests, including grain size distributions, index properties, Atterberg limits, and direct shear tests.

The *in-situ* permeability measurements and the soil samplings were made at depths ranging from 0.4 to 0.6 m below the ground level.

In addition, the samples collected in situ were examined in the laboratory to define a wide range of parameters to more extensively characterise the deposits. The following tests were performed:

- grain size distribution (determination of granulometric curve by sieving and settling following ASTM recommendations), and classification of soils (according to AGI and USCS classification, Wagner, 1957);
- determination of the main index properties (porosity, relationships of phases, natural water content (w_n), the respective natural and dry unit weight (γ) and (γ_d) following the ASTM recommendations;
- determination of Atterberg limits (liquid limit (LL), plastic limit (PL), and plasticity index (PI));
- direct shear test on selected samples.

Soil thickness was assessed by applying the GIST model (Catani et al., 2010; Del Soldato et al., 2016). Soil characteristic curves parameters (pore size index, bubbling pressure, and residual water content) were derived instead from literature values (Rawls et al., 1982).

Root cohesion variations in the area (at the soil depth chosen for the physical modelling with HIRESSS) were first obtained, identifying the plant species and determining their distribution from in

situ observations and vegetational maps. For the first simulations described in Salvatici et al., 2018, as vegetational map was considered the Carta delle serie di vegetazione d'Italia, Italian Ministry of the Environment and Protection of Land and Sea. Successively, considering the purposes of the present study, a different vegetational map was chosen: the land use map Corine Land Cover 2012, 4th and 5th levels by ISPRA, since the latter represent in more detail the plant species distribution of the previous one. A more detail vegetational map allows for producing a more detail distribution map of the root cohesion (Figure 10).

The measure of cohesion due to the presence of roots was assigned to each subarea according to the dominant plant species and literature root cohesion value for that species (Bischetti et al., 2009, Burylo et al., 2011, Norris, 2005 when the plant species of the study area corresponded to the ones considered in these studies, differently Hales, 2018 considering biome-level root cohesion values).

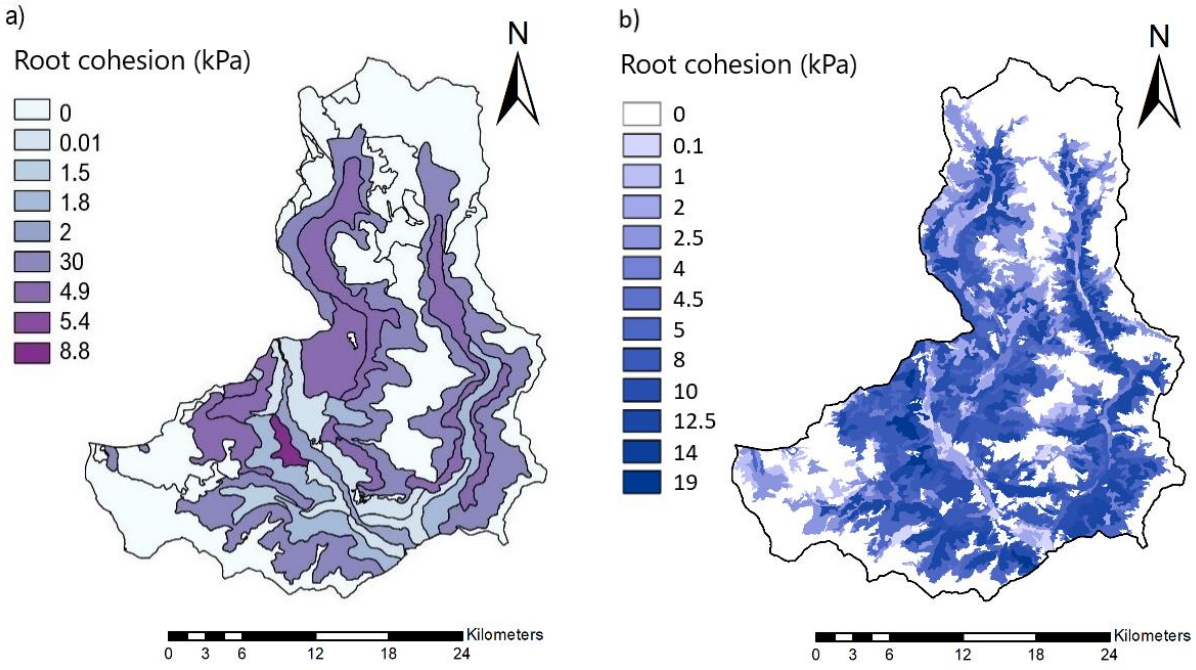

Figure 10. The root cohesion map distribution of the Valle d'Aosta study area: a) former root cohesion map (Salvatici et al. 2018); b) updated root cohesion map.

The last static input data is represented by the outcrop rock areas. These areas were defined considering land use maps, slope angles and direct observations so that the HIRESSS model avoided simulations on steep slopes of bare rocks.

The geotechnical properties have been spatialized according to lithology.

7.1.5 Dynamic data

The dynamic data are represented by the rainfall data, which are used by the model to construct the soil saturation and consequently the matrix suction and the pressure head for every pixel and time step. The initial soil saturation distribution could be provided to the model if available. Otherwise, it is possible inserting an initial soil saturation of zero for every pixel of the area, the model starts from zero and through the hydrological equations on which is based computes the soil saturation for every time step. In this case, it is preferable to have a sufficient backward extension of the rainfall data with respect to an eventual particular period of interest of the simulation.

In the study area of the Valle d'Aosta, the hourly rainfall data from 27 rain gauges were available. The rainfall data were elaborated applying the Thiessen polygon methodology (Rhynsburger, 1973), modified to consider the elevation, to spatialize the data set and generate 10 X 10m cell size input raster This approach defines an area around the points (rain gauges), where every location is nearer to this point than to all the others. Thiessen polygon methodology does not consider the morphology of the area; therefore, alert zone B was divided into three catchment areas, and the polygons were calculated for each of the rain gauges considering the reference catchment basin (Figure 11).

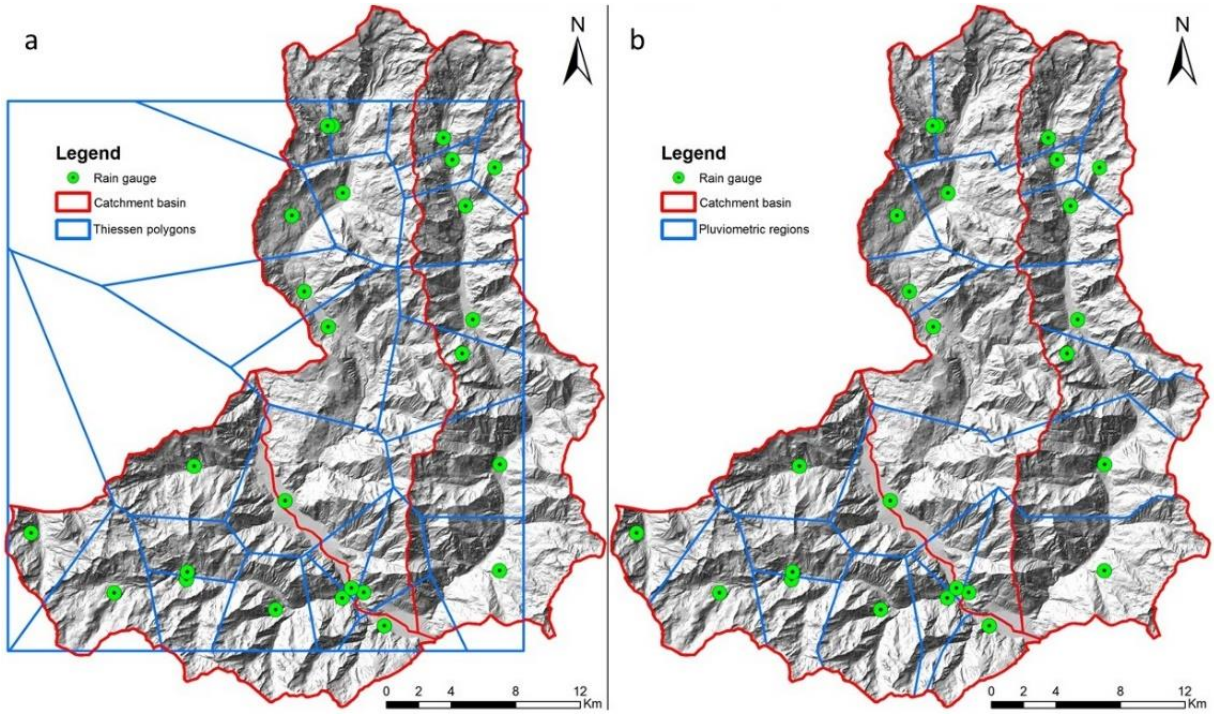

Figure 11. Comparison of Thiessen polygons methodology; (a) simple and (b) modified according to the catchment basins boundaries.

7.1.6 Simulations input data

The geotechnical and hydrological data obtained from survey campaign and laboratory analyses and considered for the simulations are shown in Table 1. The analysed soils are predominantly sand with silty gravel. The saturated unit weights range from 18.2 to 21.5 kNm^3, while the dry unit weight values lie between 13.7 to 18.7 kNm^3. The Atterberg limits (LL and PL) were measured on samples with enough passing fraction (i.e. > 30% by weight) through a 40 ASTM (0.425 mm) sieve. For prevalently sandy samples, LL values are mostly around 40% of water content (% by weight), while the PL is around 30%. The effective friction angle varies between a minimum of 25.6 and a maximum of 34.3, while the effective cohesion ranges from a minimum of 0.0 to a maximum of 9.3 kPa. The saturated permeability values are around a medium-high value of 10^{-6} m s^{-1}.

In this study area, the root cohesion was assumed in Salvatici et al. 2018 as ranging from a minimum of 0.0 kPa to a maximum of 8.9 kPa (these values represent the mean root cohesion assigned to each sector, it is worth remembering here that the Monte Carlo iterations move then in a range of +/-50% around the mean value in the case of this parameter). Successively to the update of the root cohesion map (see 7.1.4), in the simulations specifically performed for the present study, root cohesion values range from 0 (mainly in the outcrop area) to 19 kPa (in regions occupied by mountain maple on the left bank of Dora Baltea River).

In Table 2, the parameter values used for the simulations are shown. The pore size index, bubbling pressure, and residual water content are constant for the whole area, measuring 0.322 (l), 0.1466 m, and 0.041 (q_r), respectively. The initial soil saturation was inserted equivalent to zero for all the study area (from bedrock to surface).

Two different periods of rainfall were considered to perform the stability simulations: i) 02/04/2009-30/04/2009 (Figure 12); ii) 21/05/2010-20/06/2010 (Figure 13). Distribution and quantities of the cumulated rainfall are shown in Figure 14.

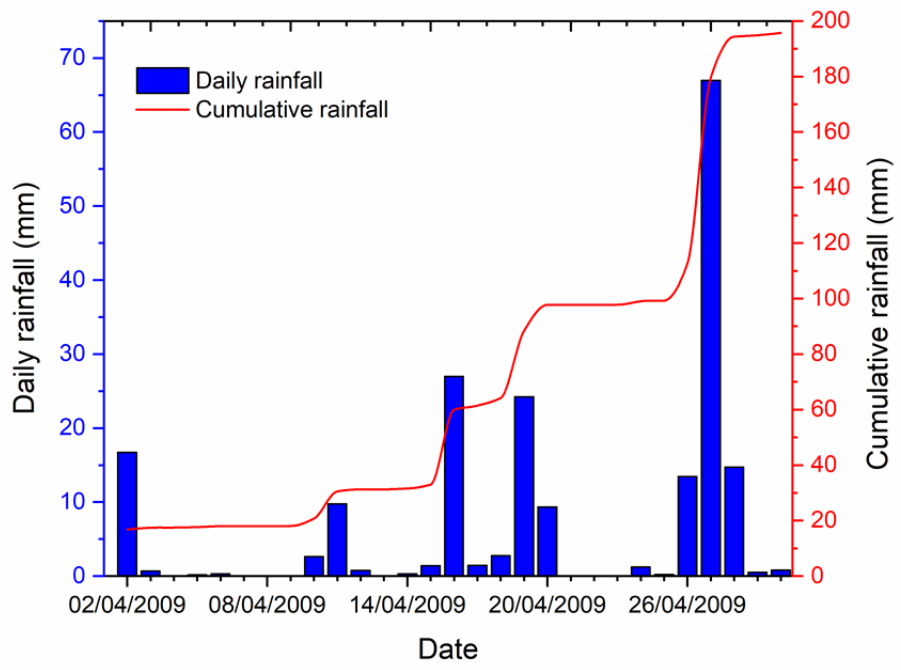

Figure 12. Intensity rainfall per day and cumulative rainfall for the event from the 2nd and the 30th April 1999.

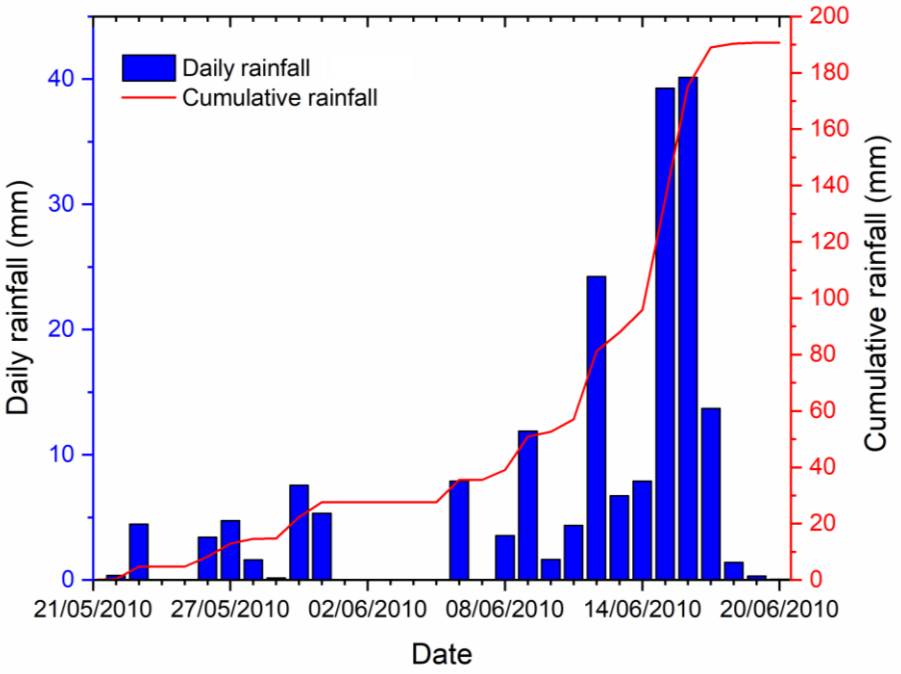

Figure 13. Intensity rainfall per day and cumulative rainfall for the event from the 21st and the 20th June 2010.

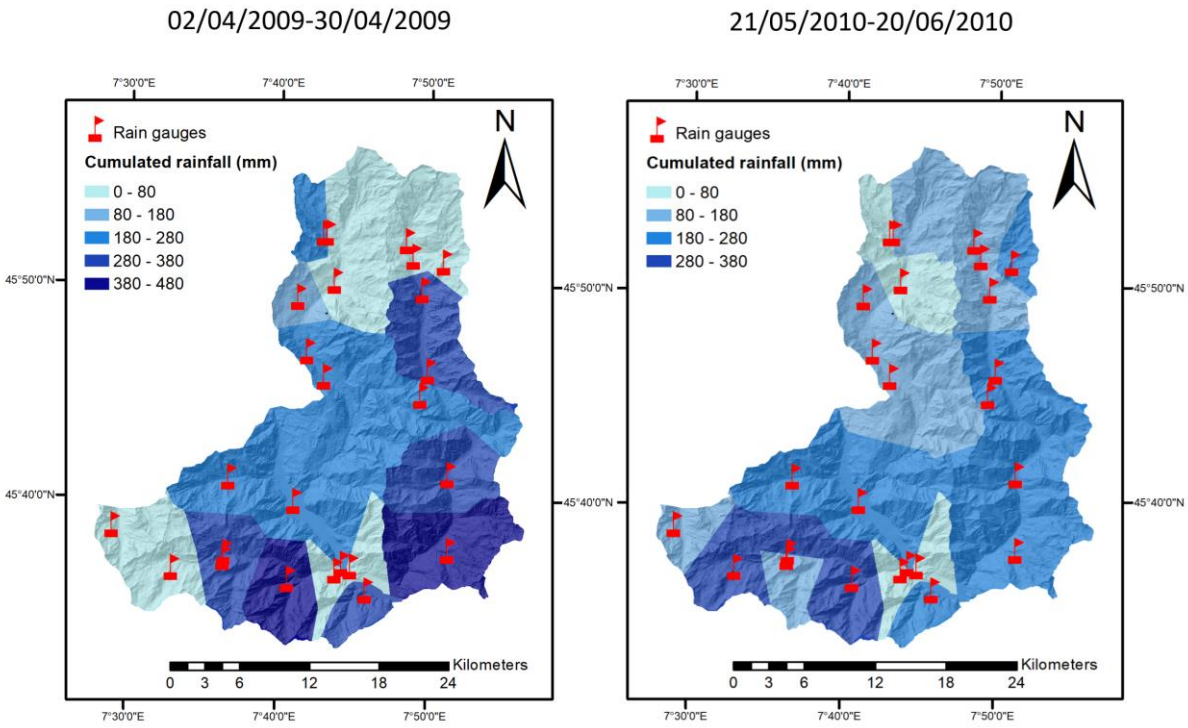

Figure 14. Cumulated rainfall of each polygon of the two events considered for the simulations.

SITE	*SOIL TYPE*	*G %*	*S %*	*M %*	*C %*	*LL (%)*	*PL (%)*	*PI (%)*	*USCS*	*γ (kN m^{-3})*	*γ_d (kN m^{-3})*	*γ_{sat} (kN m^{-3})*	*n (%)*	*w (%)*	*k_s (m s^{-1})*	*k_{sc} (m s^{-1})*	*ϕ' lab (°)*	*c' (kPa)*
Site 1	Sand with silty gravel	27.8	45.2	23.4	3.6	36	25	11	SM	16.7	13.7	18.3	47.3	11.3	/	2.52E-06	25.6	1.0
Site 2	Sand with gravelly silt	19.4	50.5	29.0	1.1	38	25	14	SC	19.1	14.5	18.8	44.3	11.4	2.71E-06	1.48E-06	34.3	1.5
Site 3	Sand with gravel and silt	26.9	45.2	26.8	1.1	/	/	/	/	/	/	/	/	/	/	8.89E-07	/	/
Site 4	Sand with gravelly silt	18.8	40.4	39.2	1.6	38	27	11	SM	19.5	14.8	19.0	43.2	10.7	1.36E-07	4.51E-07	34.3	0.0
Site 5	Sand with gravel and silt	31.0	43.1	25.7	0.2	47	36	11	SM	18.4	14.0	18.5	46.3	11.0	/	2.44E-06	25.7	9.3
Site 6	Sand with poorly silty gravel	28.5	57.5	13.9	0.1	52	38	13	SM	18.7	13.5	18.2	47.9	20.0	/	8.27E-06	30.2	4.4
Site 7	Sand with silty gravel	37.0	42.6	17.9	2.5	40	32	8	SM	20.3	15.5	19.5	40.4	26.2	5.18E-06	2.97E-06	28.2	3.4
Site 8	Sandy silty gravel	58.1	24.6	16.0	1.3	43	28	16	GM	17.2	15.7	19.6	39.6	9.4	/	3.76E-06	30.1	8.1
Site 9	Gravelly silty sand	18.7	55.1	24.4	1.8	46	36	10	SM	20.1	18.7	21.5	27.9	8.1	2.41E-06	1.73E-06	33.9	0.6
Site 10	Sand with gravelly silt	21.9	52.0	25.1	1	46	37	8	SM	18.4	16.0	19.8	38.6	15.5	/	2.10E-06	30.3	1.5
Site 11	Gravelly silty sand	24.3	51.4	21.2	3.1	31	25	7	SM	21.7	18.0	21.2	31.9	20.5	4.03E-06	3.05E-06	29.8	2.0
Site 12	Gravel with poorly silty sand	55.2	32.2	12.2	0.4	55	45	10	SM	15.3	14.6	18.9	43.9	5.1	1.54E-05	8.25E-06	30.2	1.6
	MEAN	**30.63**	**44.98**	**22.9**	**1.48**	**42.91**	**32.18**	**10.82**		**18.67**	**15.36**	**19.39**	**41.03**	**13.56**	**4.98E-06**	**3.16E-06**	**30.24**	**3.04**
	MEDIAN	**27.35**	**45.2**	**23.9**	**1.2**	**43**	**32**	**11**		**18.7**	**14.8**	**19.0**	**43.2**	**11.3**	**3.37E-06**	**2.48E-06**	**30.2**	**1.6**
	STD.DEV	**13.31**	**9.48**	**7.41**	**1.11**	**7.15**	**6.71**	**2.71**	/	**1.80**	**1.68**	**1.10**	**6.34**	**6.30**	**5.38E-06**	**2.56E-06**	**3.05**	**3.07**
	MAX	**58.1**	**57.5**	**39.2**	**3.6**	**55**	**45**	**16**		**21.7**	**18.7**	**21.5**	**47.9**	**26.2**	**1.54E-05**	**8.27E-06**	**34.3**	**9.3**
	MIN	**18.7**	**24.6**	**12.2**	**0.1**	**31**	**25**	**7**		**15.3**	**13.5**	**18.2**	**27.9**	**5.1**	**1.36E-07**	**4.51E-07**	**25.6**	**0**

Table 1. Geotechnical properties of survey points (grain size distribution, Atterberg limits, index properties, permeability, and shear strength parameters).

Lithological classes	*Soil Type*	*ϕ' lab (°)*	*c' (Pa)*	*γ_d (kN m^{-3})*	*n (%)*	*k_s (m s^{-1})*	*h_s*	*q_r*	*l*
Calcareous schist	Sand with gravelly silt	31	1000	16.5	39	1.1E-05	0.1466	0.041	0.322
Alluvial deposits	Sand with gravel and silt	26	1000	14.0	46	3.0E-06	0.1466	0.041	0.322
Glacial deposits	Sand with silty gravel	31	1000	15.3	41	2.7E-06	0.1466	0.041	0.322
Colluvial deposits	Sand with silty gravel	25	1000	13.7	47	2.5E-06	0.1466	0.041	0.322
Granites	Sandy gravel	30	1000	17.6	32	4.0E-06	0.1466	0.041	0.322
Mica schists	Sandy silty gravel	30	1000	17.7	32	6.0E-06	0.1466	0.041	0.322
Pietre Verdi	Gravel with silty sand	32	1000	16.3	37	4.6E-06	0.1466	0.041	0.322

Table 2. Spatialized geotechnical parameters of each lithological class as input for the HIRESSS model.

7.2 Cervinara

The second case study concerns an area of 18.5 km^2 in the Campania region (Southern Italy). The study area (Figure 15) is located in the centre of the region (41°01'15.36" N, 14°37'15.21" E), in the municipality of Cervinara (Avellino province) among 30 km away from the regional capital Napoli and the Vesuvio volcano. It is due to this closeness to the volcano that the major part of the area of Cervinara has typical layered soils composed by a basal layer of weathered bedrock (carbonates) covered by air-fall volcanic (pyroclastic) soils (Cuomo and Foresta, 2015; Cascini et al., 2011).

Two main reasons shall justify the selection of this area for the study: i) the availability of an abundant in- situ and laboratory dataset from which to draw on for the simulations input data; ii) the occurrence of relatively-recent and well- documented rainfall-induced shallow landslides, being the latter an essential condition for the validation phases.

In the mid of December 1999, the area of Cervinara was hit by intense rainfall that triggered several shallow landslides then evolved into debris flows and debris avalanches in the night between the 15th and 16th, causing six victims beside to severe damages to buildings and facilities. The intense rainfall event started on the 14th December 12 a.m. The rain-gauge of the area (the S. Martino Valle Caudina rain gauge) recorded a cumulated rainfall of 264 mm in 38 hours (Fiorillo et al. 2001; Fiorillo

and Wilson 2004). Cascini et al. 2005 reported that the return time of the cumulated rainfall from the 14th December 6:00 p.m. to the 15th December 6:00 p.m. was 10-20 years, passing rapidly to an event with a return time of up to 50-100 years in the consecutive hours. During the night between the 15th and the 16th, in the time of three hours, multiple debris floods and debris flows were triggered in the municipality of Cervinara.

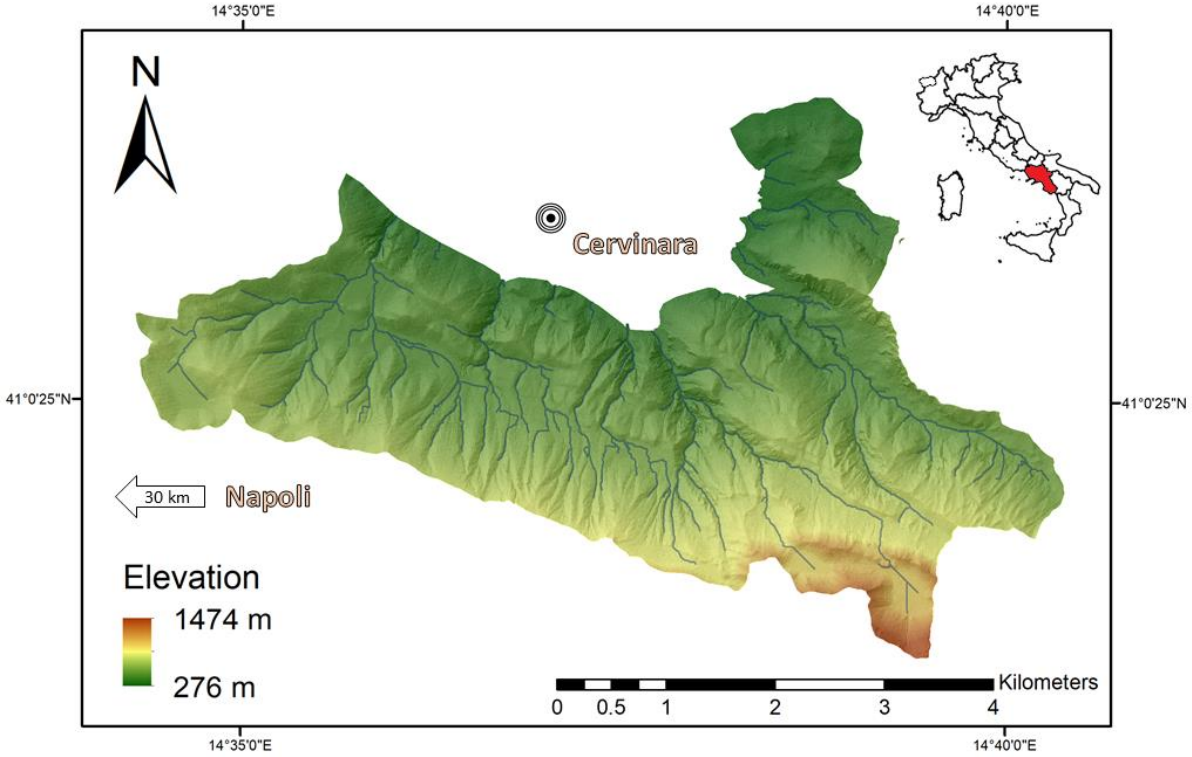

Figure 15. The study area in the Cervinara (AV) municipality.

7.2.1 Geological setting and landslides

The study area is characterised by pyroclastic soils over carbonate bedrocks, and frequently it is affected by flow-type rainfall-induced shallow landslides (Cascini et al., 2008a).

The pyroclastic soils (generally up to 2-3 m thick) derived from the explosive eruptions of Vesuvio volcano that has spread pumices and ashes over a surrounding area of 3000 km^2 (Cuomo and Foresta, 2015). From the granulometric point of view, the soils are mostly sands/gravels (the pumice soils) and silty sands/sandy silts (the ashy soils) (Bilotta et al., 2005). A typical stratigraphy of the area is ashy silty sands over ashy sandy silts, with eventual thin discontinuous layers of sands/gravels (pumices) embedded between the two, and carbonate bedrock below (Damiano et al. 2012). Not uncommon to find also only the ashy silty sands soil over the bedrock or directly outcropping bedrock (Cuomo and Foresta, 2015).

The area is dominated by two main geomorphological elements: bedrock concavities filled with pyroclastic materials reaching the maximum soil thickness in the central zone; planar hillslopes with an almost constant soil thickness (Cascini et al. 2008a).

7.2.2 Vegetation and climate

The vegetation of the Cervinara study area is dominated by beech woods and oak woods in the most elevated regions passing gradually to coppice and mixed woods of chestnut, yews, holm oaks, Italian alders and wych elm. In the areas close to the urban settlements are instead the small parcels of agricultural lands to dominate the landscape.

The weather condition to which the Cervinara territory is subjected are typical of the Temperate dry-warm summer climate: the main rainfall occurs in autumn and winter (maximum value 215 mm in December and 35 mm in July), the average monthly temperature reaches the highest values in July-August (24°C) and the lowest in January-February (8°C)(Fiorillo, 2011).

7.2.3 Data collection

As aforementioned, the area was recently and widely investigated with in situ tests (data from Autorità di Bacino Liri-Garigliano and Volturno, 2012) including iron-rod drillings and penetrometer tests performed up to the bedrock contact beside to hand-excavated shafts to investigate 1 to 3 meters below the ground surface. Further details of this field campaign are provided in Cuomo and Foresta (2015), for the geotechnical input data (dry unit weight, effective porosity, effective cohesion, effective friction angle, saturated hydraulic conductivity, residual water content, pore size index, bubbling pressure) we referred to this work beside to the one by Cuomo and Iervolino (2016).

For the other input data, already available information were considered (DEM, soil thickness, rainfall intensity) or derived from exiting data through digital elaborations and analysis (slope angle, outcropping maps), with the exception of the plant species distribution, for the determination of which, personally in situ surveys were integrated with Corinne Land Cover map 2012 information.

7.2.4 Static data

After considering the characteristics of the area, it was chosen to perform the simulations calculating the factor of safety at the contact level with the bedrock. Existing little differences in the fundamental geotechnical parameters from point to point within the 1-3 meters of the soil, for the spatial distribution of the geotechnical parameters was chosen to consider a homogeneous layer covering all the area with the characteristics of the ashy silty sands (see section 7.2.1) layer.

About the assumed soil thickness for this case study, the reported data by Cuomo and Iervolino (2016) regarding the pyroclastic deposits were considered. The slope angle was computed starting from a Digital Terrain Model (DTM) derived by LIDAR (Light Detection And Ranging) and provided by "Ministero dell'Ambiente e del Territorio". The DTM has a resolution of 1 m, and it is dated 2009.

The outcrops map was defined integrating aerial and satellite images of the interest period of rainfall event (google Earth images), soil thickness information (Cuomo and Iervolino, 2016) and the computed slope angles (the sectors with slope angle larger than 60° were considered outcropping rocks).

7.2.5 Dynamic data

The rainfall intensity data were recorded by the S. Martino Valle Caudina rain-gauge (288 m a.s.l., 2 km far from Cervinara, ID 18897, UTM 469109, 4540511) and reported by Cascini et al. 2005. Since in the study area a single rain gauge is present, the rainfall data did not need the spatialization procedure adopted for the Valle d'Aosta study area (see 7.1.5).

7.2.6 Simulations input data

Based on the data reported by Cuomo and Foresta (2015) and Cuomo and Iervolino (2016) for the homogeneous layer the following values of the geotechnical parameters were assumed: dry unit weight (γ_d) 7.8 kN/m^3, effective porosity (n) 0.7, effective cohesion (c') 0 kPa, effective friction angle (φ') 38°, saturated hydraulic conductivity (k_s) 5.00E-06 m/s, residual water content (q_r) 0.008, pore size index (λ) 0.676, bubbling pressure (h_b) 0.8657 mH_2O (Table 3).

γ_d (kN/m^3)	7.8
n	0.7
c' (kPa)	0
φ' (°)	38
k_s (m/s)	5.00E-06
q_r	0.008
λ	0.676
h_b (mH_2O)	0.8657

Table 3. Geotechnical parameters input data for the Cervinara study area, where γ_d is the dry unit weight, n the effective porosity, c' the effective cohesion, φ' the friction angle, k_s the hydraulic conductivity, q_r the residual water content, λ the pore size index, h_b the bubbling pressure.

The soil thickness data reported by Cuomo and Iervolino, 2015 for the pyroclastic deposit show values ranging mainly between 0 m to 5 m, in very few areas the soil is reported to reach 10 m of depth (Figure 16). The slope angles derived from the 1-meter resolution DTM show values ranging from 0° to 83° (Figure 17).

The total masked area representing outcropping rock sectors (elaborated as described in section 7.2.4) covers a surface of 1.5 km2 (Figure 18).

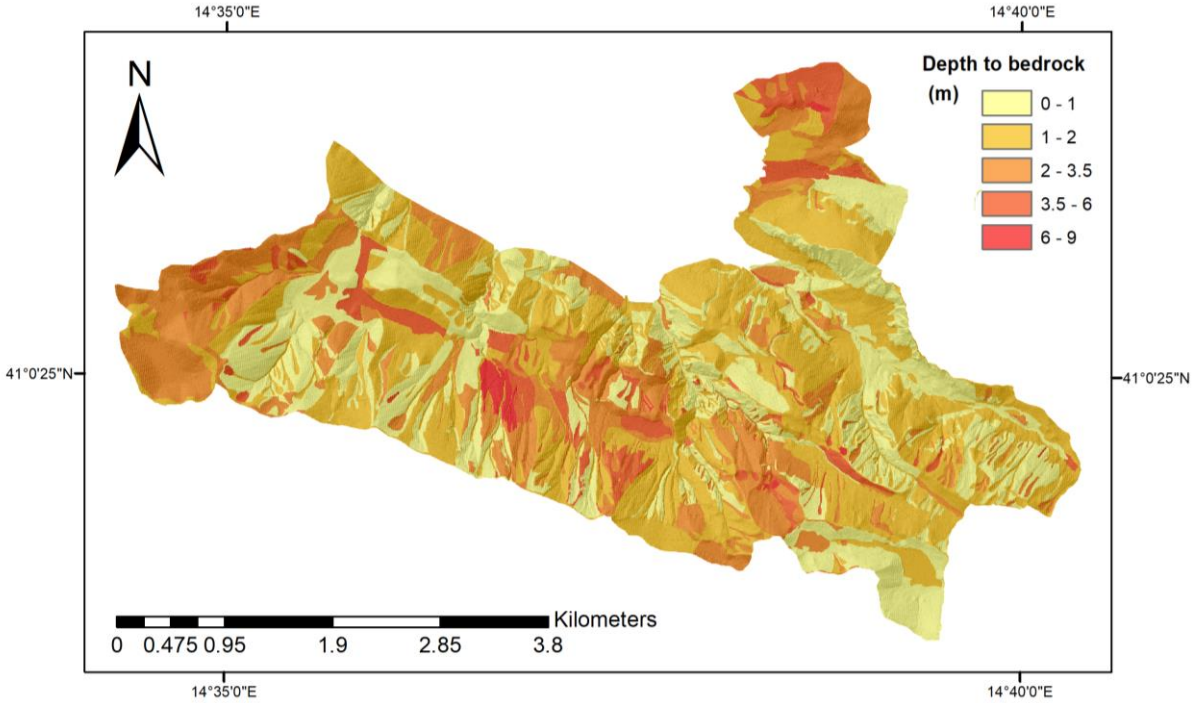

Figure 16. Soil thickness of Cervinara case study.

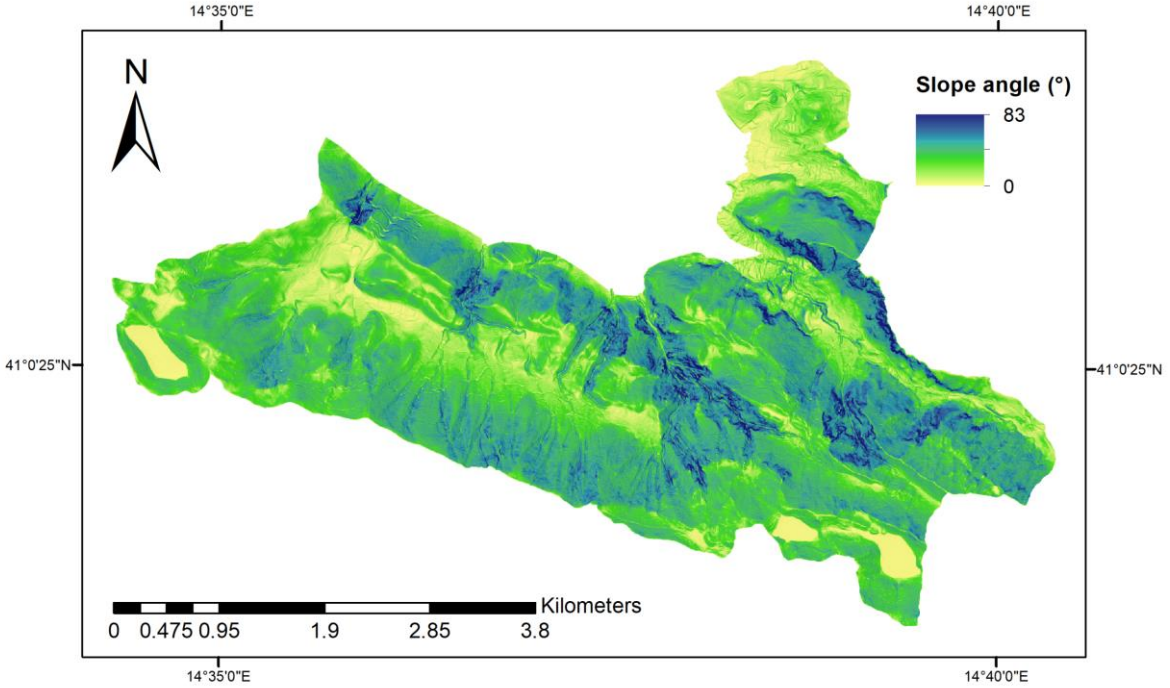

Figure 17. Slope angles of Cervinara case study area.

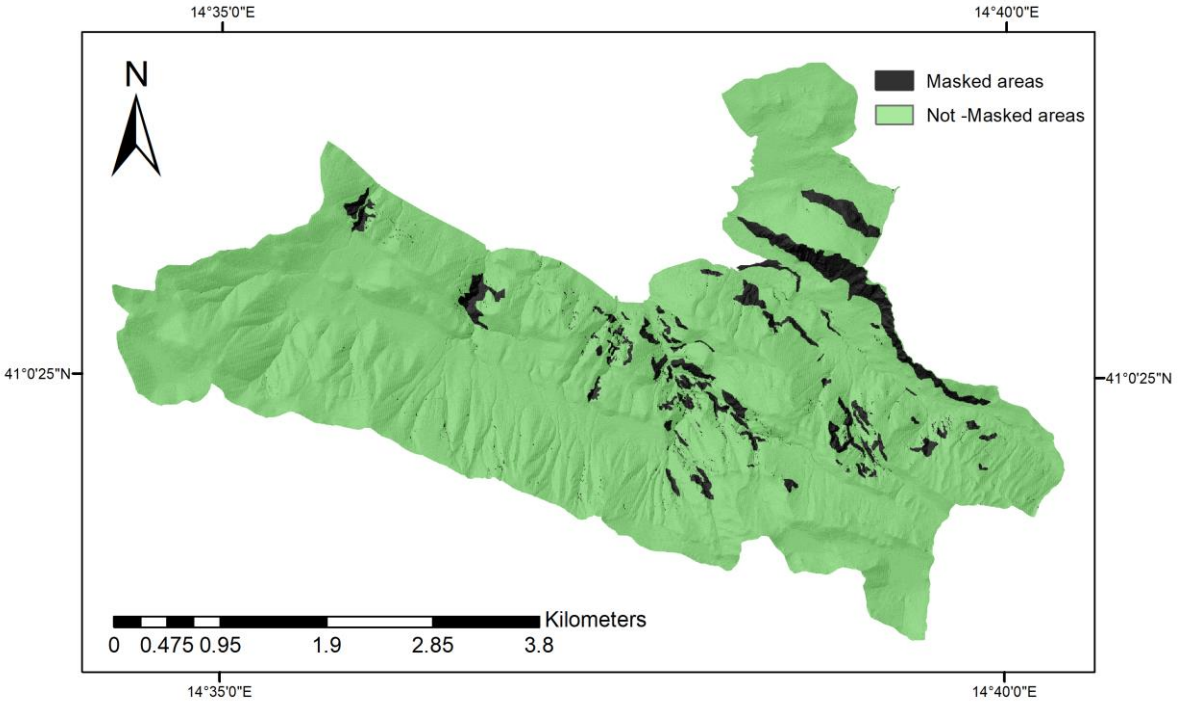

Figure 18. Masked area of Cervinara case study.

The root cohesion values assumed for the area range from a minimum of 0.1 kPa at the north-eastern border in correspondence of suburban areas to a maximum of 20 kPa at the south-eastern border in correspondence of forests dominated by beeches Figure 19).

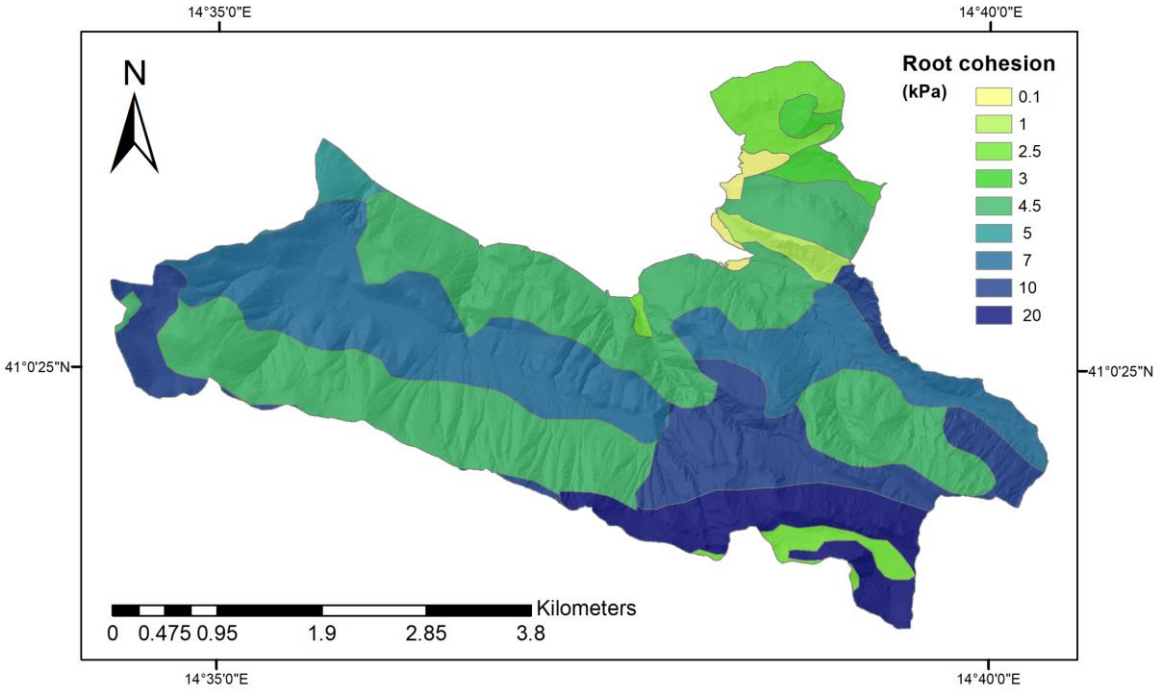

Figure 19. Root cohesion values assumed for the Cervinara case study.

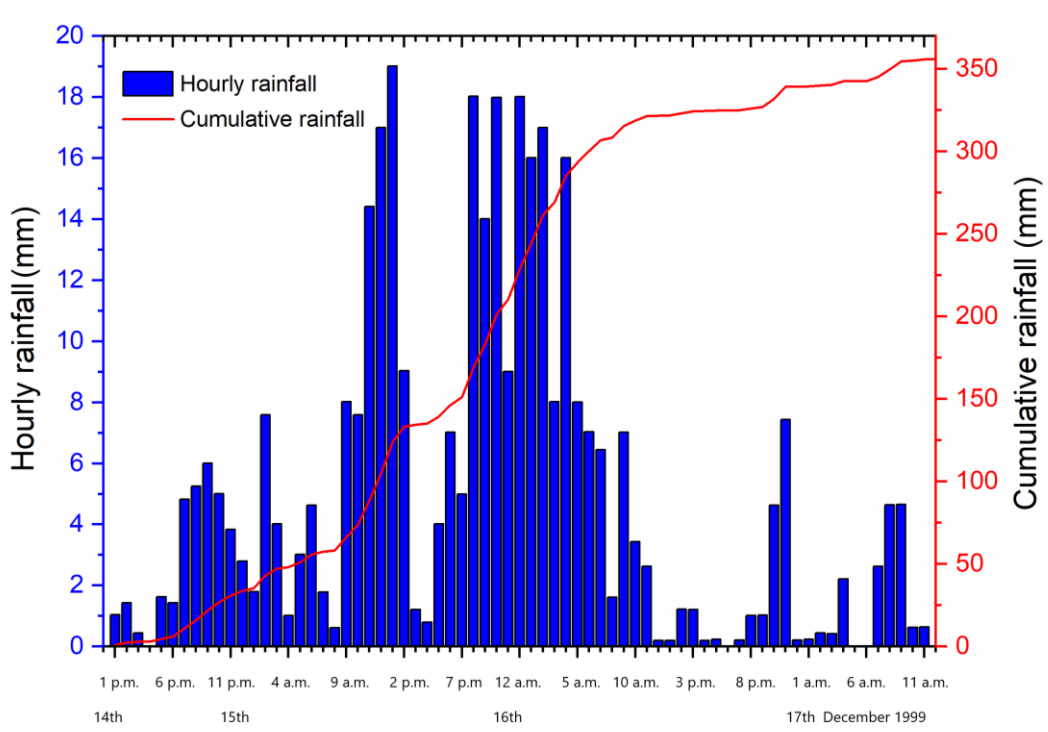

Figure 20. Cervinara case study, hourly and cumulative rainfall of a three days event in December 1999.

The period of rainfall considered for this case study is the time frame of three days at the turn of the night between the 15th December and the 16th December 1999, during which several landslides were triggered by intense rainfall. From the beginning of the considered period (14/12/1999, h 01.00) pm) to the end (17/12/1999, h 12.00) the rain gauge recorded a cumulative rainfall of 356 mm (Figure 20). In the period two sharp rises in the rainfall intensity were recorded: from 9.00 15/12/1999 to 14.00 15/12/1999 in the area were fallen 75 mm of rainfall (on average 12.5 mm/h) with a peak of 19 mm from 13.00 to 14.00; from 18.00 15/12/1999 to 5.00 16/12/1999 a cumulative rainfall of 154 mm was recorded (on average 12.8 mm/h) with three peaks around to 18 mm/h.

The initial soil saturation was inserted equivalent to zero for all the study area (from bedrock to surface).

8 Results of the simulations

Multiple simulations were conducted in both the study areas inserting or not the contribution of the root cohesion (to the parity of all the other input variables), to comparing the results and analysing the effect of the root cohesion on the failure probabilities computed by the model.
During the research process, 11 simulations were completed, of which, 9 relating to the Valle D'Aosta study area and two to the Cervinara study area (Table 4).

Area	Period	Time step	Monte Carlo iterations	Root cohesion	Processing time	FP maps (1h, 24h)
Valle d'Aosta	02.04.2009-30.04.2009	1h	100	No	423.381 min	725 (696, 29)
Valle d'Aosta	02.04.2009-30.04.2009	1h	1000	No	2197.16 min	725 (696, 29)
Valle d'Aosta	02.04.2009-30.04.2009	1h	10000	No	18988.4 min	725 (696, 29)
Valle d'Aosta	02.04.2009-30.04.2009	1h	10	Yes	322.516 min	725 (696, 29)
Valle d'Aosta	02.04.2009-30.04.2009	1h	100	Yes	461.173 min	725 (696, 29)
Valle d'Aosta	02.04.2009-30.04.2009	1h	1000	Yes	2345.83 min	725 (696, 29)
Valle d'Aosta	02.04.2009-30.04.2009	1h	10000	Yes	21039.5 min	725 (696, 29)
Valle d'Aosta	20.05.2010-20.06.2009	1h	1000	No	2471.41 min	802 (770, 32)
Valle d'Aosta	20.05.2010-20.06.2009	1h	1000	Yes	2627.56 min	802 (770, 32)
Cervinara	14.12.1999-17.12.1999	1h	1000	No	22.73 min	76 (72, 4)
Cervinara	14.12.1999-17.12.1999	1h	1000	Yes	25.05 min	76 (72, 4)

Table 4. Data of the simulations.

About the Valle d'Aosta case study, two different periods of rainfall were simulated multiple times, setting the model for different numbers of iterations and inserting or not the root cohesion. Specifically, the event from the 2nd April 2009 to the 30th April 1999 was simulated 7 times, three times not including the root cohesion and setting the number of iterations to 100, 1000, 10000, and 4 times including the root cohesion and setting the number of iterations to 10, 100, 1000, 10000. The

event from the 20th May 2010 to the 20th June 2010 was simulated two times, setting both the times the number of iterations to 1000, with the difference of inserting or not the root cohesion.

About the Cervinara case study, one rainfall event was simulated (14.12.1999 – 17.12.1999) two times, with 1000 Monte Carlo iterations in both cases, and inserting or not the root cohesion.

In all the simulations, both the Valle d'Aosta and Cervinara case studies, the model was set to compute the failure probability with time steps of 1 hour, according to the time resolution of the rainfall data provided to the model.

Area	Event	Simulation (root cohesion, iterations)	Sum	Mean	Minimum	Maximum
Valle d'Aosta	2009	No, 100	2082630	71815	52229	299607
		No, 1000	1452730	50094	31857	240611
		No, 10000	1381390	47634	28614	237416
		Yes, 10	5067920	174756	148883	489794
		Yes, 100	2082760	71819	52114	299641
		Yes, 1000	1452540	50088	31864	240775
		Yes, 10000	1381410	47635	28611	237404
Valle d'Aosta	2010	No, 1000	1650370	51574	31359	146212
		Yes, 1000	1649960	51561	31389	146012
Cervinara		No, 1000	809	202	0	463
		Yes, 1000	808	202	0	462

Table 5. Count of unstable pixels (pixels with a daily max failure probability higher than 75%) of each simulation. The "Sum" is the total count over the period, "Mean" the average unstable pixels per day, "Minimum" represents the count of unstable pixels of the most stable day during the period, "Maximum" is the count of unstable pixels of the most unstable day during the period.

Every simulation of the Valle d'Aosta-2009 event (being a period of 29 days) produced 725 failure probability maps, of which 696 representing the FP of every pixel of the area for each time step, and 29 representing the daily max FP of each pixel (Table 4). The simulations of the Valle d'Aosta-2010 event (32 days) produced 802 failure probability maps each, of which 770 FP hourly maps, 32 FP daily maps. The fastest simulation was that of the 2009 event with the root cohesion and set to 10 iterations, with a processing time of 322.5 minutes (~ 5 hours). The simulation that instead needed the longest time to finished was the 2009 event with the root cohesion set to 10000 iterations, with a processing time of 21039.5 minutes (~ 350 hours). Every simulation of the Cervinara event (72 hours) produced

76 failure probability maps, 72 FP hourly maps and 4 FP daily maps. The simulation without the root cohesion took 22,7 minutes; the simulation with the root cohesion took 25.1 minutes instead.

In the Figures from 21 to Figure 27, and from Figure 29 to Figure 32, the trend of unstable pixels (pixel with a daily max failure probability higher than 75%) during the period of each simulation performed is shown, in the graphs the daily and cumulative rainfall are also reported. For the Valle d'Aosta study area, the rainfall data reported represent the average rainfall per polygon recorded by the rain gauges of the study area (section 7.1.5) during the period of the simulation. For the Carvinara case study, the reported rainfall refers to the data recorded by the only rain gauge present in the area (section 7.2.5).

8.1 Valle d'Aosta case study 2009 event

The Figures from Figure 21Figure 23 represent the simulations of the 2009 event (02.04.2009-30.04.2009), in which the contribution of root cohesion was not considered, and the number of iterations changes from 100 to 1000 and 10000.

In the simulation of the 2009 event- 100 iterations without the root cohesion (Figure 21), the model computed an overall of 2.08263E6 unstable pixels, the minimum number per day of unstable pixels was 52229 (04.04.2009), the maximum 299607 (27.04.2009), in average 71815 unstable pixels were found per day.

The simulation of the 2009 event -1000 iterations without the root cohesion (Figure 22) counts a sum of 1.45273E6 unstable pixels over the period, a minimum per day of unstable pixels of 31857 (04.04.2009), a maximum of 240611 (27.04.2009), on average the model detected 50094 unstable pixels per day.

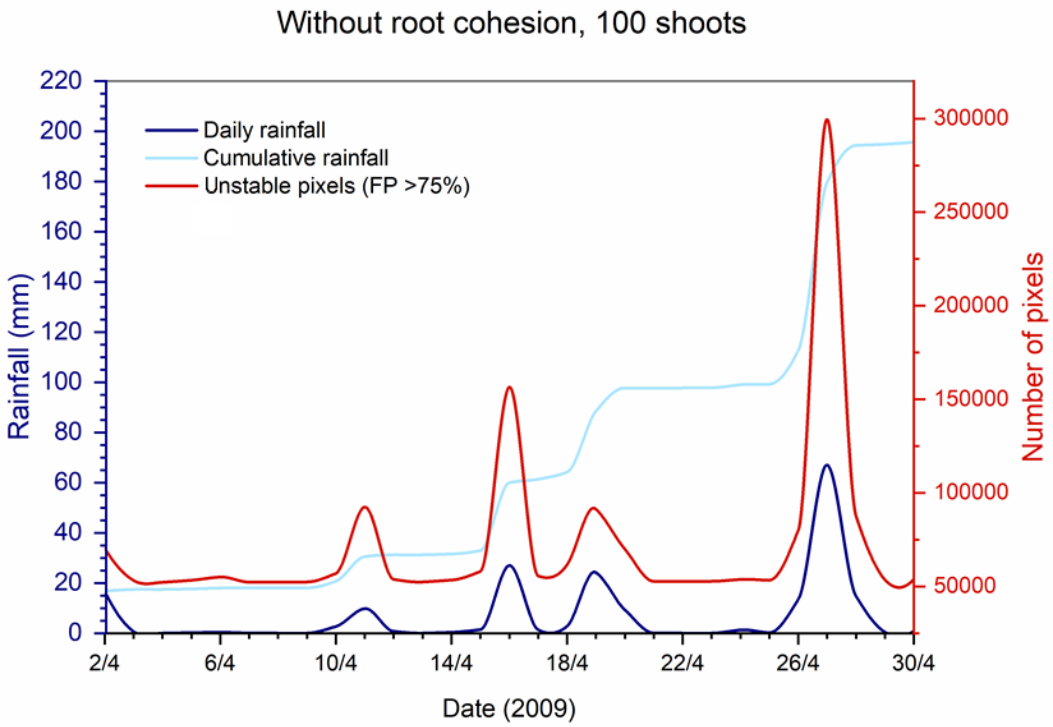

Figure 21. Unstable pixels (pixels with a daily max Failure Probability FP higher than 75%) of the simulation in which the root cohesion was not considered, 2009 event, 100 Monte Carlo shoots.

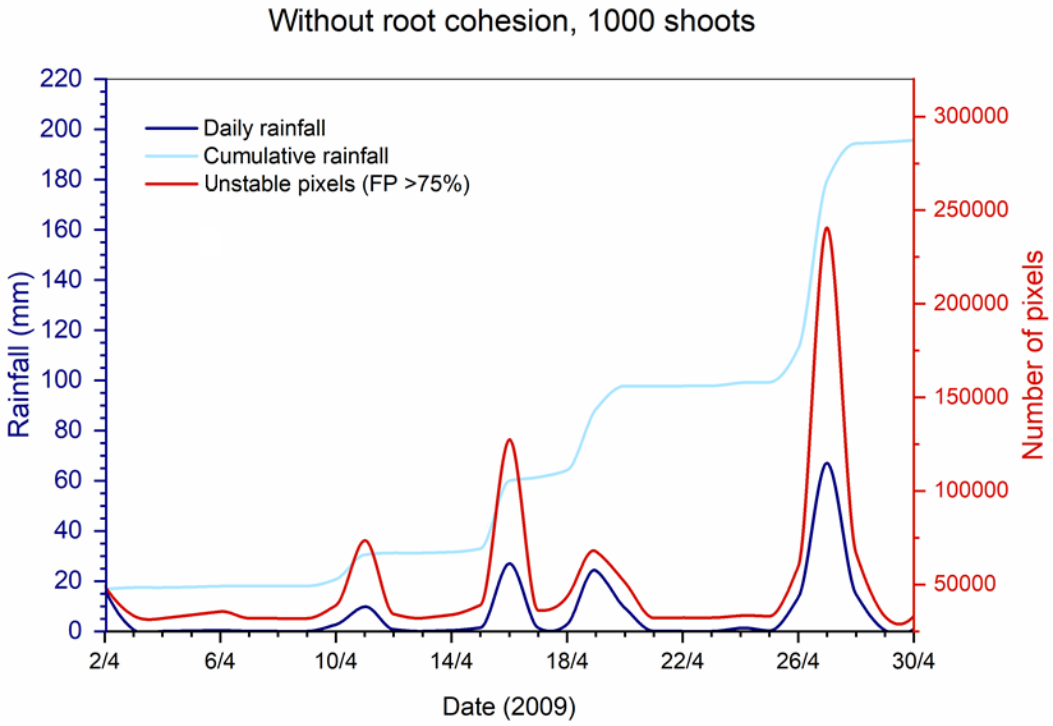

Figure 22. Unstable pixels (pixels with a daily max Failure Probability FP higher than 75%) of the simulation in which the root cohesion was not considered, 2009 event, 1000 Monte Carlo shoots.

In the simulation of the 2009 event -10000 iterations without the root cohesion (Figure 23), the model found an overall of 1.38139E6 unstable pixels during the period, a minimum of 28614 in the same most stable day of the previous simulations discussed above (04.04.2009), a maximum of 237416 (27.04.2009), and an average of 47634 unstable pixels per day.

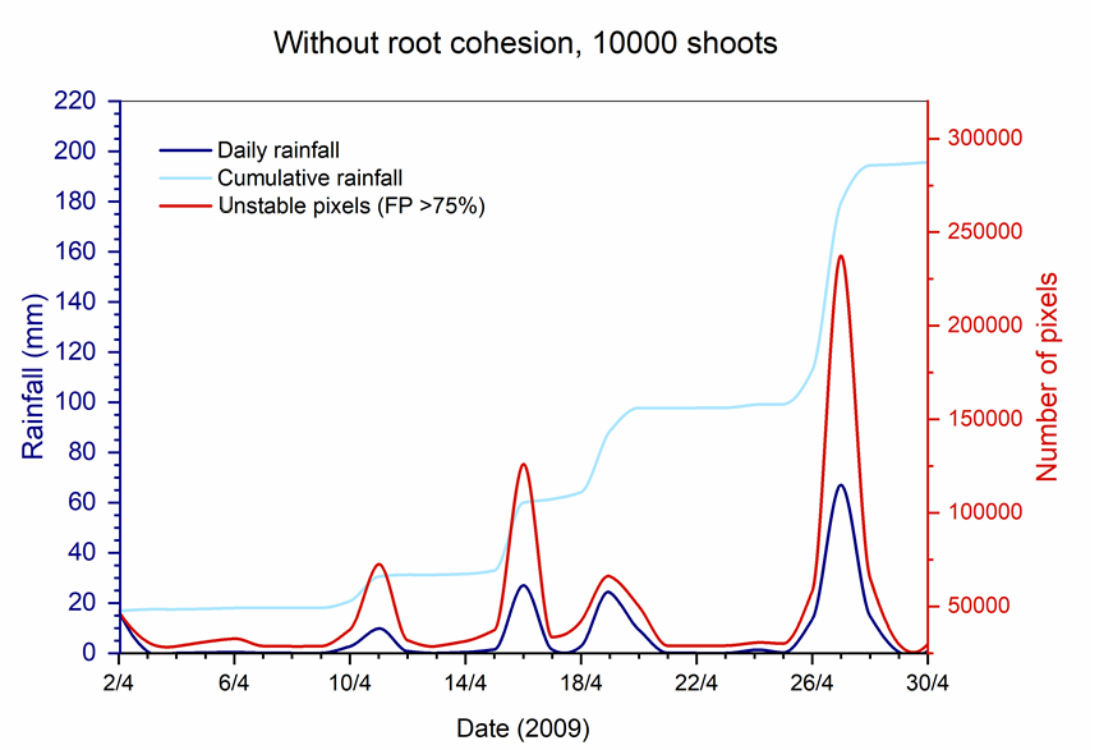

Figure 23. Unstable pixels (pixels with a daily max Failure Probability FP higher than 75%) of the simulation in which the root cohesion was not considered, 2009 event, 10000 Monte Carlo shoots.

The Figures from Figure 24 to Figure 27 show the simulations of the 2009 event (02.04.2009-30.04.2009), in which the contribution of root cohesion was considered instead, and the number of iterations was set to 10, 100, 1000 and 10000.

During the simulation of the 2009 event -10 iterations with the root cohesion (Figure 24. Unstable pixels (pixels with a daily max Failure Probability FP higher than 75%) of the simulation in which the root cohesion was considered, 2009 event, 10 Monte Carlo shoots. , the model found an overall of 5.06792E6 unstable pixels, a minimum of 148883 (04.04.2009) and a maximum of 489794 (27.04.2009), on average the unstable pixels per day were 174756.

In the simulation of the 2009 event -100 iterations with the root cohesion (Figure 25), the total unstable pixels over the period were 2.08276E6 instead, the minimum 52114 (04.04.2009), the maximum 299641 (27.04.2009) and the average per day were 71819.

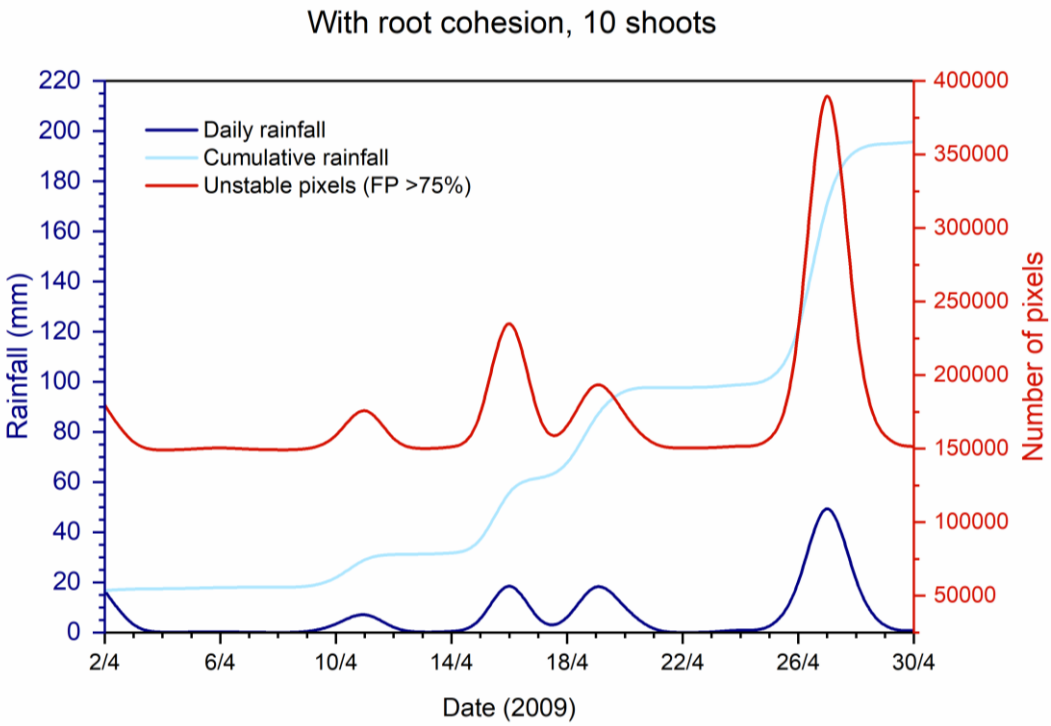

Figure 24. Unstable pixels (pixels with a daily max Failure Probability FP higher than 75%) of the simulation in which the root cohesion was considered, 2009 event, 10 Monte Carlo shoots.

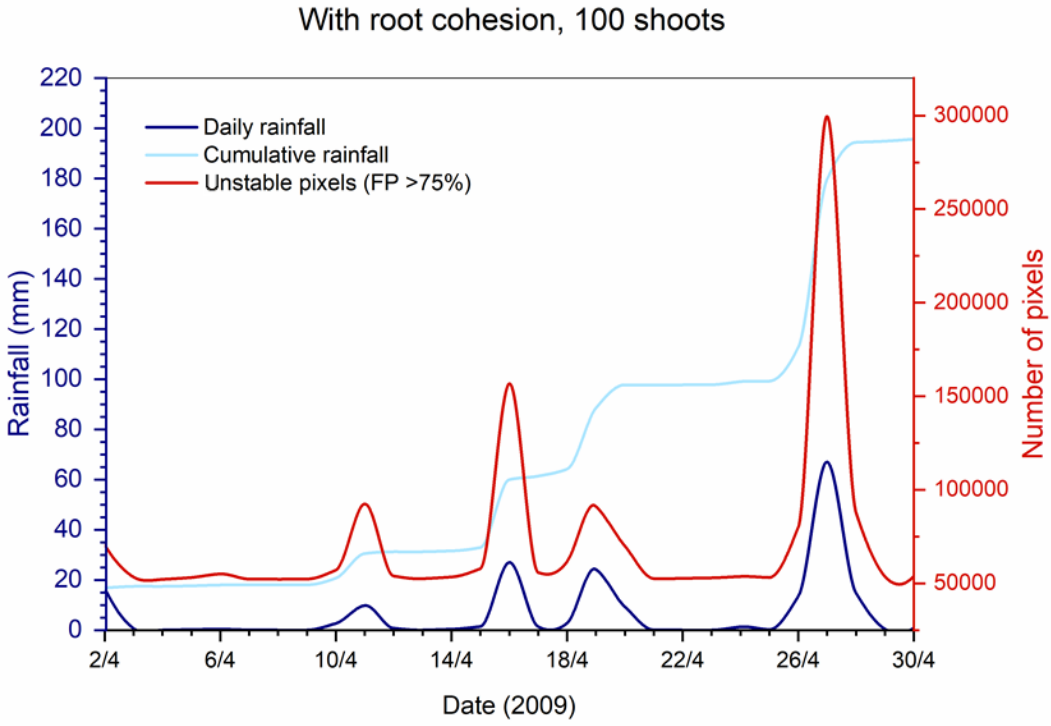

Figure 25. Unstable pixels (pixels with a daily max Failure Probability FP higher than 75%) of the simulation in which the root cohesion was considered, 2009 event, 100 Monte Carlo shoots.

The simulation of the 2009 event -1000 iterations with the root cohesion (Figure 26) counts a sum of 1.45254E6 unstable pixels over the period, a minimum per day of unstable pixels of 31864 (04.04.2009), a maximum of 240775 (27.04.2009), on average the model detected 50087 unstable pixels per day.

In the simulation of the 2009 event -10000 iterations with the root cohesion (Figure 27), the model found an overall of 1. 1.38141E6 unstable pixels during the period, a minimum of 28611 (04.04.2009), a maximum of 237404 (27.04.2009), and an average of 47634 unstable pixels per day.

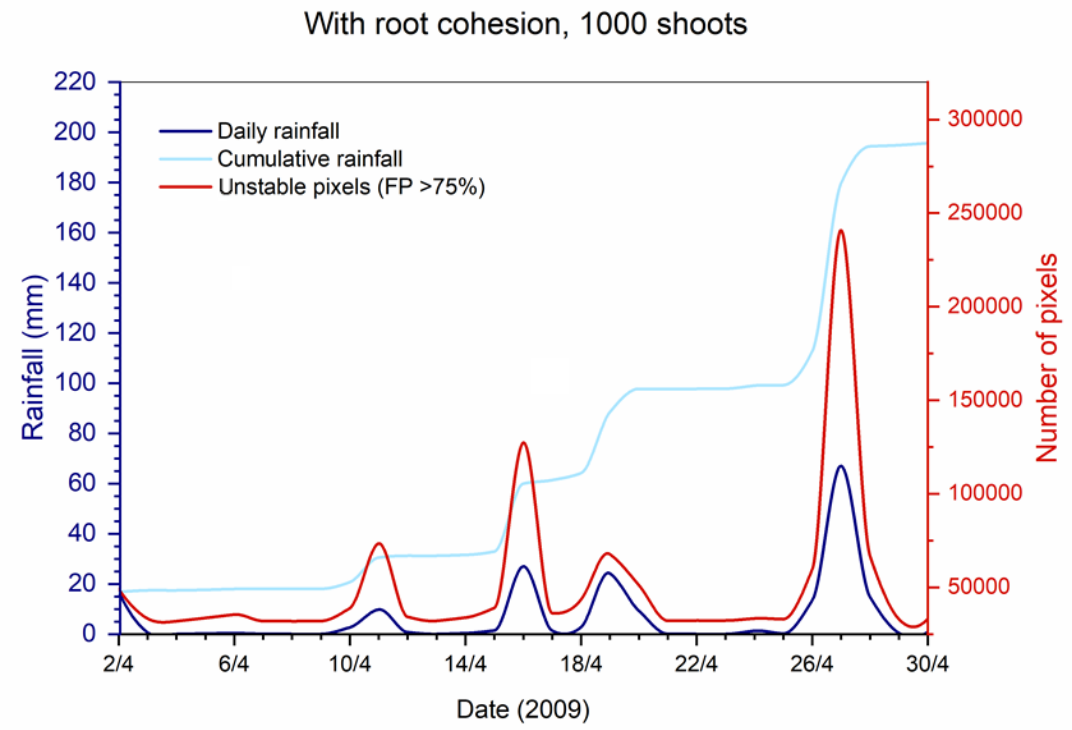

Figure 26. Unstable pixels (pixels with a daily max Failure Probability FP higher than 75%) of the simulation in which the root cohesion was considered, 2009 event, 1000 Monte Carlo shoots.

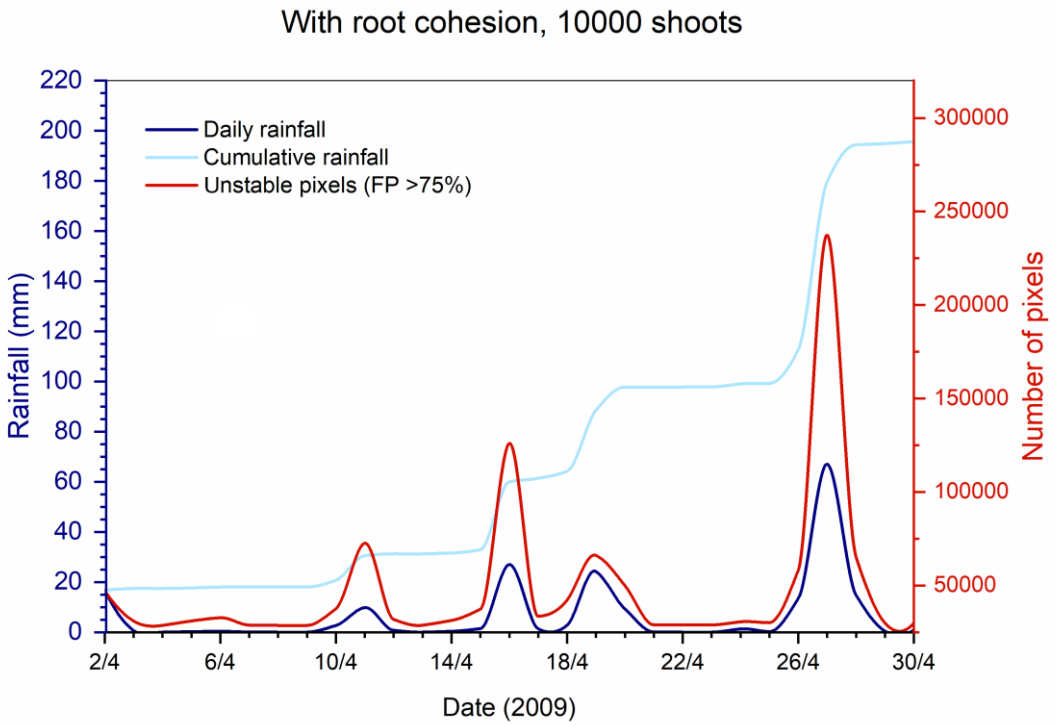

Figure 27. Unstable pixels (pixels with a daily max Failure Probability FP higher than 75%) of the simulation in which the root cohesion was considered, 2009 event, 10000 Monte Carlo shoots.

8.2 The optimal number of Monte Carlo iterations

Before proceeding with all the other planned simulations, a study on the preferable number of Monte Carlo iterations was performed. The Monte Carlo iterations performed by the chosen forecasting model (HIRESSS) to manage the spatial uncertainty of the input parameters is a fundamental aspect of the forecast procedure, the setting of which strongly affects the resulting failures probabilities. The higher the number of iterations, the higher the reliability of the forecasts. On the other hand, a higher number of iterations considerably slow down the processing calculations, so that the question here is finding the best compromise between processing time and reliability of the results.

In order to find the appropriate number of iterations in the context of the present research, four simulations of the 2009 event (02/04/2009-30/04/2009, rainfall time step 1 hour, see section 7.1.6) were performed with the same input parameters (referring to the Valle d'Aosta study area) varying the number of iterations (10, 100, 1000, 10000 shoots). The simulation results are then compared, considering the amount of unstable pixels computed in the three cases for the same days of the event and the processing time (Figure 28).

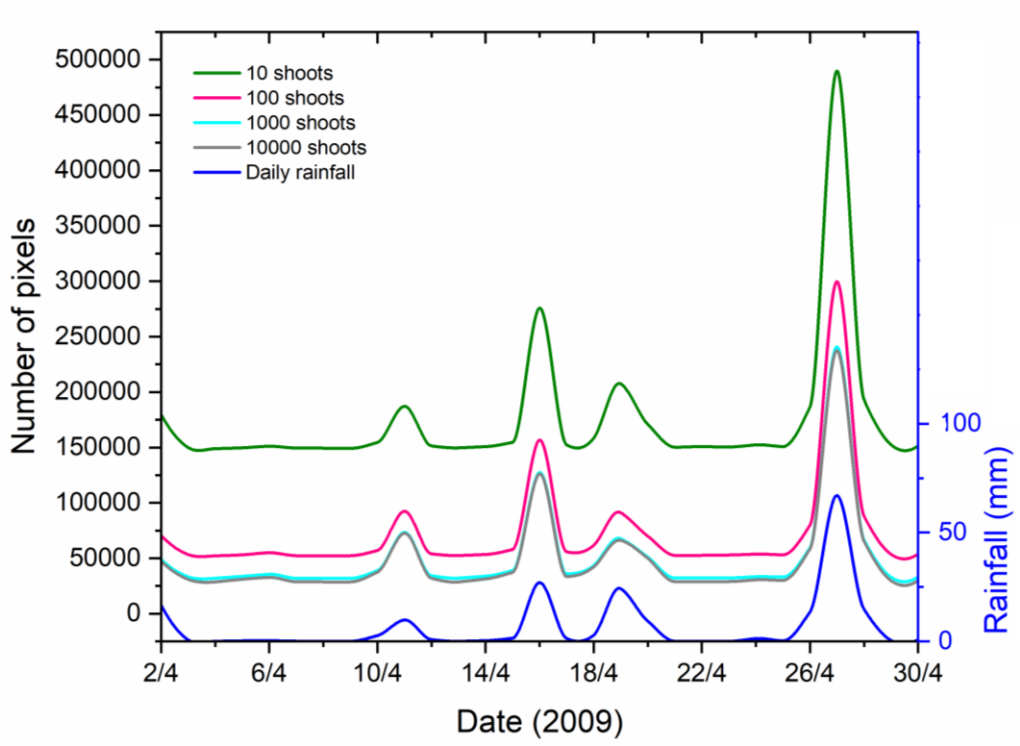

Figure 28. Comparison between simulations with a different number of Monte Carlo iterations (FP is "failure probability").

The difference between the 10-simulation and the 100-simulation is about 100000 fewer unstable pixels for the latter, while between the 100-simulation and the 1000-simulations, there are 25000 pixels of difference on average (also in this case the simulation obtained through a higher number of iterations shows less unstable pixels)(Figure 28). Differently, the differences between the 1000-simulation and the 10000-simulation are so little to be considered negligible, against a considerable difference in terms of processing time. Indeed, the 1000-simulation needs 2346 minutes (39 hours) to be completed, while the 10000-simulation took 21039 minutes (350 hours). The very few differences between the two (so the convergence of the results) and on the contrary the very different processing times lead to the choice of 1000 iterations for the successive simulations. The major part of data analysis and elaborations was performed on the 1000-simulations.

8.3 Valle d'Aosta case study 2010 event

The simulation of the 2010 event -1000 iterations without the root cohesion (Figure 29) counts a sum of 1.65037E+06 unstable pixels over the period, a minimum per day of unstable pixels of 31359 (25.05.2010), a maximum of 146212 (16.06.2010), the model detected on average 51574 unstable pixels per day.

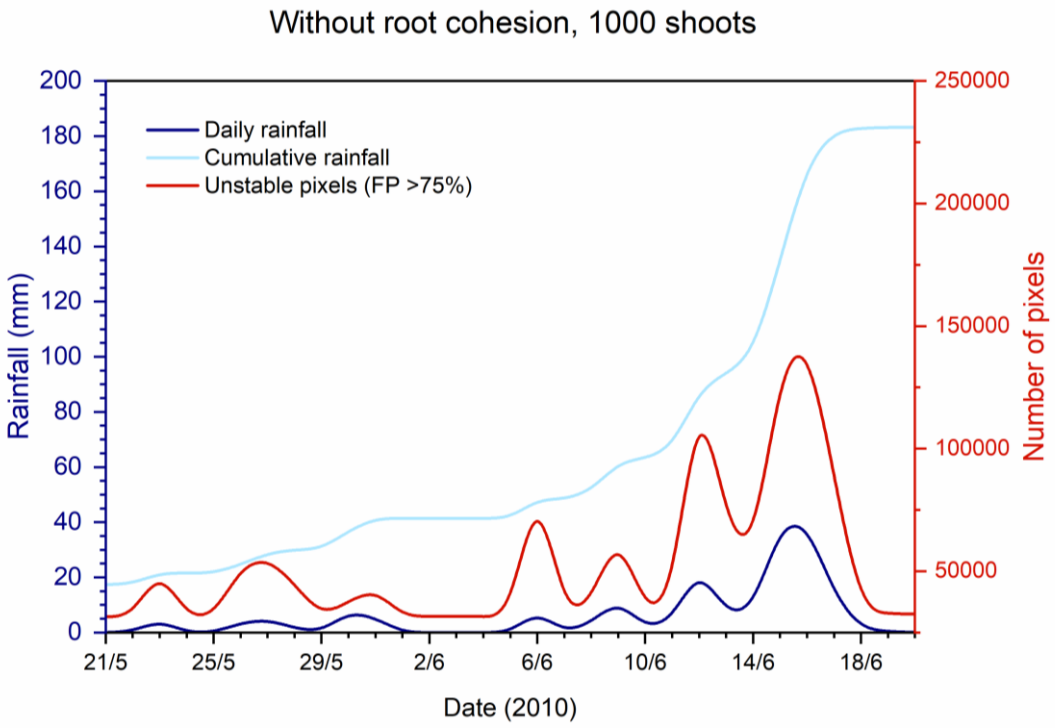

Figure 29. Unstable pixels (pixels with a daily max Failure Probability FP higher than 75%) of the simulation in which the root cohesion was not considered, 2010 event, 1000 Monte Carlo shoots.

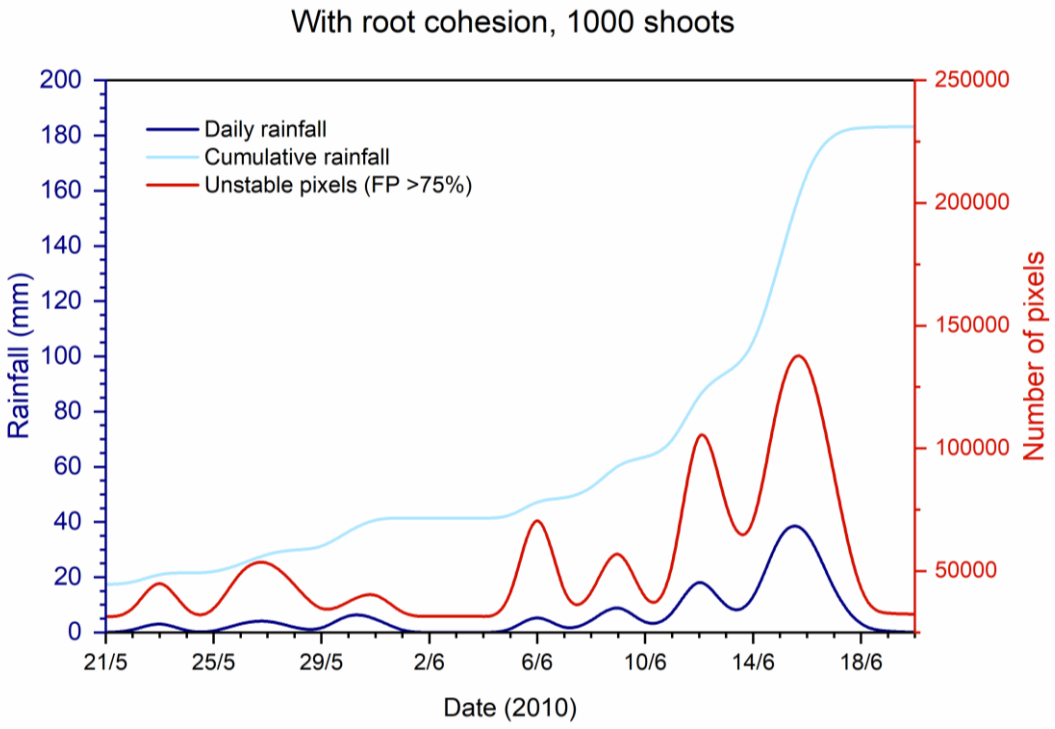

Figure 30. Unstable pixels (pixels with a daily max Failure Probability FP higher than 75%) of the simulation in which the root cohesion was considered, 2010 event, 1000 Monte Carlo shoots.

The model found in the simulation of the 2010 event -1000 iterations with the root cohesion (Figure 30) 1.64996E+06 unstable pixels over the period, a minimum per day of 31389 (25.05.2010), a maximum of 146012 (16.06.2010), and a mean of 51561 unstable pixels per day.

8.4 Cervinara case study

The Cervinara case study simulations (without and with the root cohesion, Figure 31 and Figure 32) show almost equivalent trend regarding the count of unstable pixels during the period. The model found a sum of 809 unstable pixels in the simulation without the root cohesion and 808 in the simulation with the root cohesion. The difference is represented by the maximum (recorded for both in the 16th December 1999): 463 in the simulation without the root cohesion, 462 in the simulation with the root cohesion. In both cases, the minimum was 0 (14th December 1999).

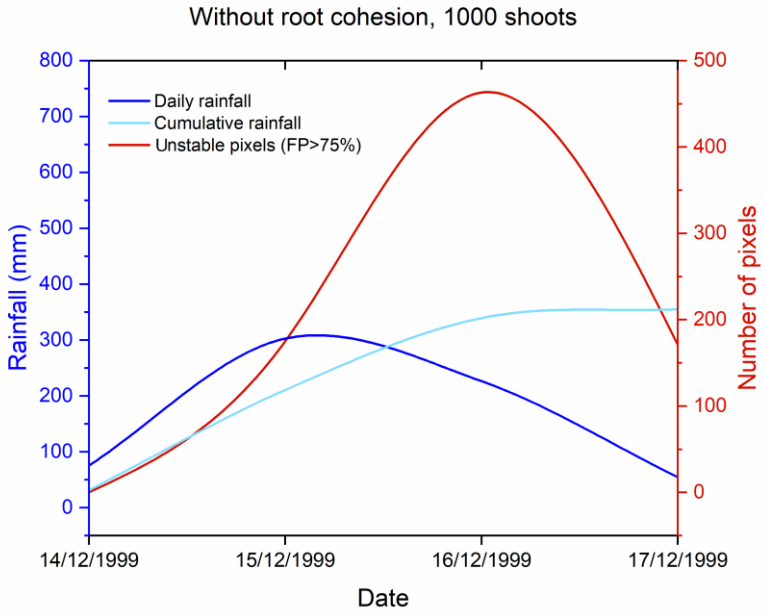

Figure 31. Unstable pixels (pixels with a daily max Failure Probability FP higher than 75%) of the simulation in which the root cohesion was not considered, 1000 Monte Carlo iterations.

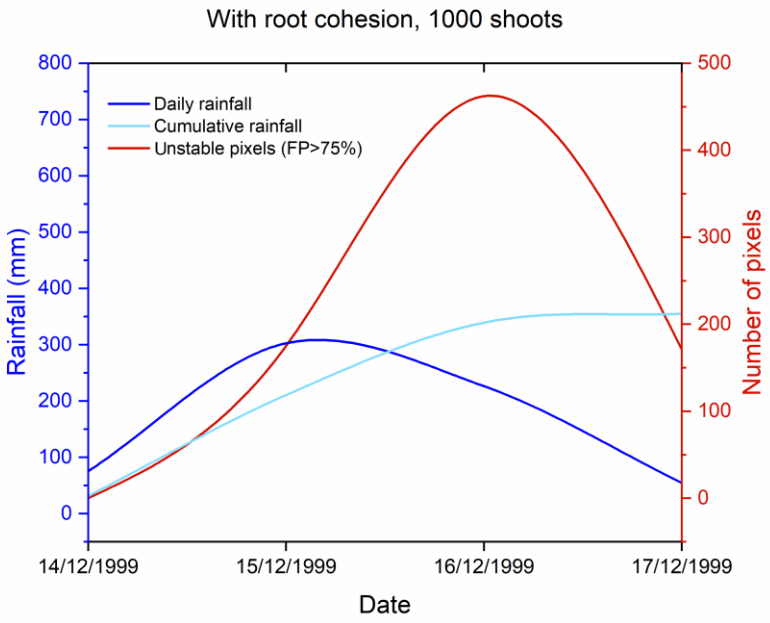

Figure 32. Unstable pixels (pixels with a daily max Failure Probability FP higher than 75%) of the simulation in which the root cohesion was considered, 1000 Monte Carlo iterations.

9 Discussions

The results of the simulations were in the first place analysed from the point of view of the unstable pixels trend during the periods. The precautionary value of 1.2 for the factor of safety and the 75% for the failure probability were chosen as thresholds to consider unstable a pixel. During the iterative process, for each pixel and time step, the model computes the factor of safety for a certain number of times (configurable). The model was set to consider unstable a pixel when the calculated factor of safety results lower than the value of 1.2. If a pixel shows a failure probability higher than the 75% in a certain time step means that the model found more than 75 times out of 100 a factor of safety lower than 1.2 for that pixel in that time step.

The failure probability threshold to consider unstable a pixel should be set from case to case depending on the purposes of the slope stability analysis. The main scope of the present study was to analyse the effect of the root cohesion evaluated as exposed in the text (6.1) on the simulation results, mainly by means of comparative analyses of the simulations. The threshold of 75% was chosen based on previous works on HIRESSS applications (Rossi, 2013; Salvatici et al., 2108); in the present study, it was used for describing and representing the trend of the simulations (Section 8) and in some comparative analyses described further in the text. But it is worthwhile mentioning here that other comparative analyses have also been carried out considering the entire spectre of the failure probabilities, to better explore the behaviour of the simulations with and without the root cohesion.

The trends of unstable pixels (pixels with a daily max Failure Probability FP higher than 75%) reported in the previous section together with daily and cumulative rainfall allow first of all to have a general view on the behaviour of the model. Beside the expectable peaks of unstable pixels in correspondence of rainfall peaks, we can observe in the graphs of the Valle d'Aosta case study a particular behaviour of the model in case of two close-up rainfall peak. When two close-up rainfall peaks of comparable size occur, in correspondence of the second rainfall peak there is a less intense increase in the number of unstable pixels compared to the answer of the model for the first one (2009-event, rainfall peaks of the 16th April and the 19th April; 2010-event, rainfall peaks of the 6th and the 9th June). Differently, when the second peak is considerably higher than the first, the trend of unstable pixels returns to reflect the rainfall path closely. This behaviour reflects the physical models (geotechnical and hydrological) of HIRESSS, shaped on the dynamics of the rainfall triggered shallow landslides, for which abrupt rainfall after days of drought have a higher impact compared to the same amount of precipitations following days of rainfall. However, when the rainfall is abundant, even if it follows other days of precipitations, the impact returns to be high for the trigger of shallow landslides.

Regarding the aspects that more closely concern the present study, the comparison of count (Table 5, Section 8) and trend of unstable pixels of the simulations (Figure 21-Figure 32, Section 8) with and without the root cohesion represented the first step to analyse the effect of the root cohesion on the failure probabilities computed by the model. Since only the comparisons between simulations with an equivalent number of iterations and referring to the same area and rainfall period are meaningful in the context of this analysis, the comparisons can concern the three couples of the Valle d'Aosta 2009-event (100, 1000, 10000 iterations), the couple of the Valle d'Aosta 2010-event (1000 iterations) and couple of the Cervinara event (1000 iterations).

The effect of the root reinforcement was inserted into the model in the form of an additional cohesion (Section 6.2.2). In the comparison of the simulation with or without the root cohesion, we expected to find a higher number of unstable pixels in the simulations in which the contribution of the root cohesion was not considered. Considering the total unstable pixels counted by the model during the simulations, there were more unstable pixels in the simulation without the root cohesion in three comparisons out of five (Valle d'Aosta 2009-event 1000 iterations, Valle d'Aosta 2010-event and Cervinara event). In the other two cases (Valle d'Aosta 2009-event 100 and 10000 iterations) the model found a higher overall number of unstable pixels in the simulation in which the contribution of the root cohesion was considered. Even considering the mean, maximum and minimum values of unstable pixels per day (Table 5, Section 8), a higher tendency to the instability of the simulations without the root cohesion did not emerge. Examining the results through this approach and considering the threshold of the 75%, the expectations have been only partially respected.

After the preliminary phase of analyses described above, the results of the simulations have been explored following different approaches.

The results have been compared i) from the point of view of the difference in the failure probabilities pixel by pixel between the simulations with and without the root cohesion in rainy and no rainy days; ii) analysing the trend of the unstable pixels difference (count of unstable pixels of the without root cohesion-simulation minus the count of the with root cohesion-simulation) during the whole period of the simulations in different subareas of the case studies; iii) examining the trend of the failure probabilities (comparison of the number of unstable pixels for each failure probability of the simulations with and without the root cohesion) in rainy and no rainy days in different subareas of the case studies. The approaches are detailed in the next dedicated sections.

9.1 Differences in the failure probabilities pixel by pixel

For each study area, one “no rainy” day and one rainy day were selected to analyse the difference between the simulations with or without the root cohesion in terms of failure probability (FP) at the level of each pixel. For each day, the raster map of the max FP computed by the model for each pixel in the simulation without the root cohesion and the equivalent raster map of the simulation with the root cohesion were extracted from the results. Then a raster difference was performed, subtracting the FP of each pixel of the map with the root cohesion to the FP of the correspondent pixel of the map without the root cohesion, so that obtaining the difference in the max failure probability computed by the model. Finally, the mean difference at the basin level was calculated.

9.1.1 Valle d’Aosta case study

For the Valle d’Aosta case study two days of the 2009-event were selected, the 25th April as the “no rainy” day and the 27th April as the rainy day. The procedure to obtain the difference of the daily max failure probability between the simulations with or without the root cohesion was performed twice for this case study, considering the simulation-1000 iterations and the simulation-10000 iterations.

The figures from Figure 33 to Figure 40 show the distribution of the daily max failure probability computed by the model in the following different days and simulations:

- 25.04.2009, 1000 iterations, without the root cohesion;
- 27.04.2009, 1000 iterations, without the root cohesion;
- 25.04.2009, 1000 iterations, with the root cohesion;
- 27.04.2009, 1000 iterations, with the root cohesion;
- 25.04.2009, 10000 iterations, without the root cohesion;
- 27.04.2009, 10000 iterations, without the root cohesion;
- 25.04.2009, 10000 iterations, with the root cohesion;
- 27.04.2009, 10000 iterations, with the root cohesion.

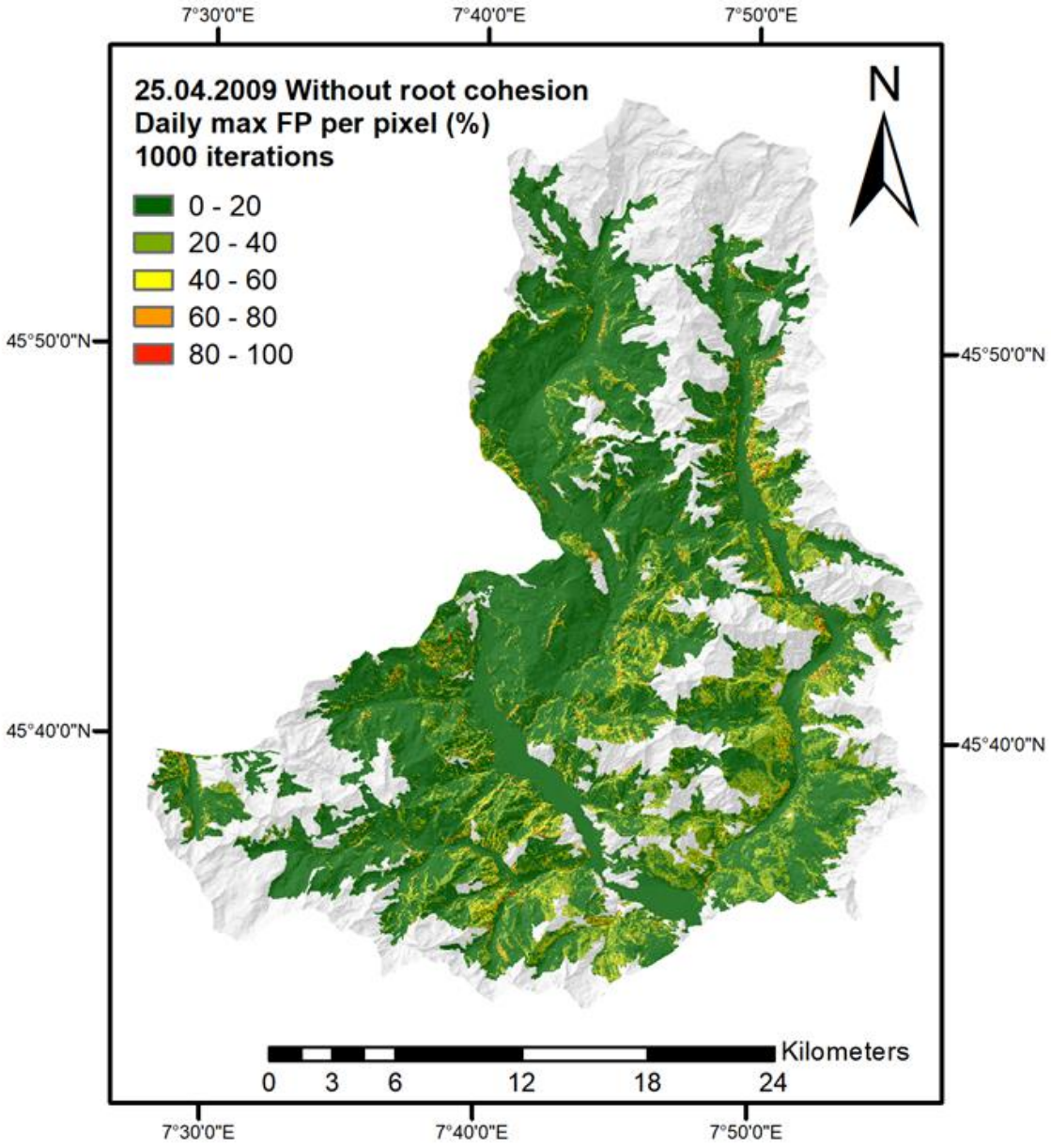

Figure 33. Max Failure Probability (FP) computed by the model for each pixel in the not rainy day (25.04.2009), simulation without the root cohesion, 1000 Monte Carlo iterations.

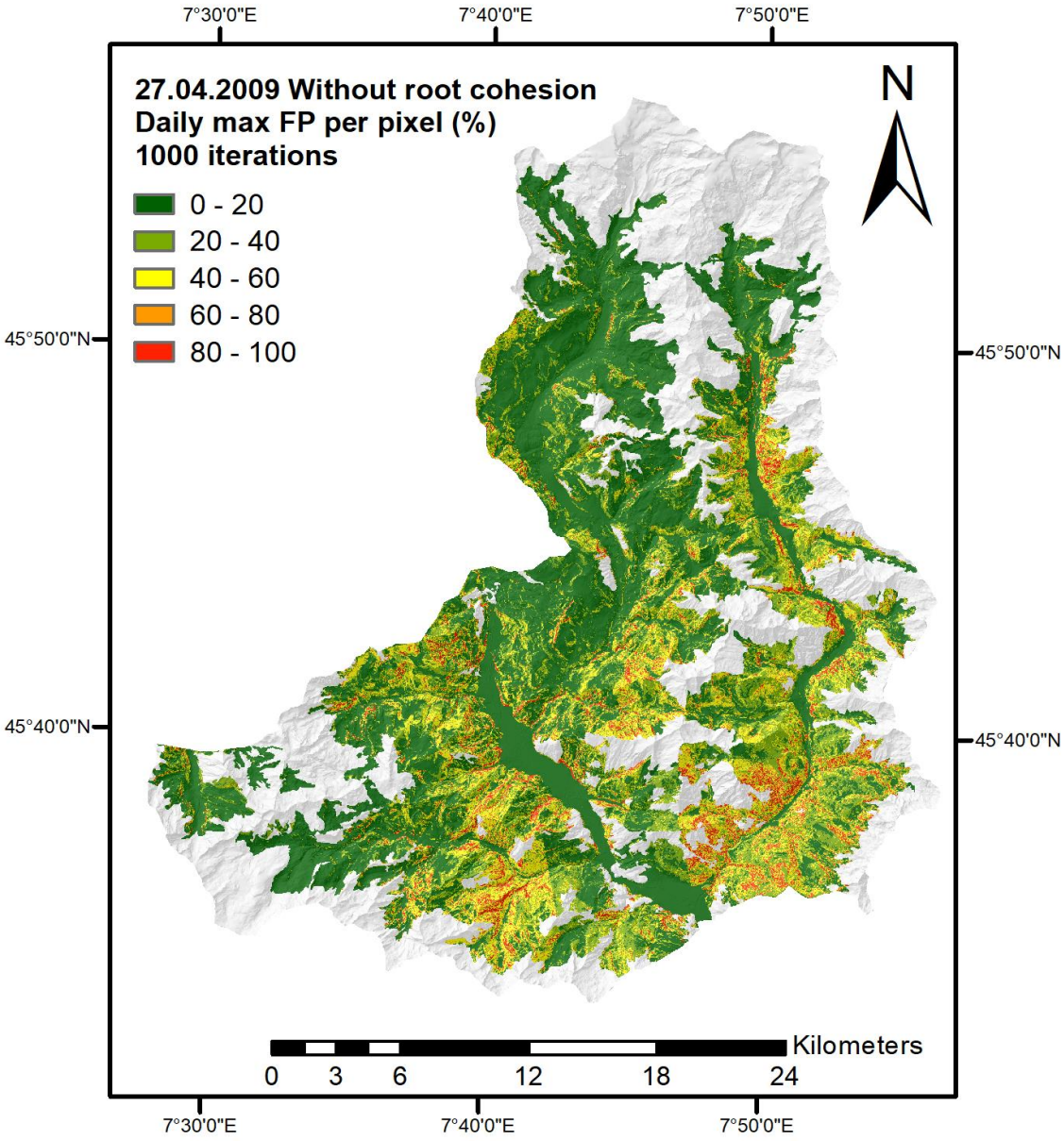

Figure 34. Max Failure Probability (FP) computed by the model for each pixel in the rainy day (27.04.2009), simulation without the root cohesion, 1000 Monte Carlo iterations.

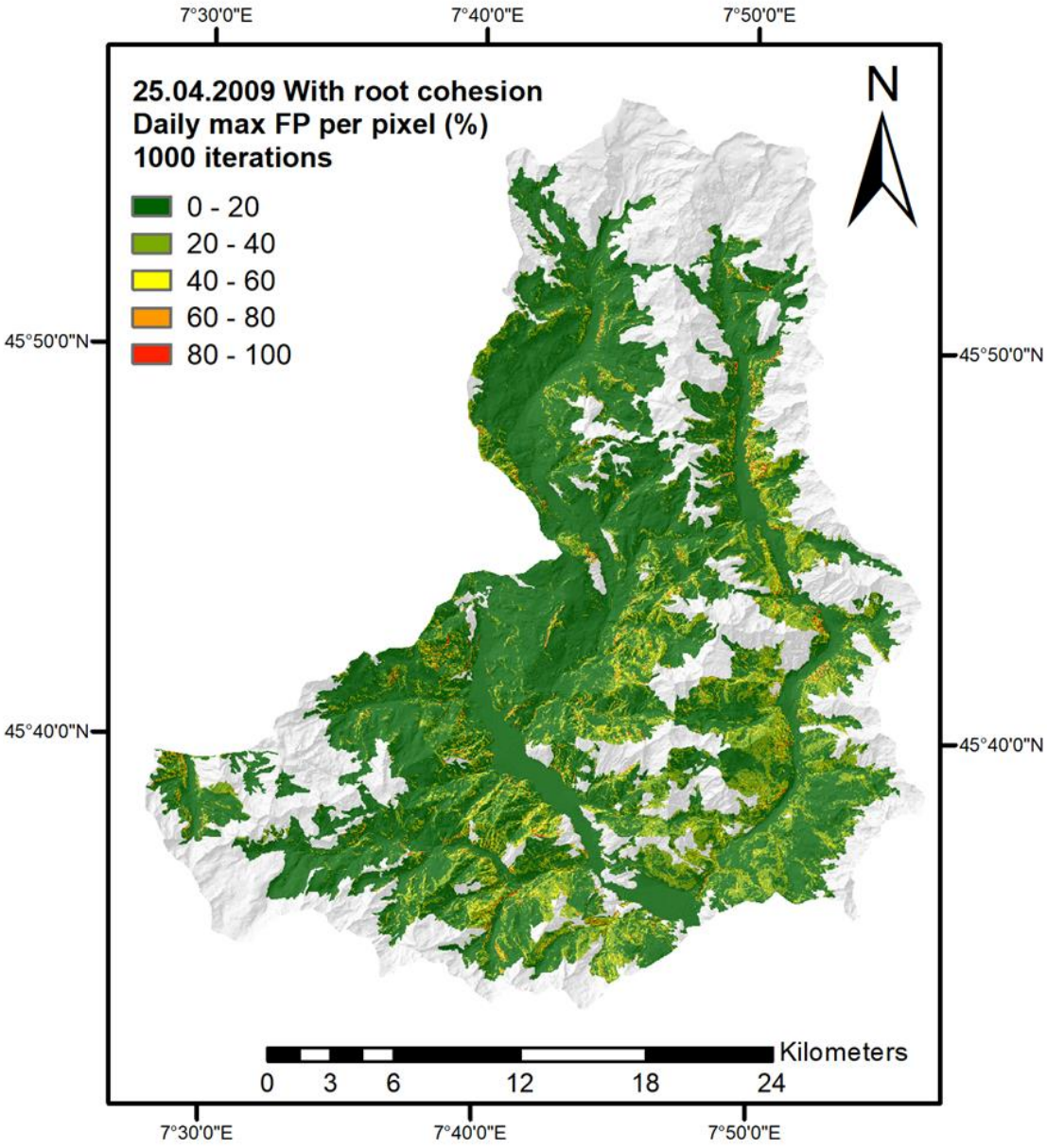

Figure 35. Max Failure Probability (FP) computed by the model for each pixel in the not rainy day (25.04.2009), simulation with the root cohesion, 1000 Monte Carlo iterations.

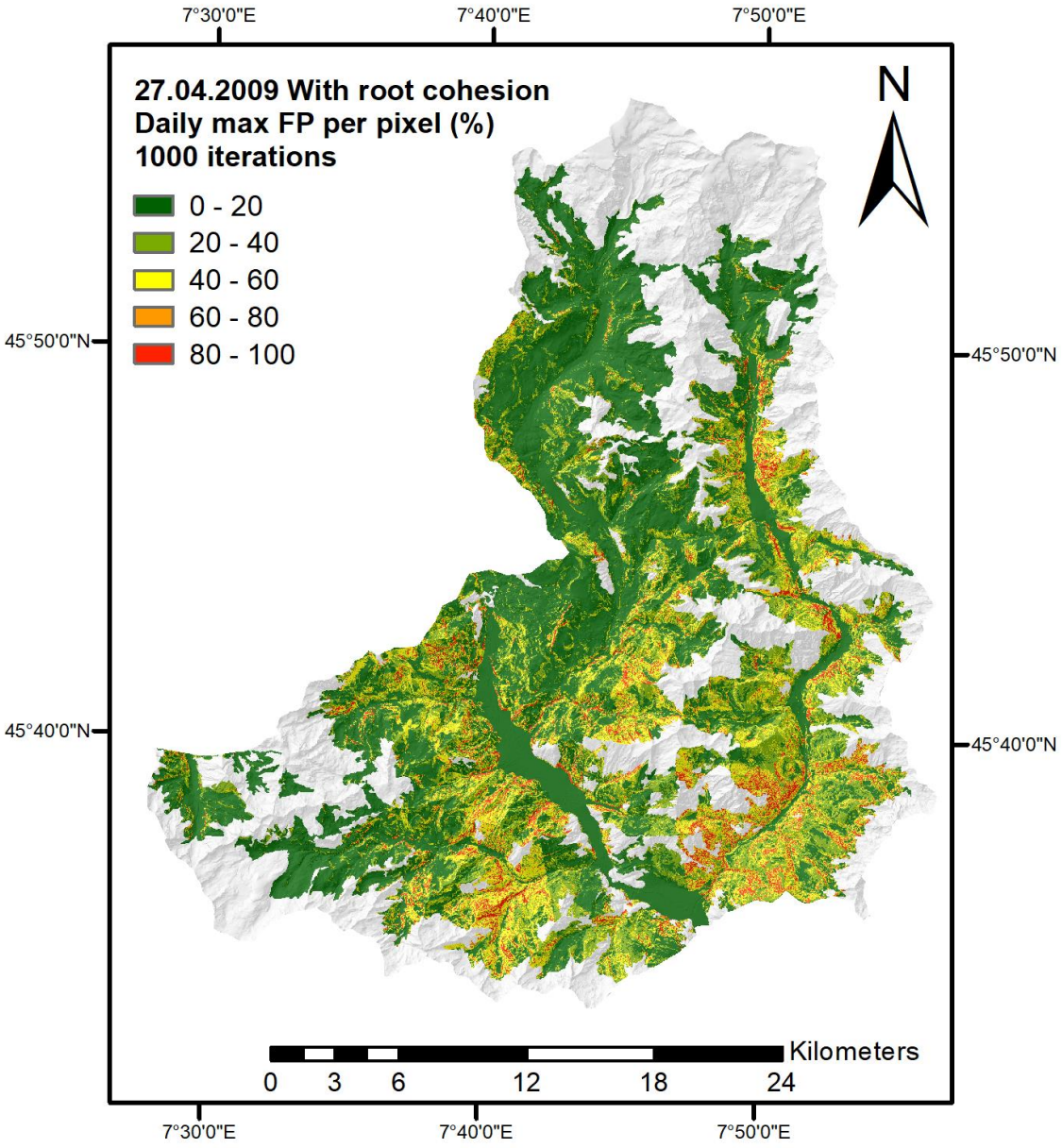

Figure 36. Max Failure Probability (FP) computed by the model for each pixel in the rainy day (27.04.2009), simulation with the root cohesion, 1000 Monte Carlo iterations.

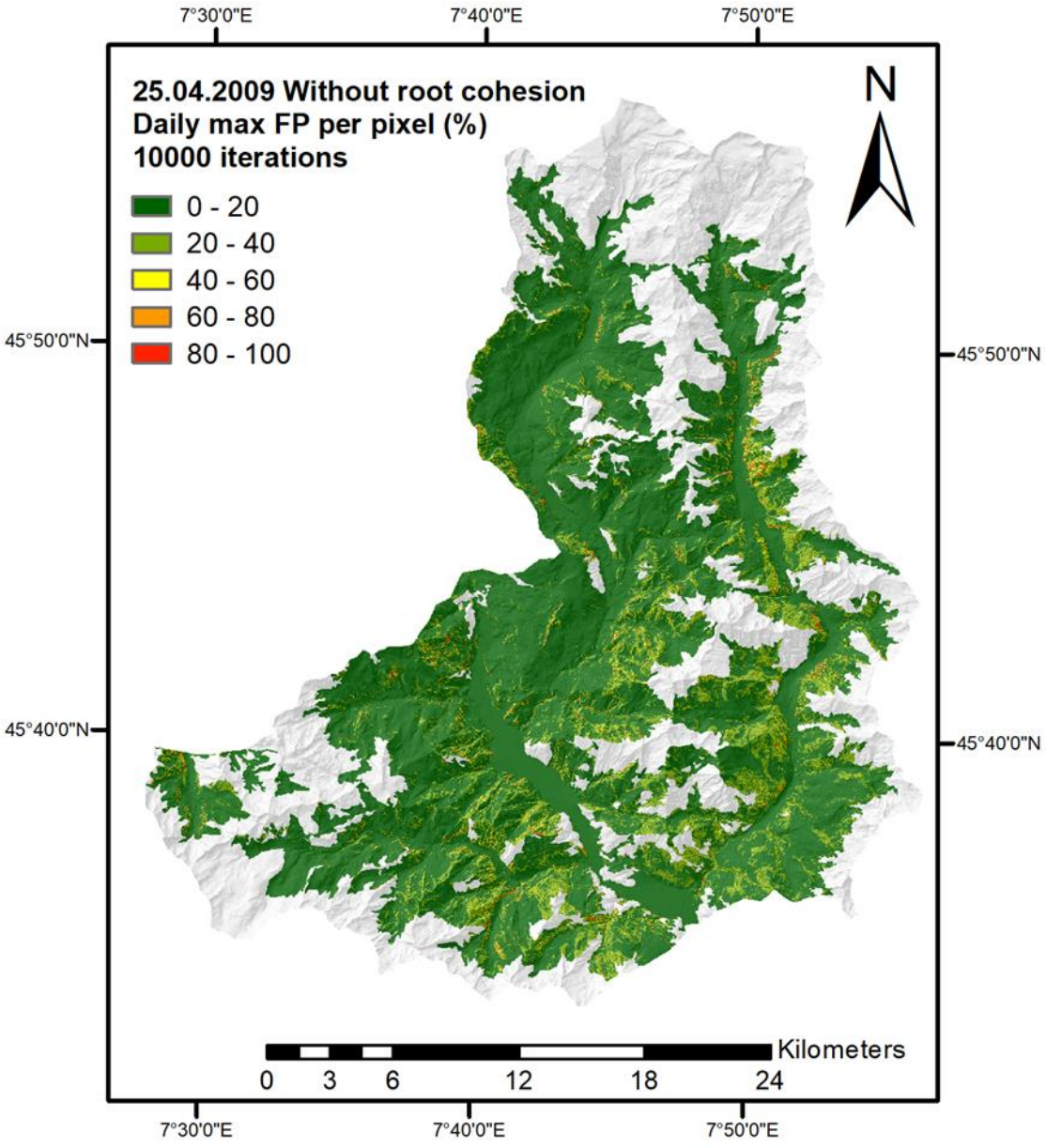

Figure 37. Max Failure Probability (FP) computed by the model for each pixel in the not rainy day (25.04.2009), simulation without the root cohesion, 10000 Monte Carlo iterations.

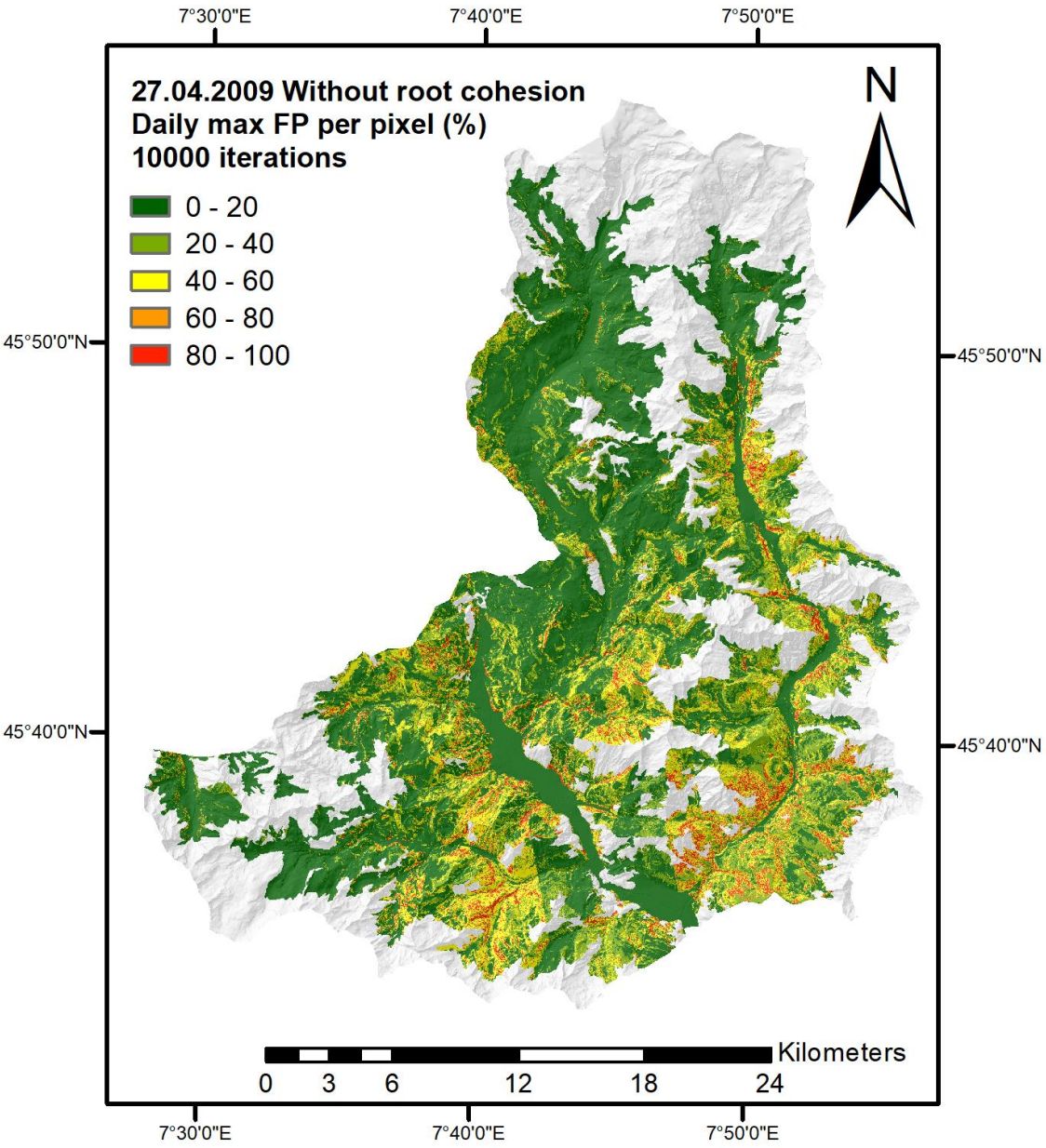

Figure 38. Max Failure Probability (FP) computed by the model for each pixel in the rainy day (27.04.2009), simulation without the root cohesion, 10000 Monte Carlo iterations.

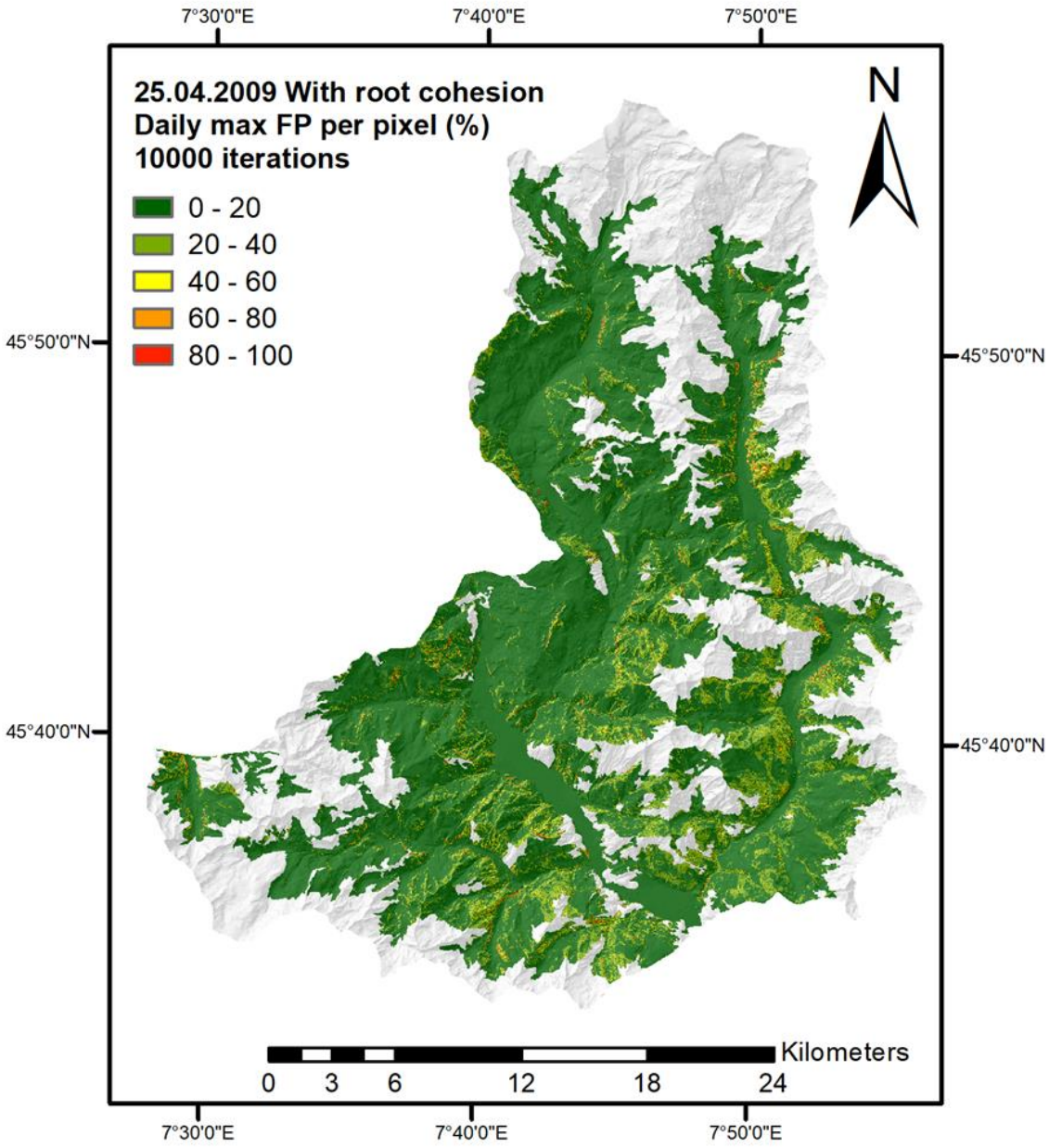

Figure 39. Max Failure Probability (FP) computed by the model for each pixel in the not rainy day (25.04.2009), simulation with the root cohesion, 10000 Monte Carlo iterations.

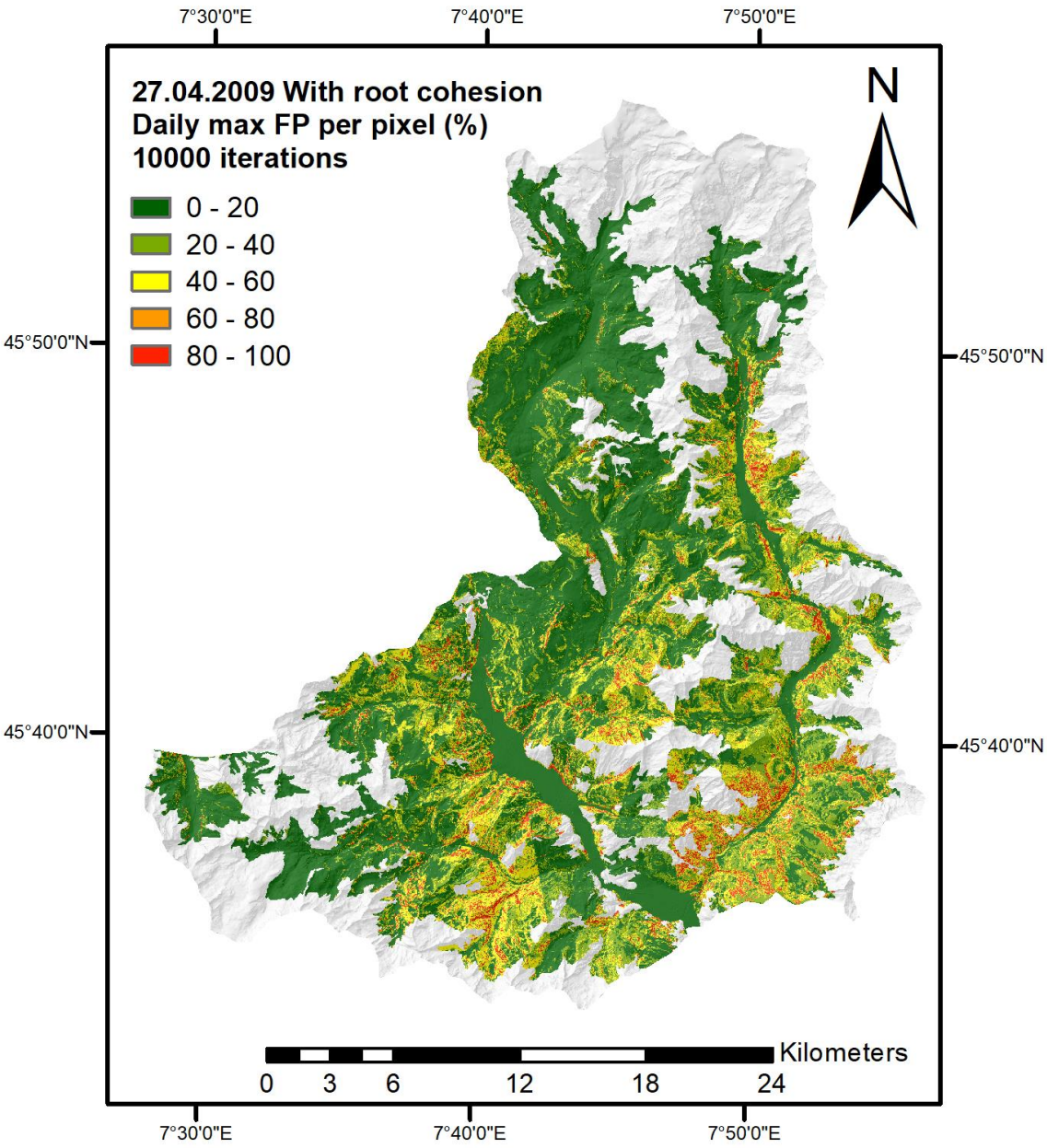

Figure 40. Max Failure Probability (FP) computed by the model for each pixel in the rainy day (27.04.2009), simulation with the root cohesion, 10000 Monte Carlo iterations.

As it can be seen, the difference that we can visually detect among the reported raster maps is the increase of the pixels with higher failure probabilities from the "no rainy" (25.04.2009) to the rainy day (27.04.2009), while the differences between the simulations with or without the root cohesion and between the simulations with 1000 or 10000 iterations are hardly noticeable.

The figures from 41 to 44 represent the difference of max daily failure probability for each pixel of the area between the simulations without and with the root cohesion in the two selected days 25th and 27th April and for the two cases of the 1000/10000 iterations.

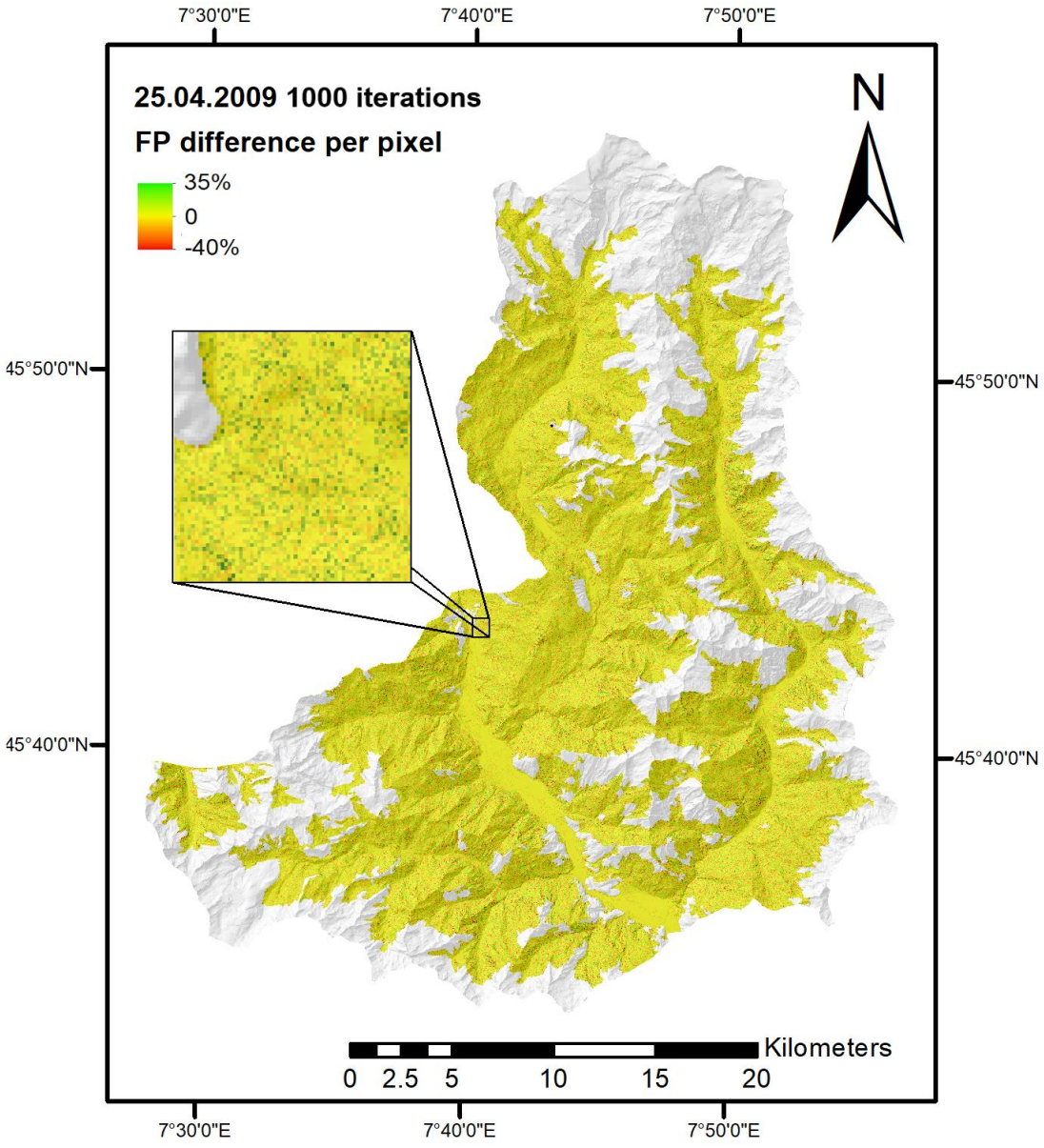

Figure 41. Max Failure Probability (FP) difference for each pixel between the simulation without the root cohesion and the simulation with the root cohesion (max FP of the simulation without the root cohesion minus max FP of the simulation with the root cohesion) for the not rainy day (25.04.2009), 1000 Monte Carlo iterations.

Comparing the two maps of the differences (Figure 41 and Figure 42) we can notice a predominance of the pixels in the spectrum of the yellow, indicating globally a prevalence of low differences in the percentage of the failure probability of the pixels belonging to the simulations with or without the root cohesion, for both days.

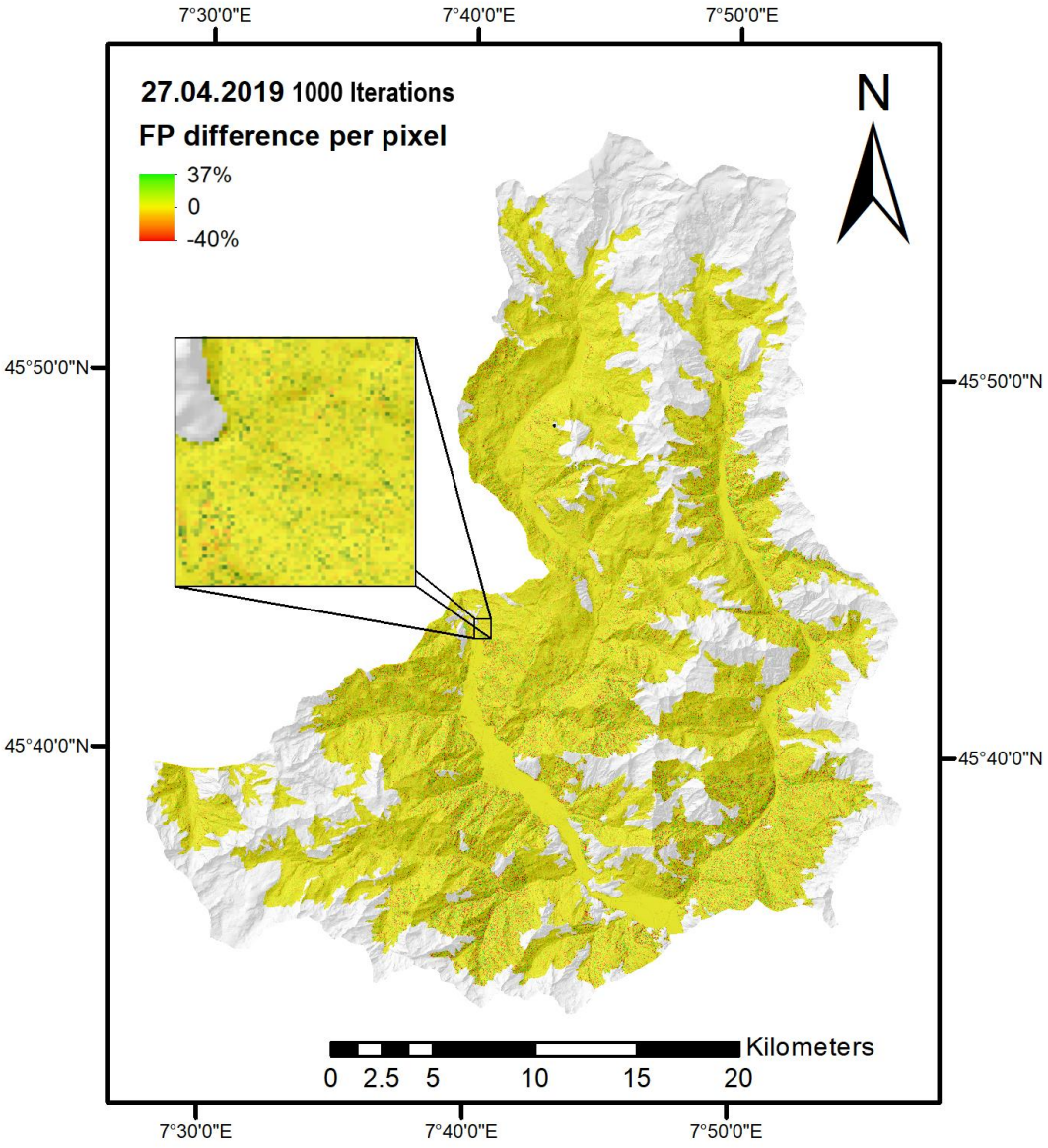

Figure 42. Max Failure Probability (FP) difference for each pixel between the simulation without the root cohesion and the simulation with the root cohesion (max FP of the simulation without the root cohesion minus max FP of the simulation with the root cohesion) for the rainy day (27.04.2009), 1000 Monte Carlo iterations.

Furthermore, when the pixels deviate from the yellow, we cannot notice a marked tendency towards the red (indicating a higher failure probability in the simulation with the root cohesion) nor the green (indicating a higher failure probability in the simulation without the root cohesion).

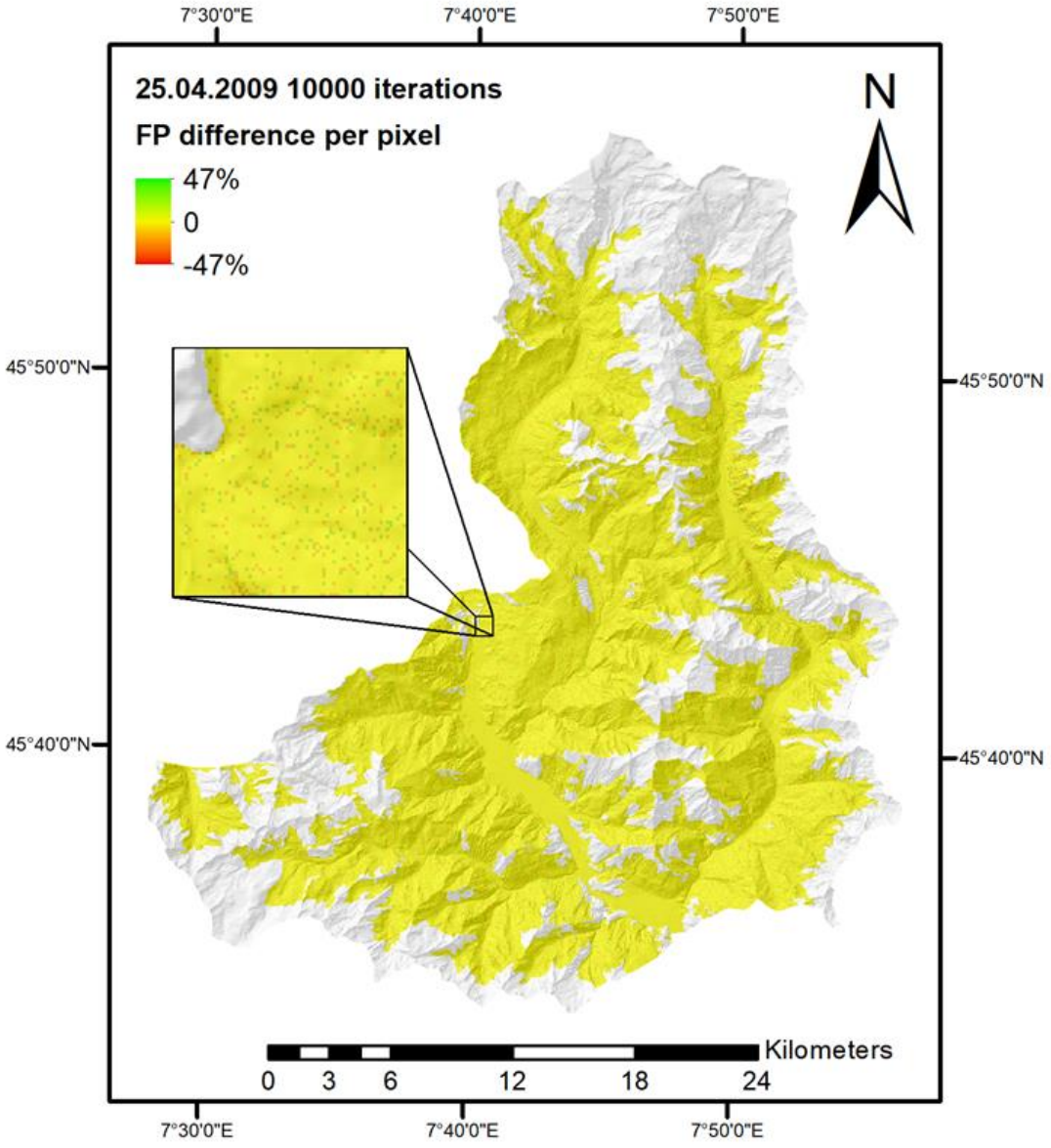

Figure 43. Max Failure Probability (FP) difference for each pixel between the simulation without the root cohesion and the simulation with the root cohesion (max FP of the simulation without the root cohesion minus max FP of the simulation with the root cohesion) for the not rainy day (25.04.2009), 10000 Monte Carlo iterations.

In the case of the simulations with 10000 iterations (Figure 43, Figure 44), we can notice the same behaviour of the previous maps (1000 iterations), with an even more marked predominance of the yellow, besides to a not clear tendency neither towards the red nor the green also in this case.

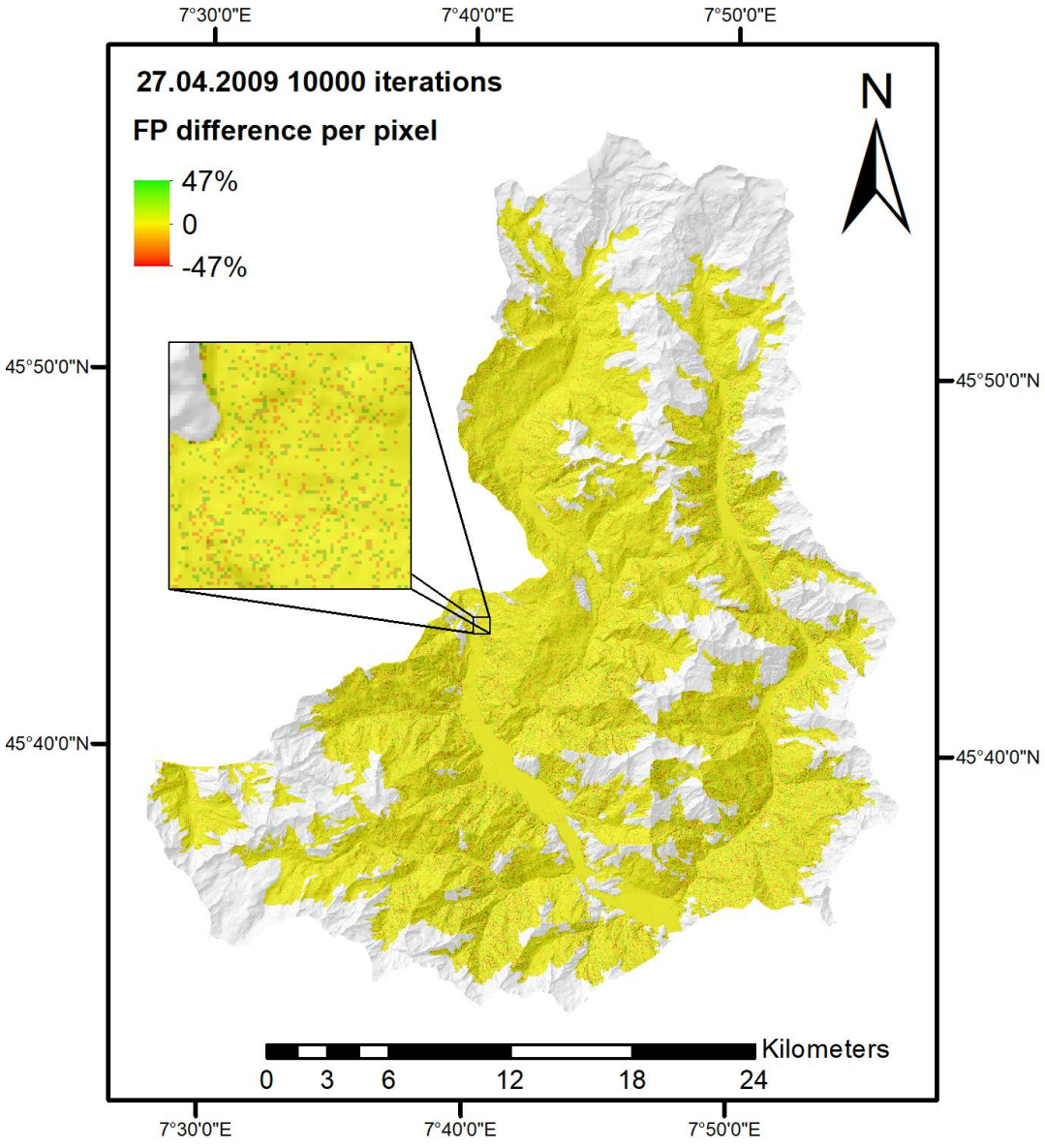

Figure 44. Max Failure Probability (FP) difference for each pixel between the simulation without the root cohesion and the simulation with the root cohesion (max FP of the simulation without the root cohesion minus max FP of the simulation with the root cohesion) for the not rainy day (27.04.2009), 10000 Monte Carlo iterations.

The figures from Figure 45 to Figure 48 represent the previous four maps in the form of mean differences at the basin level (within each basin, the mean of the values representing the difference of failure probability between the pixels of the simulations with or without the root cohesion was calculated).

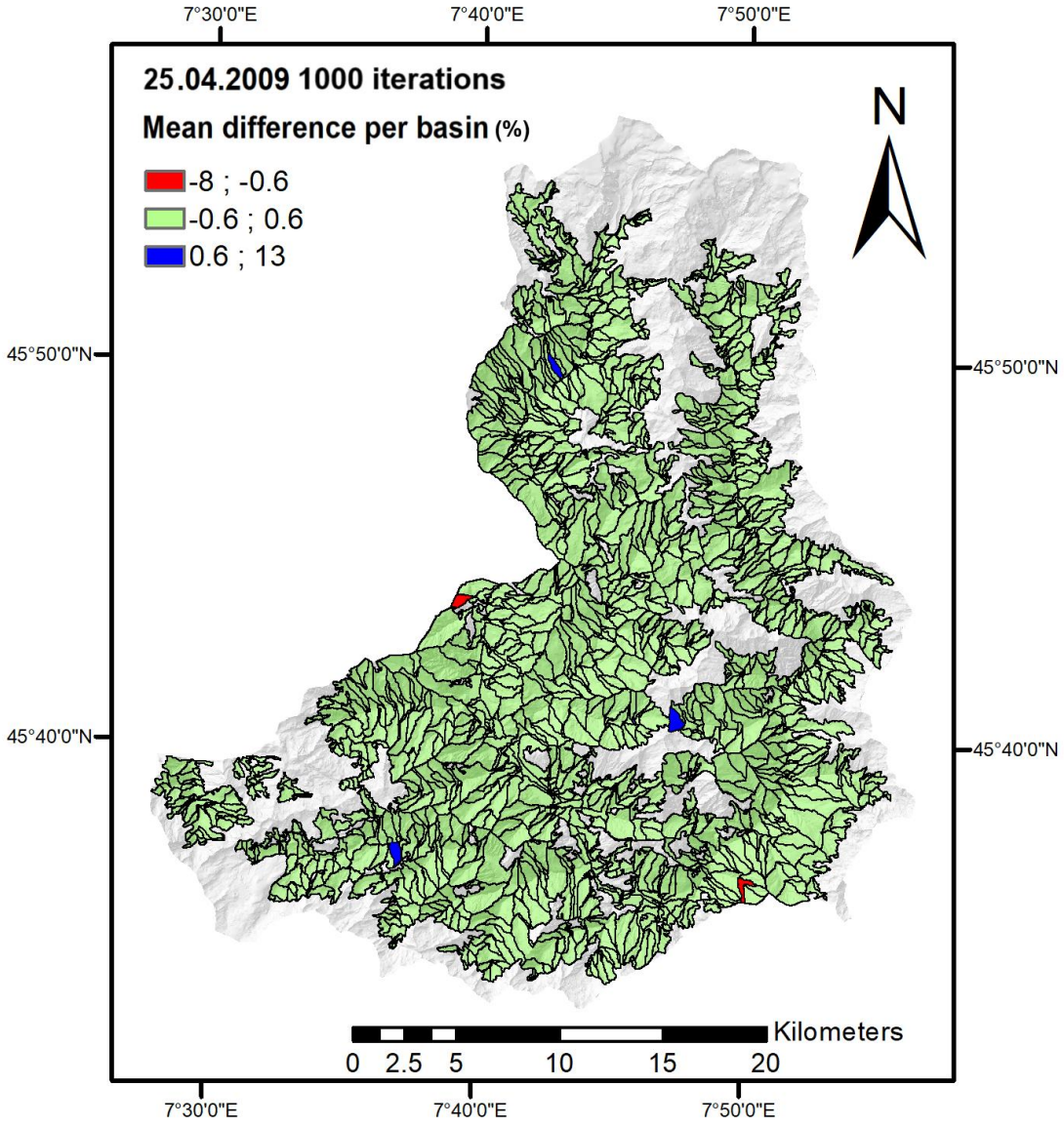

Figure 45. Mean Failure Probability (FP) difference between the two simulations (mean of the difference max FP of the simulation without the root cohesion minus max FP of the simulation with the root cohesion) at the basin level in the not rainy day (25.04.2009), 1000 Monte Carlo iterations.

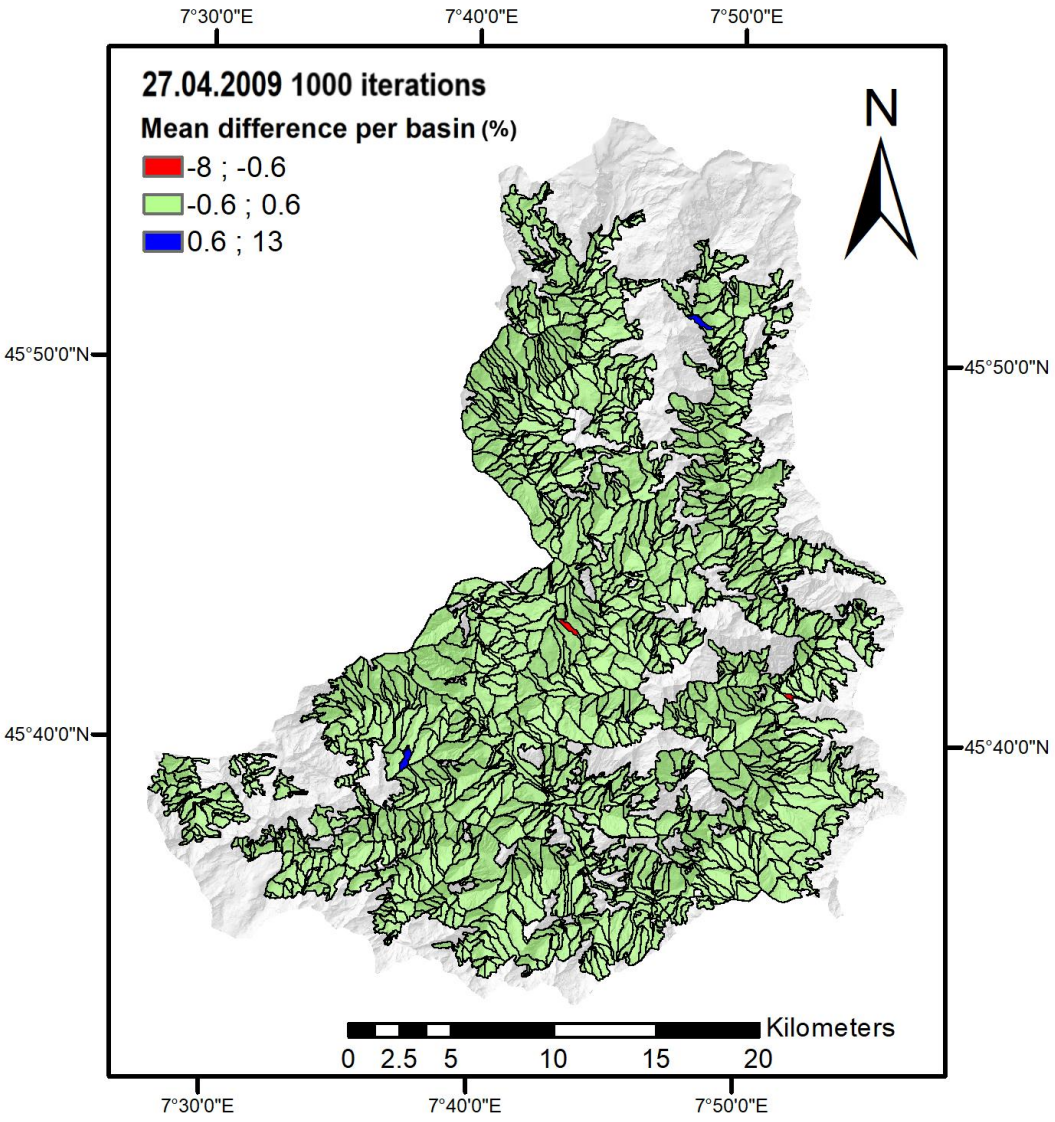

Figure 46. Mean Failure Probability (FP) difference between the two simulations (mean of the difference max FP of the simulation without the root cohesion minus max FP of the simulation with the root cohesion) at the basin level in the rainy day (27.04.2009), 1000 Monte Carlo iterations.

As shown in the maps (Figure 45 and Figure 46), the mean difference per basin varies between -8 % and 13 %, but only in sporadic cases the basins reach these values, almost the totality of the basins shows a value close to zero (falling into the range -0.6 %, 0.6%).

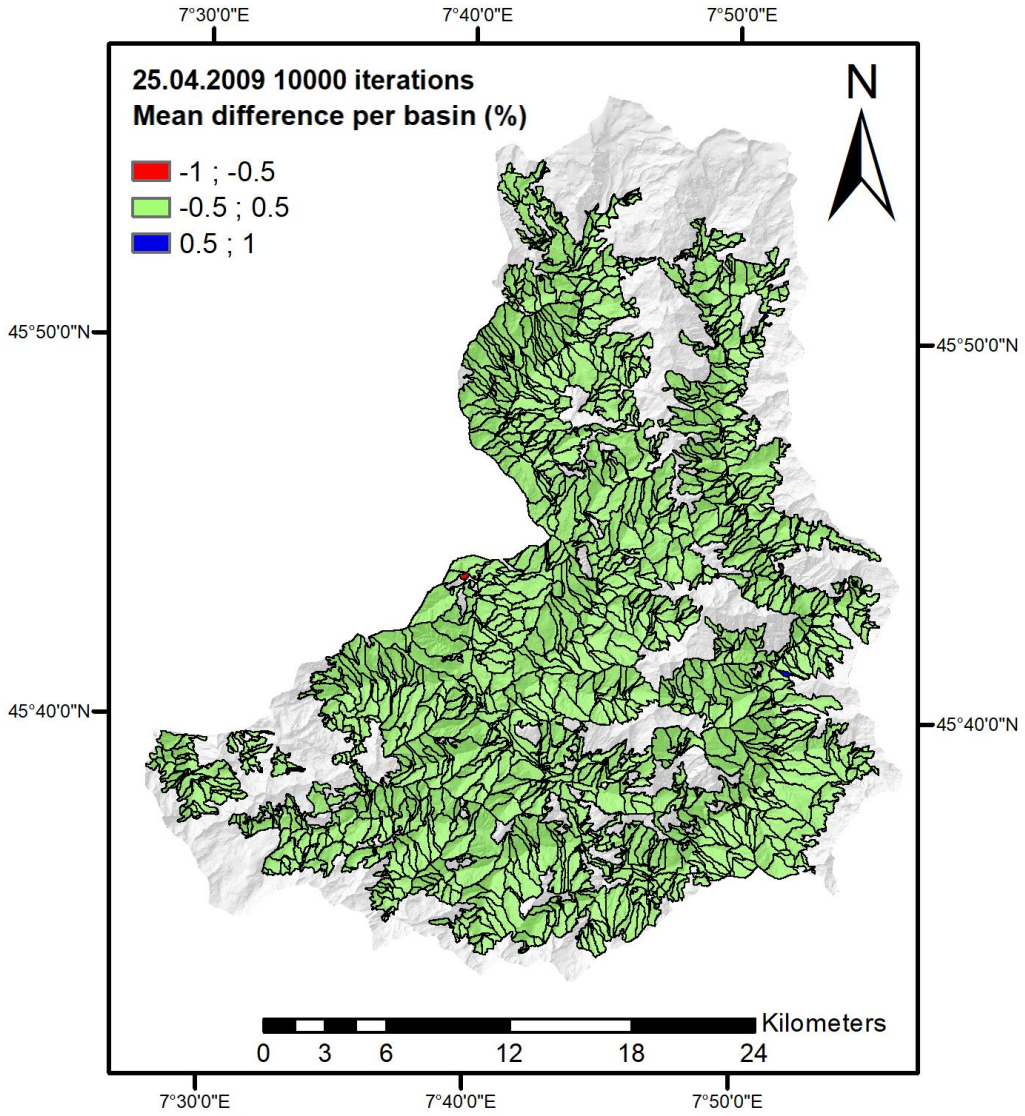

Figure 47. Mean Failure Probability (FP) difference between the two simulations (mean of the difference max FP of the simulation without the root cohesion minus max FP of the simulation with the root cohesion) at the basin level in the not rainy day (25.04.2009), 10000 Monte Carlo iterations.

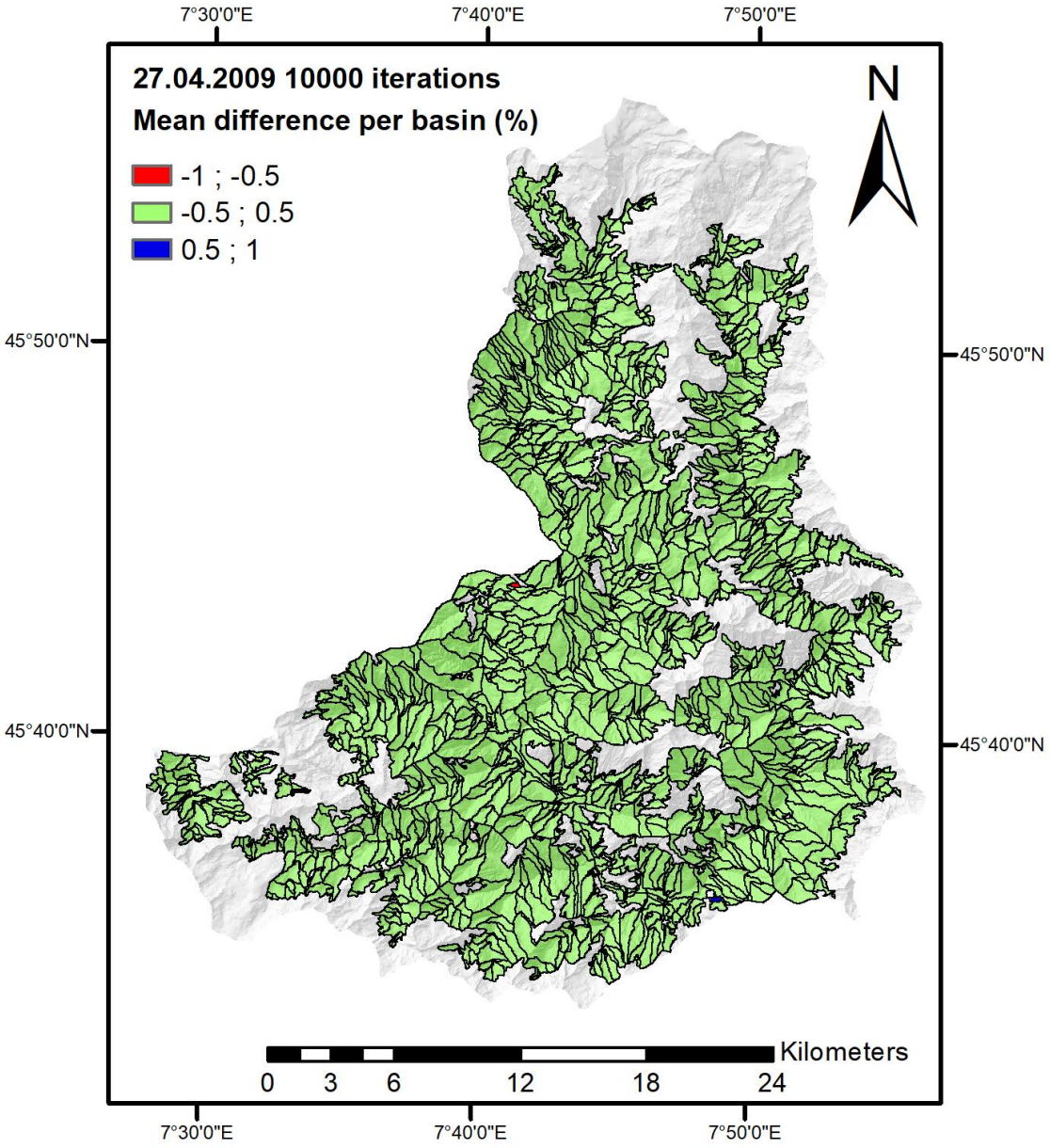

Figure 48. Mean Failure Probability (FP) difference between the two simulations (mean of the difference max FP of the simulation without the root cohesion minus max FP of the simulation with the root cohesion) at the basin level in the rainy day (27.04.2009), 10000 Monte Carlo iterations.

The maps of the mean failure probability difference per basin of the 10000 iterations-simulations show a smaller range of variation (-1 %, 1%), and the totality of the basins has a mean value around zero (falling into the range -0.5%-0.5%) also in these cases.

9.1.2 Cervinara case study

For the Cervinara case study, the 14th December 1999 was selected as "no rainy" day and the 16th December was chosen as rainy day.

The figures from Figure 49 Figure 52 represent the distribution of the daily max failure probability computed by the model in the two selected days during the simulations with or without the root cohesion.

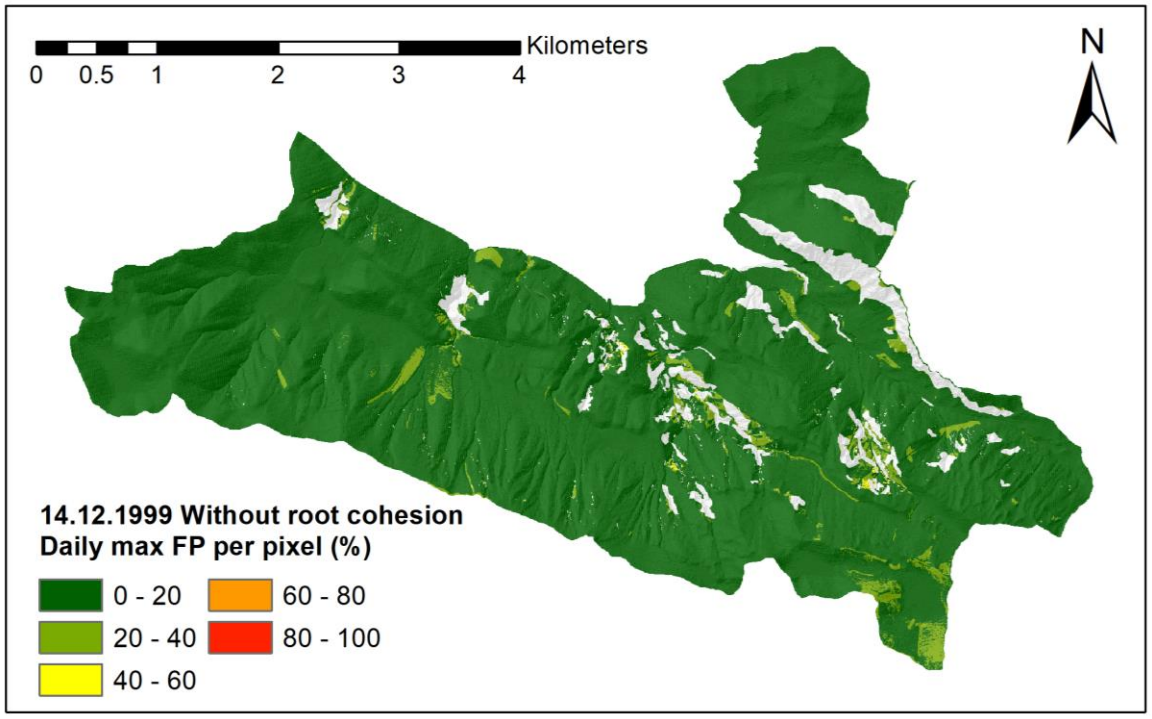

Figure 49. Max Failure Probability (FP) calculated by the model for each pixel in the not rainy day (14.12.1999), simulation without the root cohesion, 1000 Monte Carlo iterations.

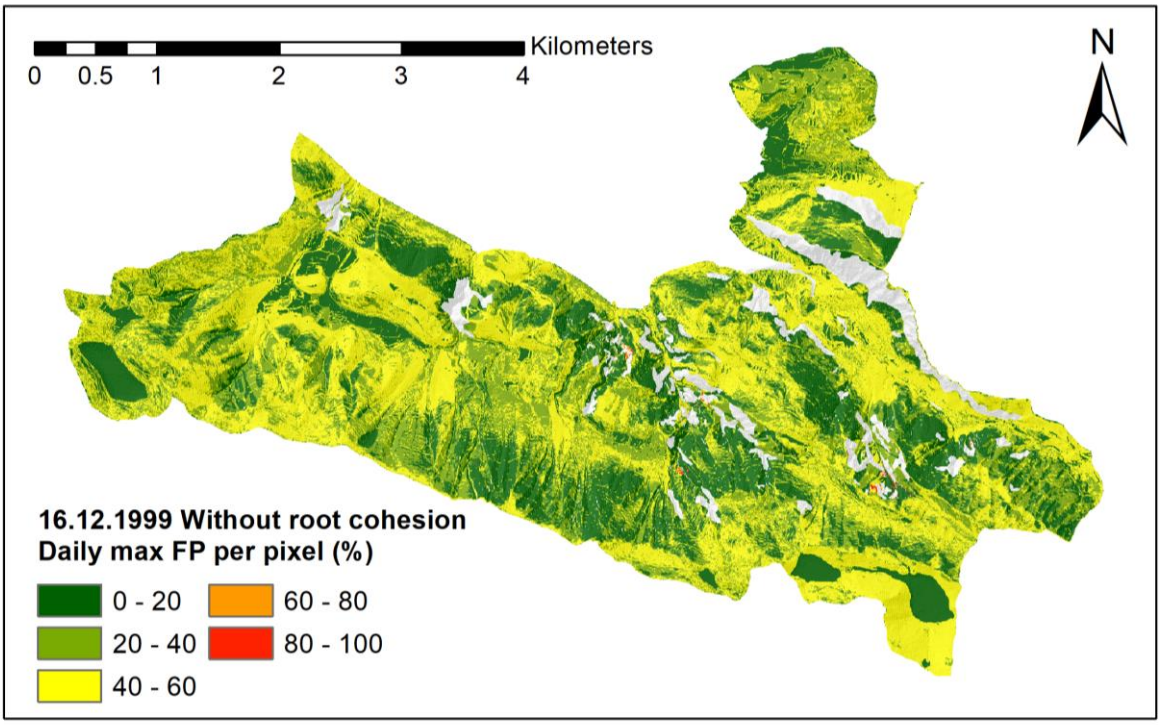

Figure 50. Max Failure Probability (FP) computed by the model for each pixel in the rainy day (16.12.1999), simulation without the root cohesion, 1000 Monte Carlo iterations.

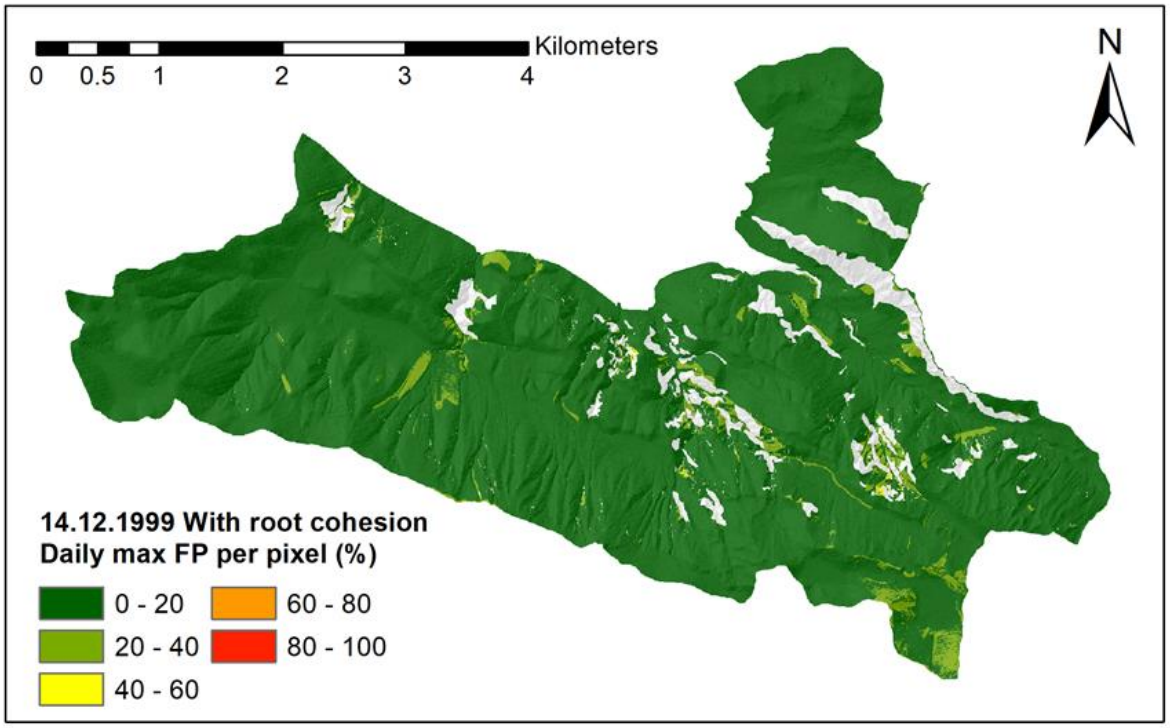

Figure 51. Max Failure Probability (FP) computed by the model for each pixel in the not rainy day (14.12.1999), simulation with the root cohesion, 1000 Monte Carlo iterations.

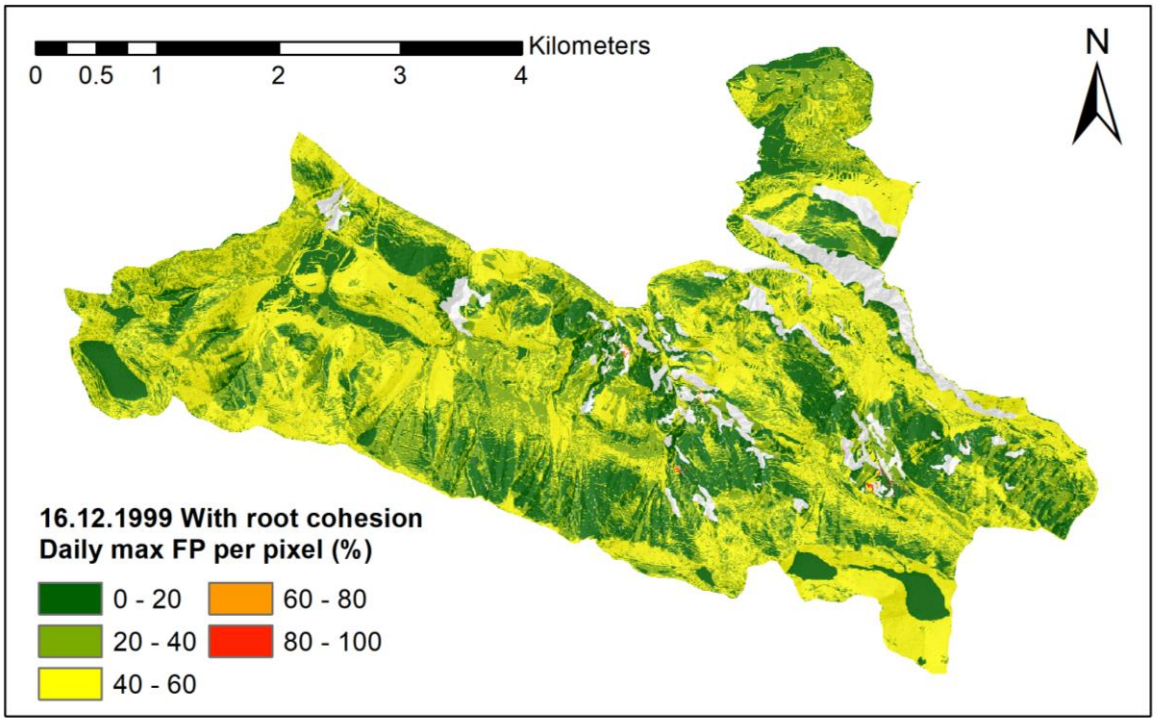

Figure 52. Max Failure Probability (FP) computed by the model for each pixel in the rainy day (16.12.1999), simulation with the root cohesion, 1000 Monte Carlo iterations.

Besides to appreciate the massive change in the failure probabilities of the area from the 14th to the 16th, even in this case study, like in the previous one (Valle d'Aosta), the differences between the simulations with or without the root cohesion are hardly noticeable.

The Figure 53 and Figure 54 show the difference in the max failure probability for each pixel of the area between the simulation without the root cohesion and the simulation with the root cohesion, in the two days 14th and 16th December. Figure 55 and Figure 56 represent the mean FP difference at the basin level.

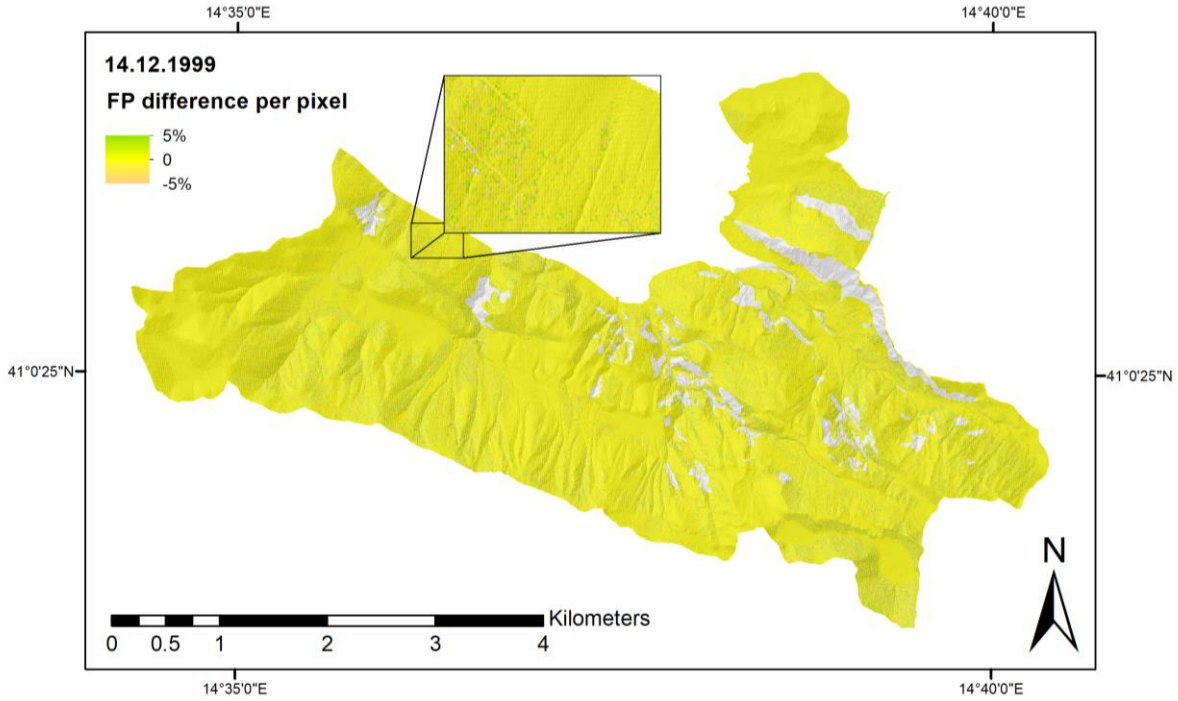

Figure 53. Max Failure Probability (FP) difference for each pixel between the simulation without the root cohesion and the simulation with the root cohesion (max FP of the simulation without the root cohesion minus max FP of the simulation with the root cohesion) for the not rainy day (14.12.1999), 1000 Monte Carlo iterations.

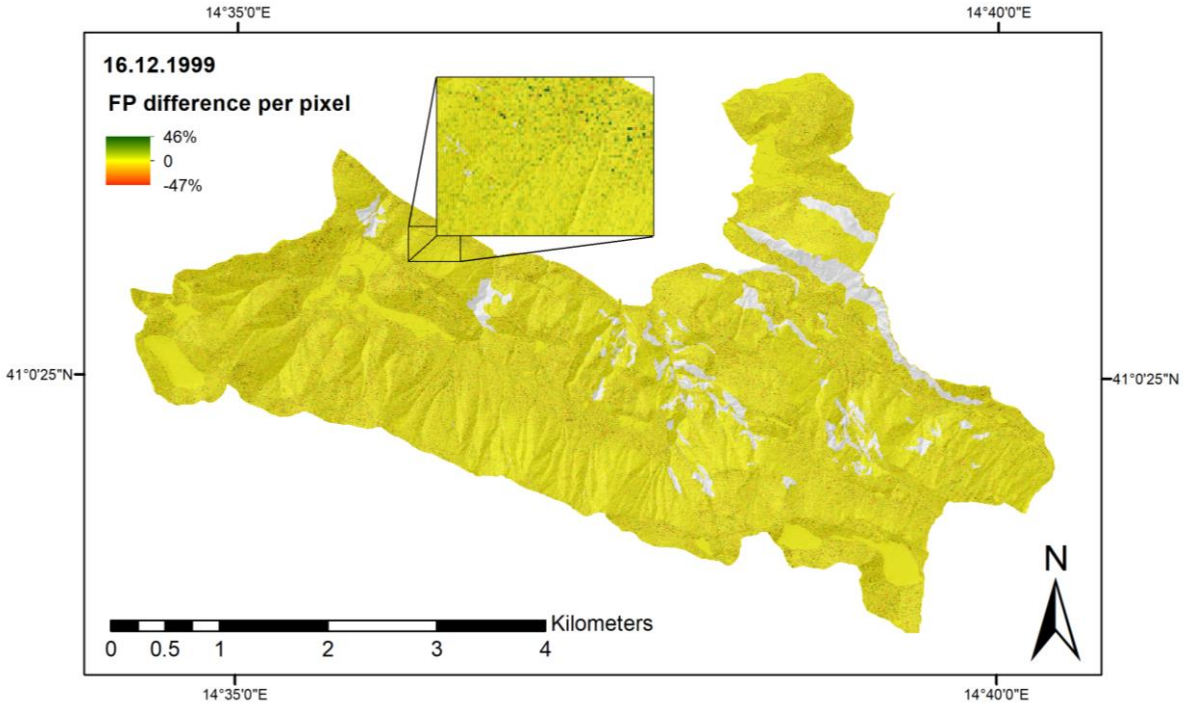

Figure 54. Max Failure Probability (FP) difference for each pixel between the simulation without the root cohesion and the simulation with the root cohesion (max FP of the simulation without the root cohesion minus max FP of the simulation with the root cohesion) for the rainy day (16.12.1999), 1000 Monte Carlo iterations.

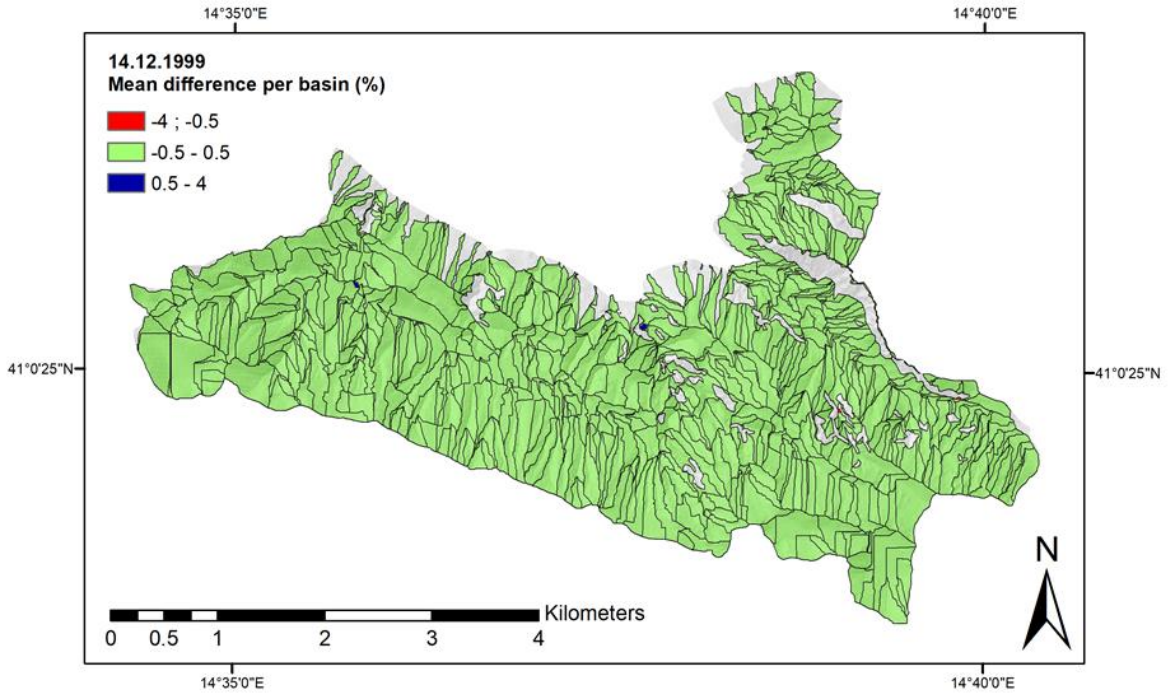

Figure 55. Mean Failure Probability (FP) difference between the two simulations (mean of the difference max FP of the simulation without the root cohesion minus max FP of the simulation with the root cohesion) at the basin level in the not rainy day (14.12.1999), 1000 Monte Carlo iterations.

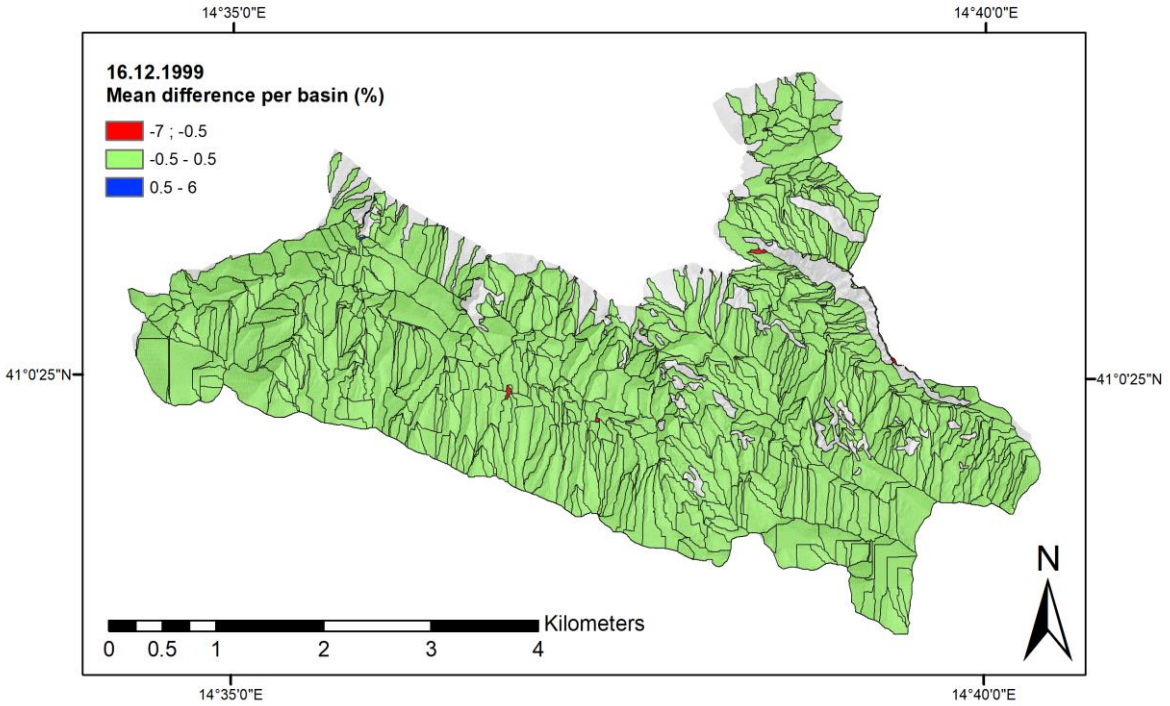

Figure 56. Mean Failure Probability (FP) difference between the two simulations (mean of the difference max FP of the simulation without the root cohesion minus max FP of the simulation with the root cohesion) at the basin level in the rainy day (16.12.1999), 1000 Monte Carlo iterations.

Examining the FP difference maps (Figure 53 and Figure 54), the one representing the 16th December has a very different range of variation (46%, -47%) and a higher amount of the pixels with values deviating from the zero if compared to the one representing the 14th December, which has a range of (-5%, 5%) and a more dominating presence of pixels close to zero (coloured in the spectre of the yellow). Nevertheless, when the maps are elaborated to have the mean value of the differences within the basins, for both cases, the almost totality of the basins show a mean value between -0.5 % and 0.5 %.

By means of this approach of analysis of the results and dealing with failure probabilities (not with factors of safety), we cannot detect notable differences on average at the basin level between the results of the simulations with or without the root cohesion both for the Valle d'Aosta and the Cervinara case study.

9.2 Unstable pixels trend (whole period)

The second approach to analyse the effect of the root cohesion on the results of the simulations consisted in the examination of the trend of the unstable pixels difference (count of unstable pixels of the simulation without root cohesion minus the count of the simulation with root cohesion, the unstable have a daily max failure probability higher than 75 %) during the whole period, to compare day by day the two simulations.

These analyses were performed on the Valle d'Aosta 2009 event-1000 iterations; the Valle d'Aosta 2009 event-10000 iterations; the Valle d'Aosta 2010 event; the Cervinara event. In addiction, to better explore the root cohesion effect, the results of the Valle d'Aosta 2010 event were elaborated to analyse the difference trend in subareas with peculiar characteristics.

Therefore, the unstable pixels difference trend analysis was carried out on the following 8 cases:

- Valle d'Aosta 2009 event (1000 iterations), whole area;
- Valle d'Aosta 2009 event (10000 iterations), whole area;
- Valle d'Aosta 2010 event (1000 iterations), whole area;
- Valle d'Aosta 2010 event (1000 iterations), subarea with same lithology (therefore under the same geotechnical parameters values);
- Valle d'Aosta 2010 event (1000 iterations), subarea with same root cohesion equal to 19 kPa;
- Valle d'Aosta 2010 event (1000 iterations), subarea with same lithology and root cohesion value (12.5 kPa);

– Valle d'Aosta 2010 event (1000 iterations), subarea with the root cohesion higher than 10 kPa;
– Cervinara event (1000 iterations), the whole area.

9.2.1 Valle d'Aosta case study

The figures from Figure 59Figure 58 show the trend for the 7 cases regarding the Valle d'Aosta study area. The difference between the simulation without the root cohesion and the simulation with the root cohesion was presented in the graphs (the red line) accompanied by the daily rainfall (the blue bars).

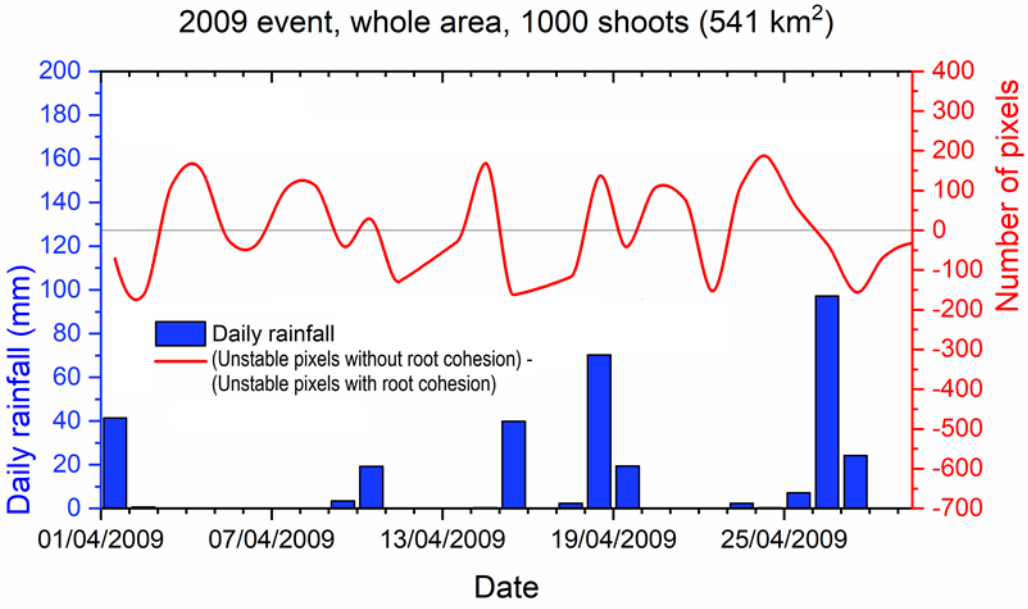

Figure 57. Comparison of the unstable pixels (failure probability > 75%) trend (count of the daily unstable pixels during the period) of the two simulations with and without the root cohesion (1000 Monte Carlo iterations). The red line represents the difference: without root cohesion-simulation unstable pixels minus with root cohesion-simulation unstable pixels, for every day of the period 02.04.2009-30.04.2009 in the whole study area. The blue bars represent the daily rainfall (mean value of the rainfall data recorded by all the rain gauges of the area.

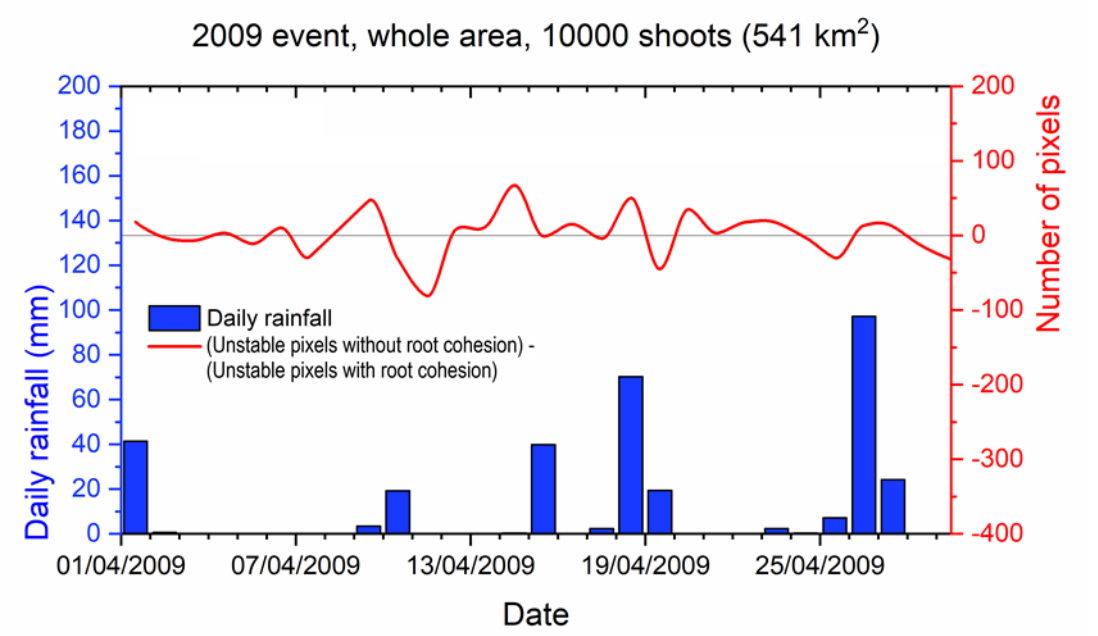

Figure 58. Comparison of the unstable pixels (failure probability > 75%) trend (count of the daily unstable pixels during the period) of the two simulations with and without the root cohesion (10000 Monte Carlo iterations). The red line represents the difference: without root cohesion-simulation unstable pixels minus with root cohesion-simulation unstable pixels, for every day of the period 02.04.2009-30.04.2009 in the whole study area. The blue bars represent the daily rainfall (mean value of the rainfall data recorded by all the rain gauges of the area.

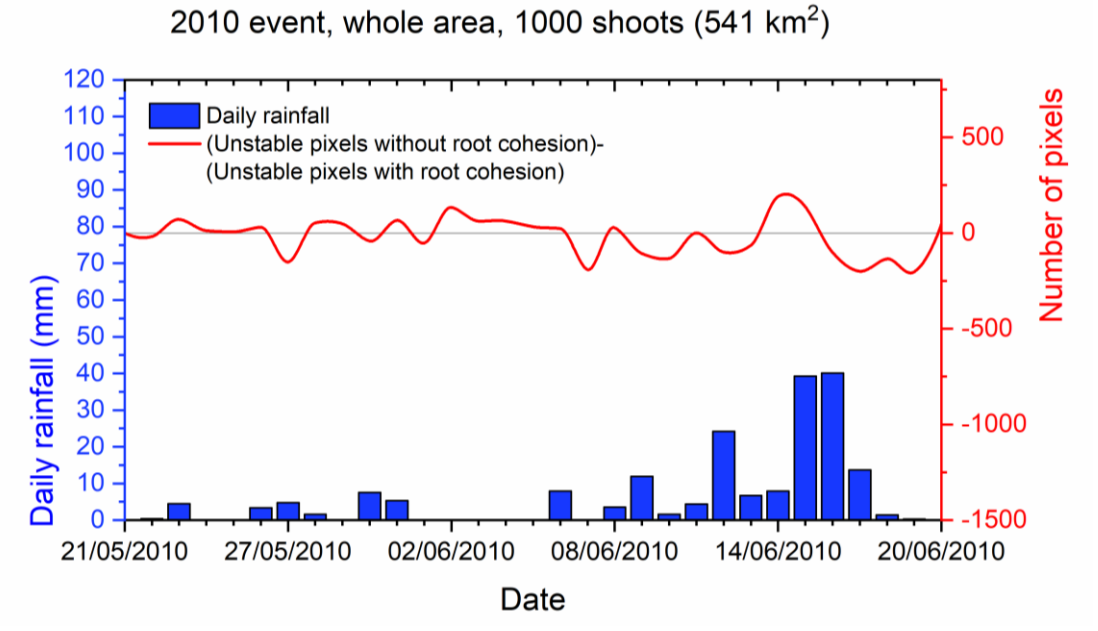

Figure 59. Comparison of the unstable pixels (failure probability > 75%) trend (count of the daily unstable pixels during the period) of the two simulations with and without the root cohesion (1000 Monte Carlo iterations). The red line represents the difference: without root cohesion-simulation unstable pixels minus with root cohesion-simulation unstable pixels, for every day of the period 21.05.2010-20.06.2010 in the whole study area. The blue bars represent the daily rainfall (mean value of the rainfall data recorded by all the rain gauges of the area).

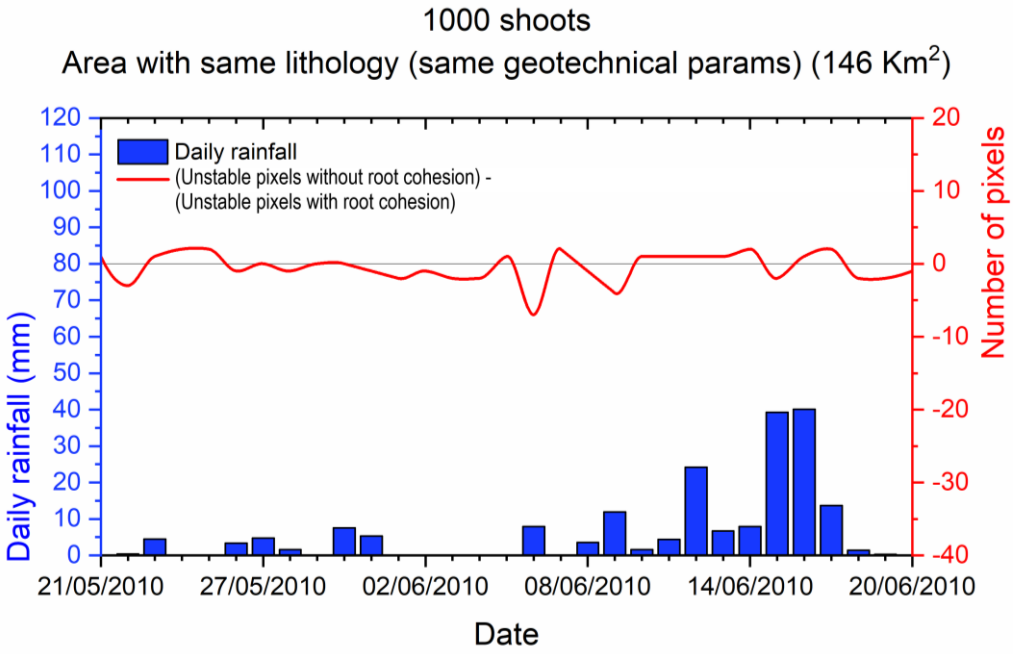

Figure 60. Comparison of the unstable pixels (failure probability > 75%) trend (count of the daily unstable pixels during the period) of the two simulations with and without the root cohesion (1000 Monte Carlo iterations). The red line represents the difference: without root cohesion-simulation unstable pixels minus with root cohesion-simulation unstable pixels, for every day of the period 21.05.2010-20.06.2010 in a subarea with same geotechnical parameter values. The blue bars represent the daily rainfall (mean value of the rainfall data recorded by all the rain gauges of the area).

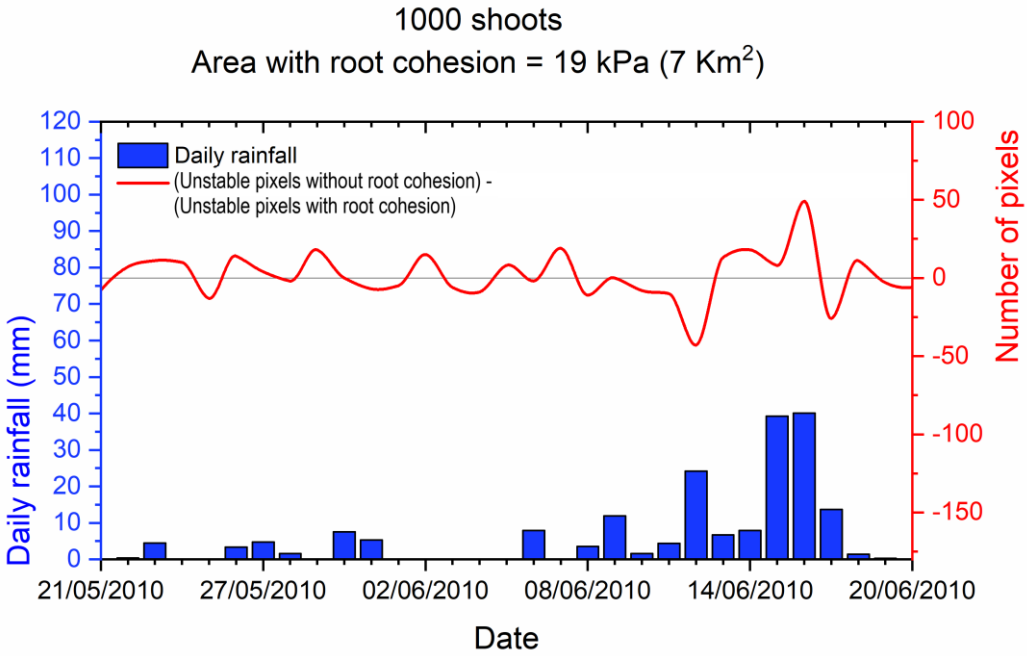

Figure 61. Comparison of the unstable pixels (failure probability > 75%) trend (count of the daily unstable pixels during the period) of the two simulations with and without the root cohesion (1000 Monte Carlo iterations). The red line represents the difference: without root cohesion-simulation unstable pixels minus with root cohesion-simulation unstable pixels, for every day of the period 21.05.2010-20.06.2010 in a subarea with a unique value of root cohesion (19 kPa). The blue bars represent the daily rainfall (mean value of the rainfall data recorded by all the rain gauges of the area).

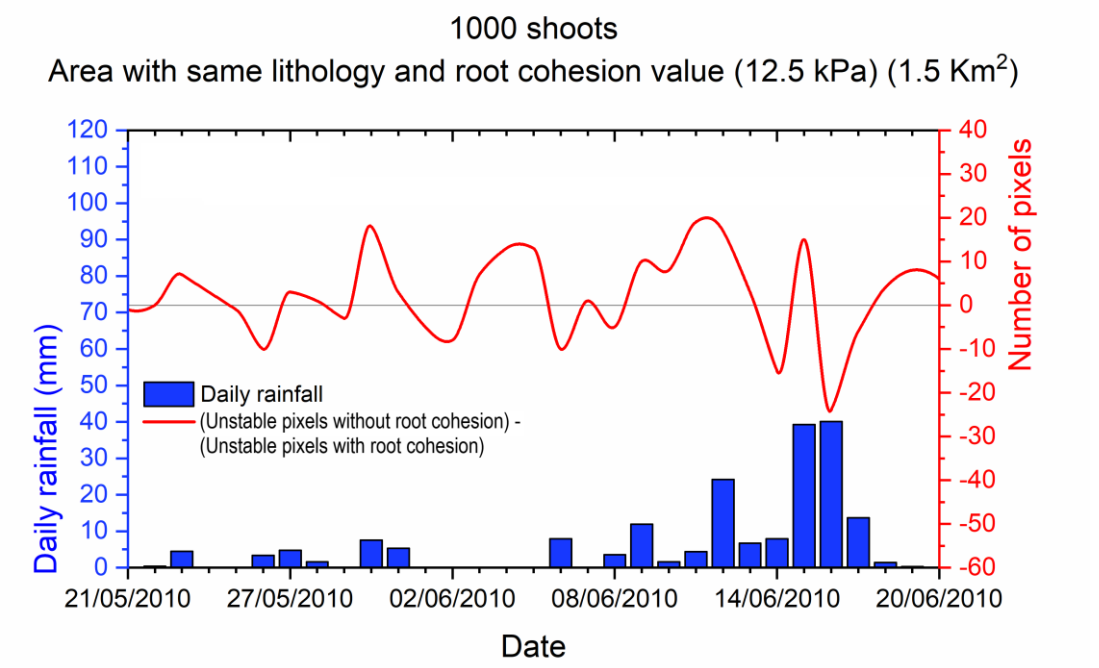

Figure 62. Comparison of the unstable pixels (failure probability > 75%) trend (count of the daily unstable pixels during the period) of the two simulations with and without the root cohesion (1000 Monte Carlo iterations). The red line represents the difference: without root cohesion-simulation unstable pixels minus with root cohesion-simulation unstable pixels, for every day of the period 21.05.2010-20.06.2010 in a subarea of same lithology (therefore same geotechnical parameters values) and root cohesion value (2.5 kPa). The blue bars represent the daily rainfall (mean value of the rainfall data recorded by all the rain gauges of the area).

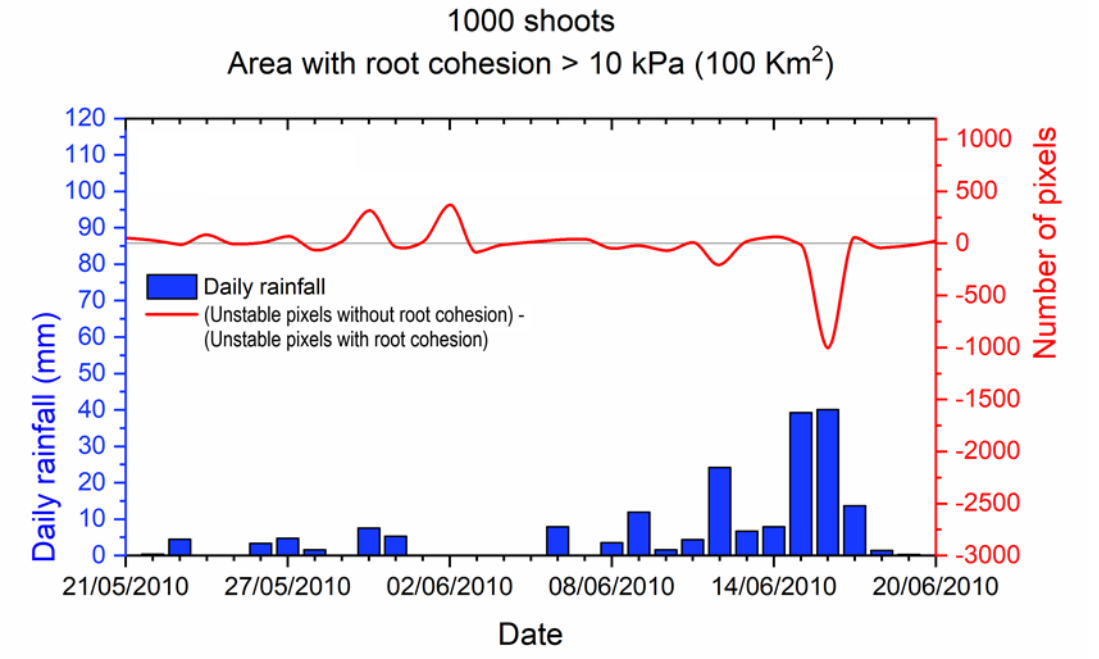

Figure 63. Comparison of the unstable pixels (failure probability > 75%) trend (count of the daily unstable pixels during the period) of the two simulations with and without the root cohesion (1000 Monte Carlo iterations). The red line represents the difference: without root cohesion-simulation unstable pixels minus with root cohesion-simulation unstable pixels, for every day of the period 21.05.2010-20.06.2010 in a subarea with root cohesion higher than 10 kPa. The blue bars represent the daily rainfall (mean value of the rainfall data recorded by all the rain gauges of the area).

As it can be seen in the graphs, the difference for the whole area in three different simulations (Figure 57, Figure 58, Figure 59) has a trend that moves in a balanced way above and below the zero (for every day in which the red line is below the zero, the reference grey line, the model found more unstable pixels in the simulation with the root cohesion). From the comparison of the trend with the rainfall pattern, it is not possible to individuate particular correlations helping in the interpretation of the difference trend. Regarding the analysis on the subareas (figure from Figure 60 Figure 63), in the two cases in which an area with a same medium-high root cohesion value was considered (Figure 62 and Figure 63), the difference assumes a positive value for a number of days higher than negatives. From an analysis on the unstable pixels number of the two simulations in these subareas (same root cohesion of 19 kPa; same lithology and root cohesion of 12.5 kPa) results that there were 126 and 481 (respectively) more unstable pixels in the simulation without the root cohesion, not negligible amount of pixels considering the limited extension of the areas (7 km^2 and 1.5 km^2).

These findings suggest that the root cohesion moves the results of the simulations towards higher stability, but its effect is not clearly detectable when we consider the whole area. Furthermore, up to this point, we have discussed the results only referring to a failure probability higher than the 75%, the examination of the difference trend considering other thresholds can give more indications, and this is the rationale of the third analysis approach described in Section 9.3.

9.2.2 Cervinara case study

In the Cervinara case study, the count of unstable pixels (max FP > 75 %) per day of the simulations with or without the root cohesion has an equivalent trend in the two cases. Therefore, we prefer to present the data in the form of a table instead of the graphs presented for the Valle d'Aosta case study. Indeed, as shown in Table 6, in terms of count of unstable pixels there is no difference except for one day out of three (16.12.1999) consisting in only one pixel: 463 unstable pixels in the simulation without the root cohesion, 462 in the simulation with the root cohesion.

	Without root cohesion	**With root cohesion**
14.12.1999	0	0
15.12.1999	175	175
16.12.1999	463	462
17.12.1999	171	171

Table 6. Unstable pixels trend for the simulations with or without the root cohesion. Count of the pixels with a daily max FP > 75 % for each day of the event in the two cases (with or without the root cohesion).

9.3 Failure probability trend (rainy and not rainy days)

The third approach to analyse the effect of the root cohesion on the results consisted in comparing the number of unstable pixels found by the model for each failure probability value (from 0 to 100%) in the simulations with and without the root cohesion, during rainy and no rainy days and in different subareas with specific features.

9.3.1 Valle d'Aosta case study

For the Valle d'Aosta case study, the analysis was performed on the results of 2009 event – 1000 iterations, regarding three different areas: a) the whole area; b) a subarea with the same value of root cohesion (19 kPa); c) a subarea with same lithology (same values of the geotechnical parameters) and same root cohesion value (12.5 kPa). The selected days are 08.04.2009 as the "no rainy day" (a day without precipitations following days without precipitations), the 27.04.2009 as "first rainy day" (a day with rainfall following days of no rainfall), the 28.04.2009 as "second rainy day" (a day with rainfall following a rainy day).

The data were elaborated to obtain the difference trend between the simulations in terms of unstable pixels in the whole range of failures probabilities for the three areas and the three different days. Furthermore, the total number of pixels with failure probabilities higher than 75% was extracted for each day, simulation and area.

In the "no rainy day" (08.04.2009), the model found more unstable pixels in all the three areas during the simulation without the root cohesion, and the difference (between the count of unstable pixels of the two simulations) is higher in the two subareas with the same medium-high root cohesion (right side of Figure 64, red and light blue boxes).

Regarding the trend of the difference with respect to the failure probabilities, in the whole area, we cannot detect particular discrepancies between the two simulations. Differently in the subareas b) and c), we can observe that the trend moves in a balanced way above and below the zero line in the lower failure probabilities, as the probabilities value increases the trend assumes positives values mainly passed the 30 % in the b) case and the 60% in the c) case.

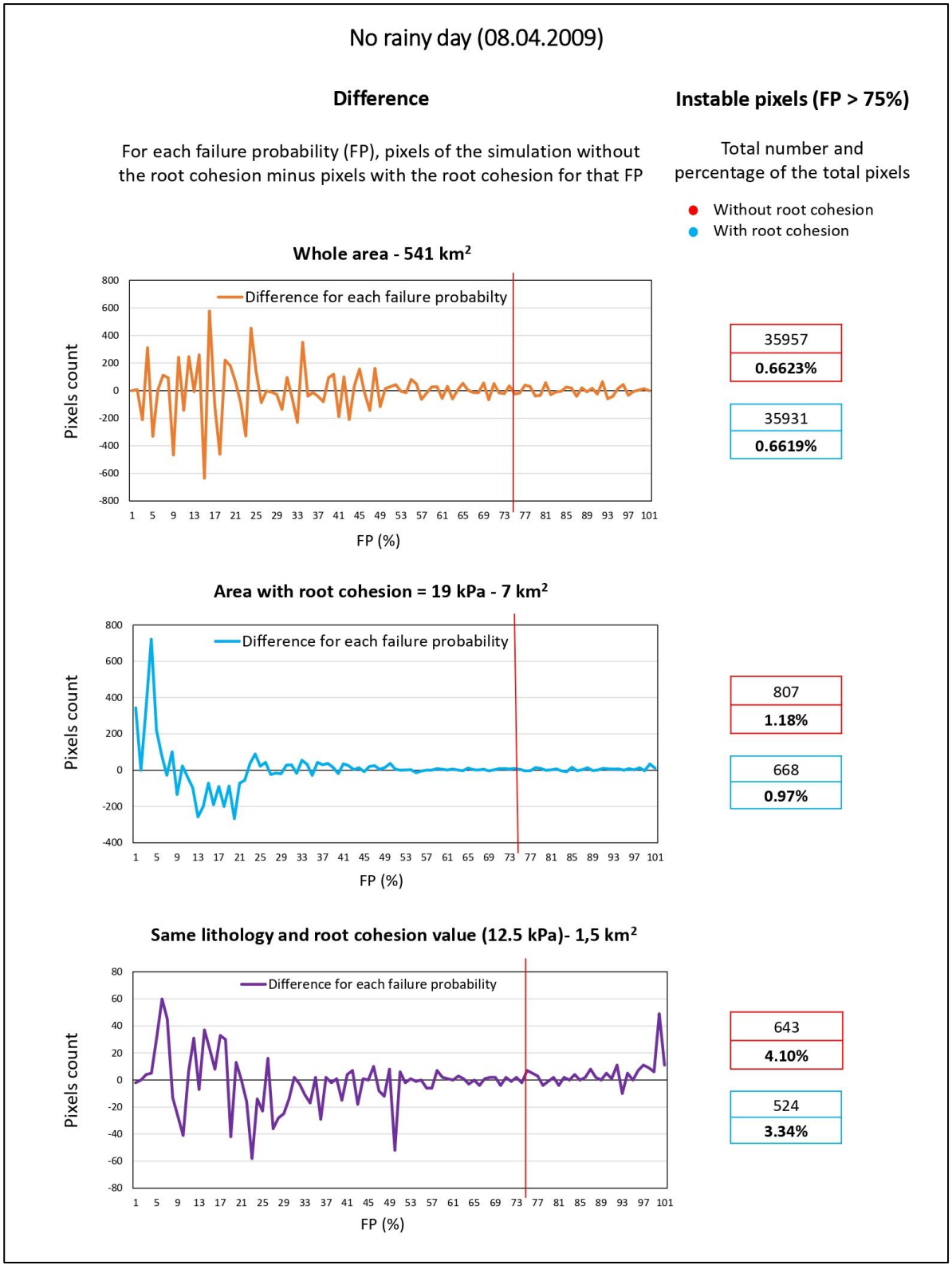

Figure 64. Comparison of the failure probability trend for a "no rainy" day (08.04.2009) of the simulations with and without the root cohesion in three different reference area: a) the whole area; b) a subarea characterized by a root cohesion mean value of 19 kPa; c) a subarea with same values of geotechnical parameters and root cohesion. On the left: the coloured line (orange, light blue, purple) represents the difference: for each FP, pixels of the simulation without the root cohesion minus pixels with root cohesion with that FP. On the right: count of the unstable pixels (FP >75), lightened in red the count of the simulation without the root cohesion, lightened in light blue the count of the simulation with the root cohesion.

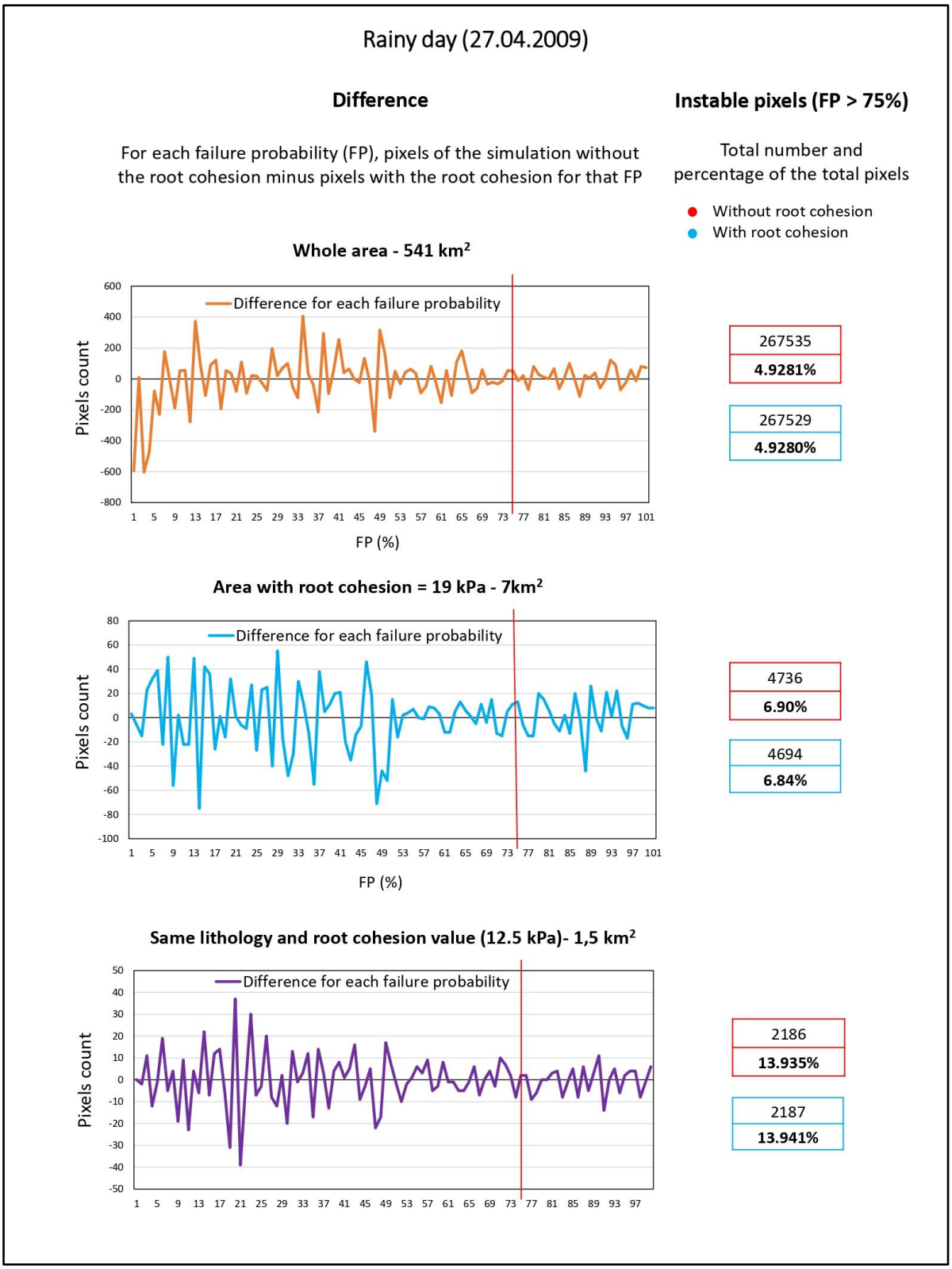

Figure 65. Comparison of the failure probability (FP) trend for a rainy day (27.04.2009) of the simulations with and without the root cohesion in three different reference area: d) the whole area; e) a subarea characterized by a root cohesion mean value of 19 kPa; f) a subarea with same values of geotechnical parameters and root cohesion. On the left: the coloured line (orange, light blue, purple) represents the difference: for each FP, pixels of the simulation without the root cohesion minus pixels with root cohesion with that FP. On the right: count of the unstable pixels (FP >75), lightened in red the count of the simulation without the root cohesion, lightened in light blue the count of the simulation with the root cohesion.

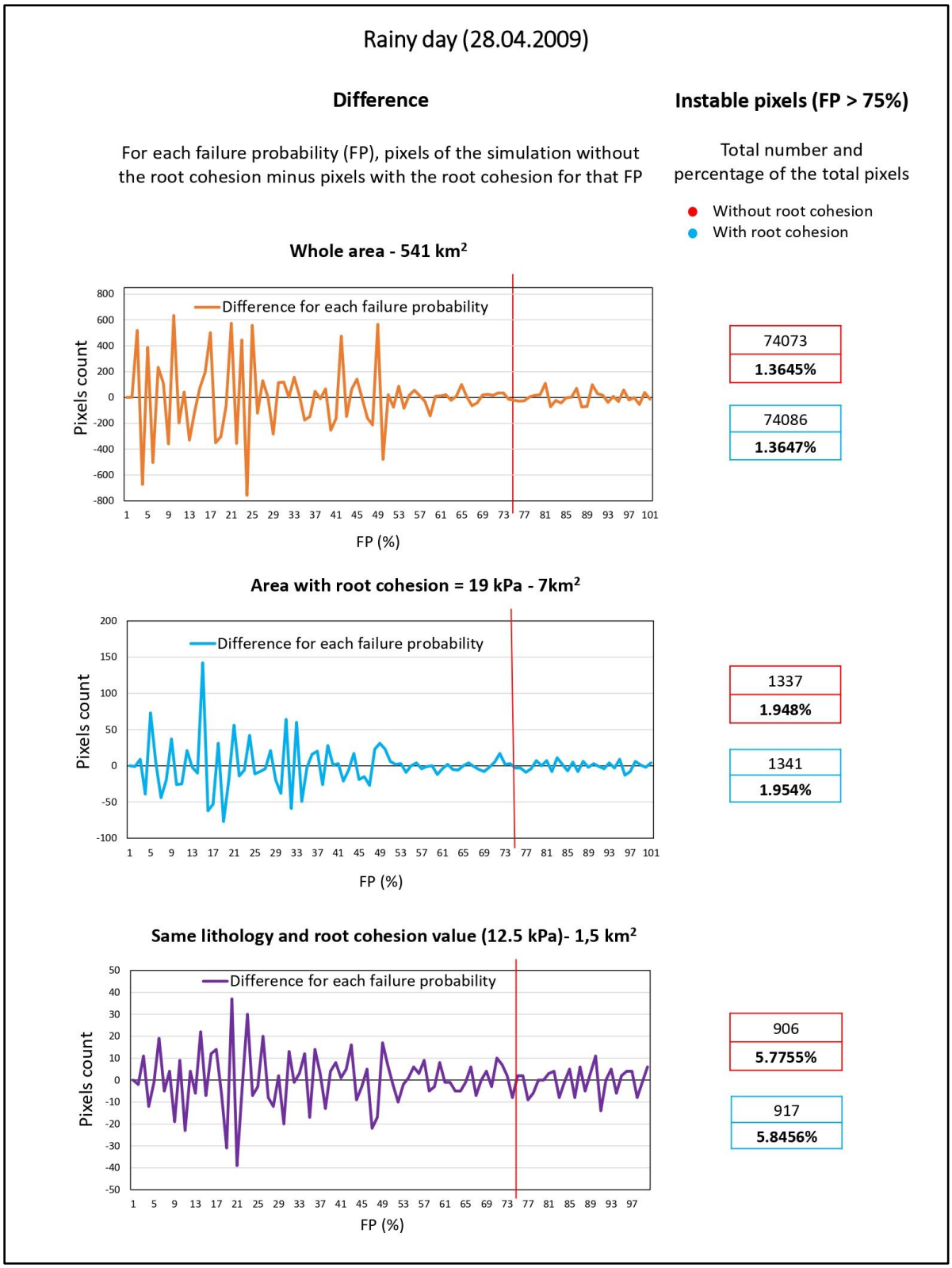

Figure 66. Comparison of the failure probability (FP) trend for a rainy day (28.04.2009) of the simulations with and without the root cohesion in three different reference area: g) the whole area; h) a subarea characterized by a root cohesion mean value of 19 kPa; i) a subarea with same values of geotechnical parameters and root cohesion. On the left: the coloured line (orange, light blue, purple) represents the difference: for each FP, pixels of the simulation without the root cohesion minus pixels with root cohesion with that FP. On the right: count of the unstable pixels (FP >75), lightened in red the count of the simulation without the root cohesion, lightened in light blue the count of the simulation with the root cohesion.

In the two rainy days (Figure 64, Figure 65) the number of unstable pixels for the two simulations is essentially the same in each case, the differences between one and the other are very low, in some cases slightly in favour of the simulation without the root cohesion (meaning higher unstable pixels for the latter), in some cases in favour of the simulation with the root cohesion (right side of the figures Figure 64Figure 65). Even from the point of view of the trend with respect to the failure probabilities, we cannot detect particular discrepancies in the behaviour of the two simulations. As can be seen in the graphs, the trend line has a balanced pattern above and below the zero in all the cases.

In Table 7, the count of pixels with a daily max failure probability higher than the 75% for the 9 cases reported in this section (figures from Figure 64Figure 66) are summarised.

Reference area	**With root cohesion**		**Without root cohesion**	
	No rainy day			
	a	b	a	b
Whole area	35931	0.6619%	35957	0.6623%
Root cohesion = 19KPa	668	0.97%	807	1.18%
Same lithology and root cohesion=12.5kPa	524	3.34%	643	4.10%
	First rainy day			
	a	b	a	b
Whole area	267529	4.9280%	267535	4.9281%
Root cohesion = 19KPa	4694	6.84%	4736	6.90%
Same lithology and root cohesion=12.5kPa	2187	13.941%	2186	13.935%
	Second rainy day			
	a	b	a	b
Whole area	74073	1.3645%	74086	1.3647%
Root cohesion = 19KPa	1341	1.954%	1337	1.948%
Same lithology and root cohesion=12.5kPa	917	5.8456%	906	5.7755%

Table 7. Comparisons of the unstable pixels of the simulation without and with the root cohesion: a) count of the pixels with failure probability > 75 % in the reference area; b) percentage of the pixels with a failure probability > 75 % normalised to the reference area.

Based on what has emerged in the data analysis of the present approach, the effect of the root cohesion has a not negligible effect in the unsaturated conditions of the soil (no rainy day), while in saturated conditions it has a not detectable impact on the results in terms of failure probabilities. The insertion of the values of additional cohesion of the present study undoubtedly produces higher values of factor of safety, but from the point of view of the failure probabilities obtained through the Monte Carlo iterations it has presumably a lower impact compared to other variables, and this behaviour it is particularly clear when the saturated conditions are reached in the simulations. The root cohesion was

modelized as a component of the "standard" cohesion in this study (equations from 11 to 14, Section 6.2.2), consequently it is subjected to the same decrease of the latter in saturated conditions due to the increase of the denominator of the second term in the right member of equation 14. This is a reasonable approach supported by the literature that reported decreases in the root cohesion as the soil moisture increases (Lian et al. 2019; Hales and Miniat, 2017; Pollen, 2007) and adopted from several authors (e.g Chock et al. 2015; Preti and Giadrossich, 2009; Hales and Miniat, 2017). But, considering that the stabilising action of vegetation in the saturated condition is indisputable when dealing with shallow mass movements, based on what emerged in this section, the model of the root cohesion that we assumed to insert the parameter in HIRESSS might not be the most suitable for the shallow landslides, in the context (vegetation, weather conditions, soil types) of the study areas of this research.

9.3.2 Cervinara case study

For the Cervinara case study, the analyses were performed on the results regarding the whole area. The selected days were the 14th of December as a day with little rainfall and the 16th of December as day with abundant rainfall.

Regarding the count of unstable pixels (with a daily max failure probability higher than the 75%), as we saw in Section 9.2.2, there are no differences between the two simulations.

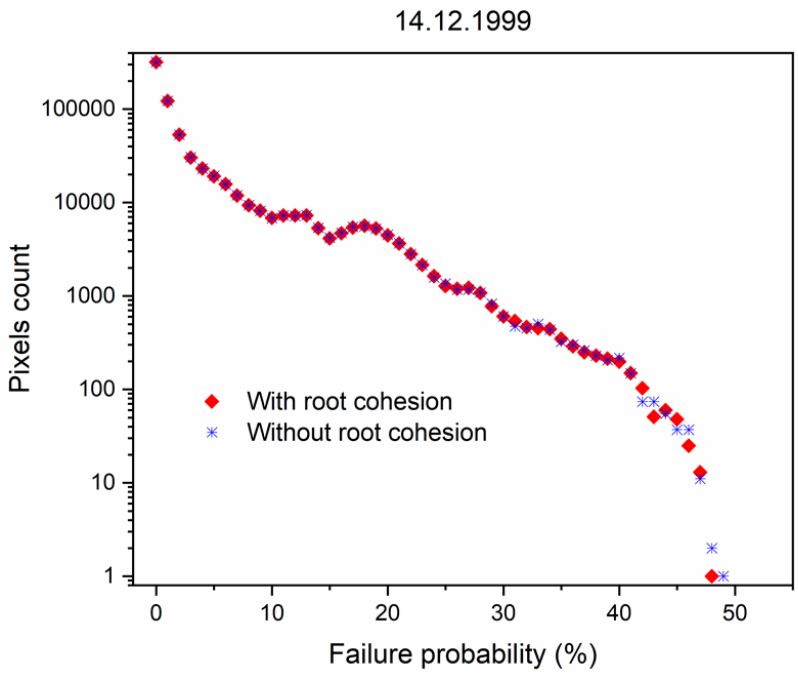

Figure 67. Comparison of the failure probability trend for a "no rainy" day (14.12.1999) of the simulations with (red square) and without (blue asterisk) the root cohesion.

About the failure probabilities (Figure 67 and Figure 68), we can observe that the 14th of December the model did not found pixels with failure probabilities higher than the 50% in both the simulations, while pixels with high failure probabilities are present in both the simulations of the 16th of December. As regards to the comparison between the simulations with or without the root cohesion, we cannot detect particular discrepant distributions of the pixels concerning the probabilities. The log scale of the graphs for the pixels count was needed to be able to represent all the data in the figure and to highlight at least some of the little discrepancies present.

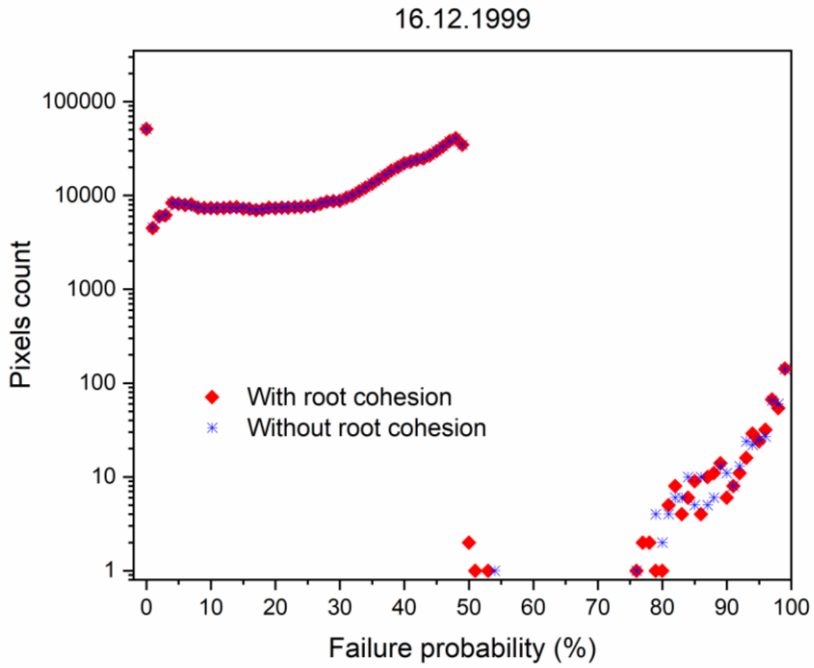

Figure 68. Comparison of the failure probability trend for a rainy day (16.12.1999) of the simulations with (red square) and without (blue asterisk) the root cohesion.

9.4 Validation

As the last phase of the evaluation of the root cohesion effect on regional scale simulations, it was planned a validation of the results obtained with or without the root cohesion considering the landslides occurred in the areas of the case studies in the simulated periods (Figure 69). The aim was to evaluate the eventual improvements obtained in the forecasting capabilities of HIRESSS.

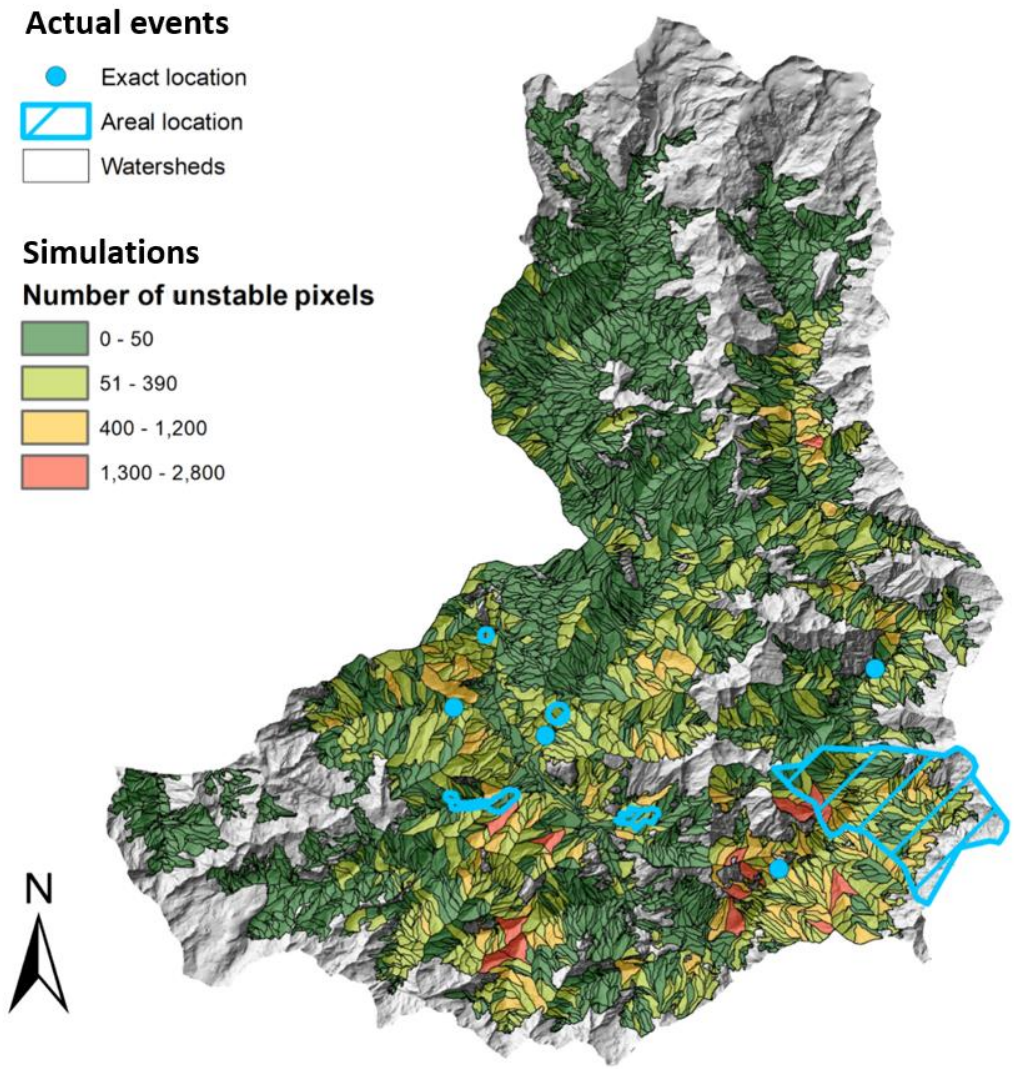

Figure 69. Simulations results compared to actual landslide events. Valle d'Aosta study area, 27.04.2009.

One of the most useful applications for which a distributed model capable of quick processing can be used is the landslides forecasting at regional scale, to support territory authorities and civil protection agencies in making decisions aimed to protect people and infrastructures from the hydrogeomorphic events.

In this perspective, the failure probabilities (FP) of each pixel are redundant information not practical to use. Rather, the results should be synthesised through a chosen criterium and expressed in the form of failure probabilities of more extended areas like the basins of a certain size, for example. The potential criteria to spatially synthesised the data are several, and the choice depends on the context and the precise purposes for which the simulations are carried out.

For this research, the pixel results of some days of the performed simulations with and without the root cohesion were synthesized into basins through different criteria: mean FP, median FP, number of pixels with the FP higher than a certain threshold (Table 8, Figure 70, and from Figure 72 to Figure 75). For each criterium, the obtained maps of the simulations with or without the root cohesion were compared to each other and with respect to the databases of the occurred landslide events.

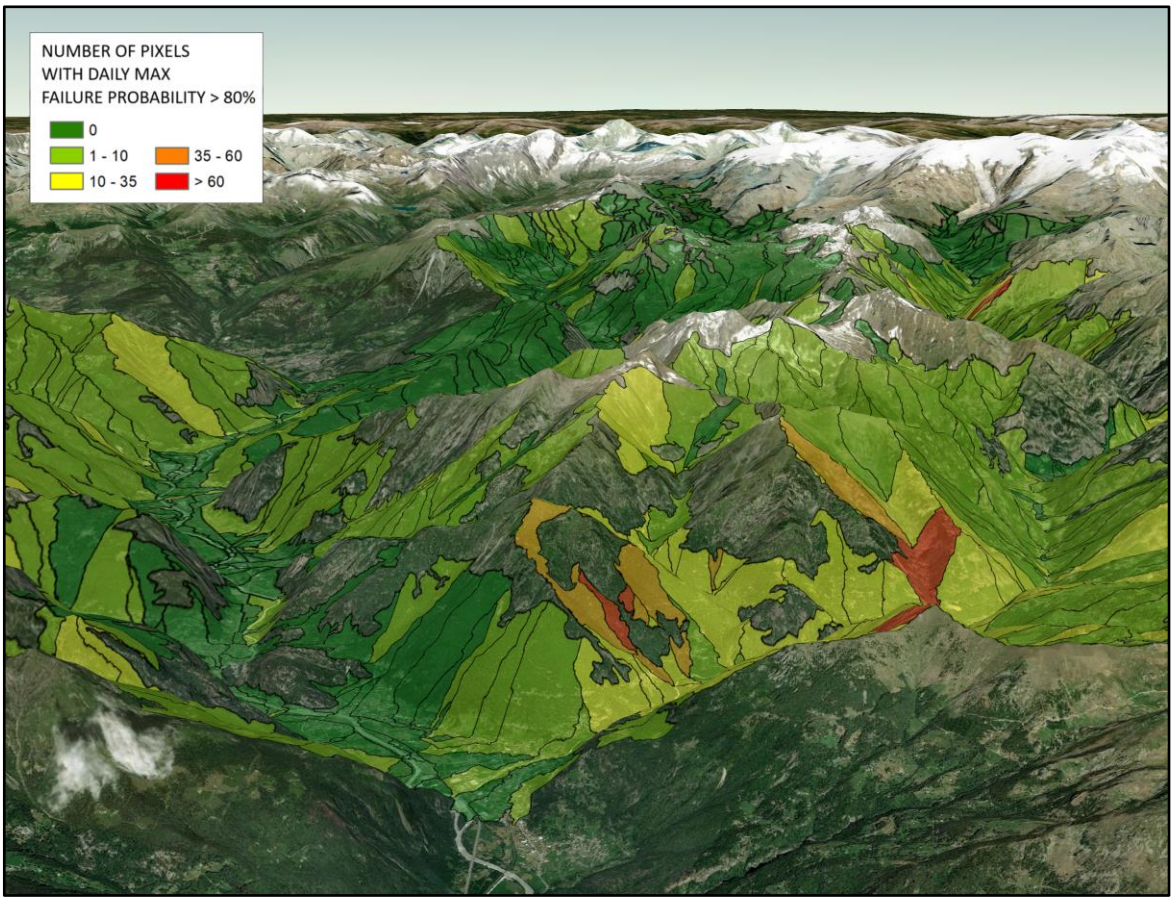

Figure 70. Pixels failure probability (FP) synthesised into number of unstable pixels per basin. Valle d'Aosta study area, 27.04.2009.

In accordance to what was emerged and discussed in the previous sections, the differences between the FP basin maps obtained in the simulations with or without the root cohesion were very little (Figure 71-Figure 75 and Table 8).

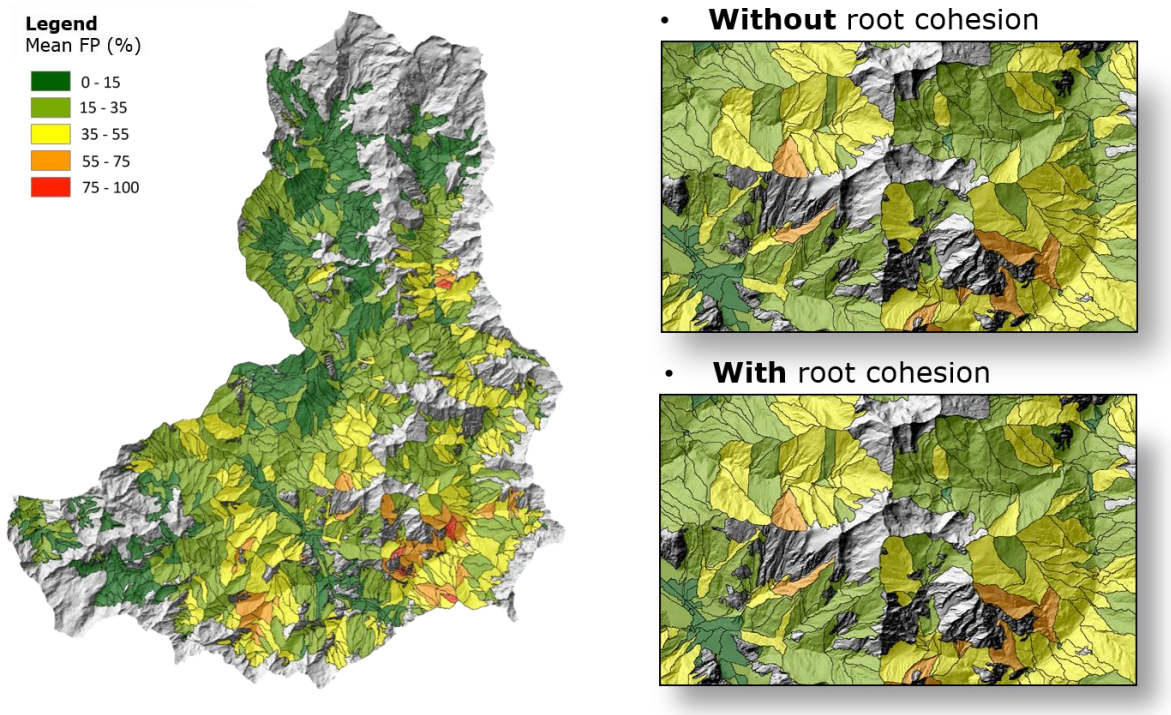

Figure 71. Valle d'Aosta case study, 27.04.2009: comparison of mean failure probability (FP) per basin of the simulations without or with the root cohesion.

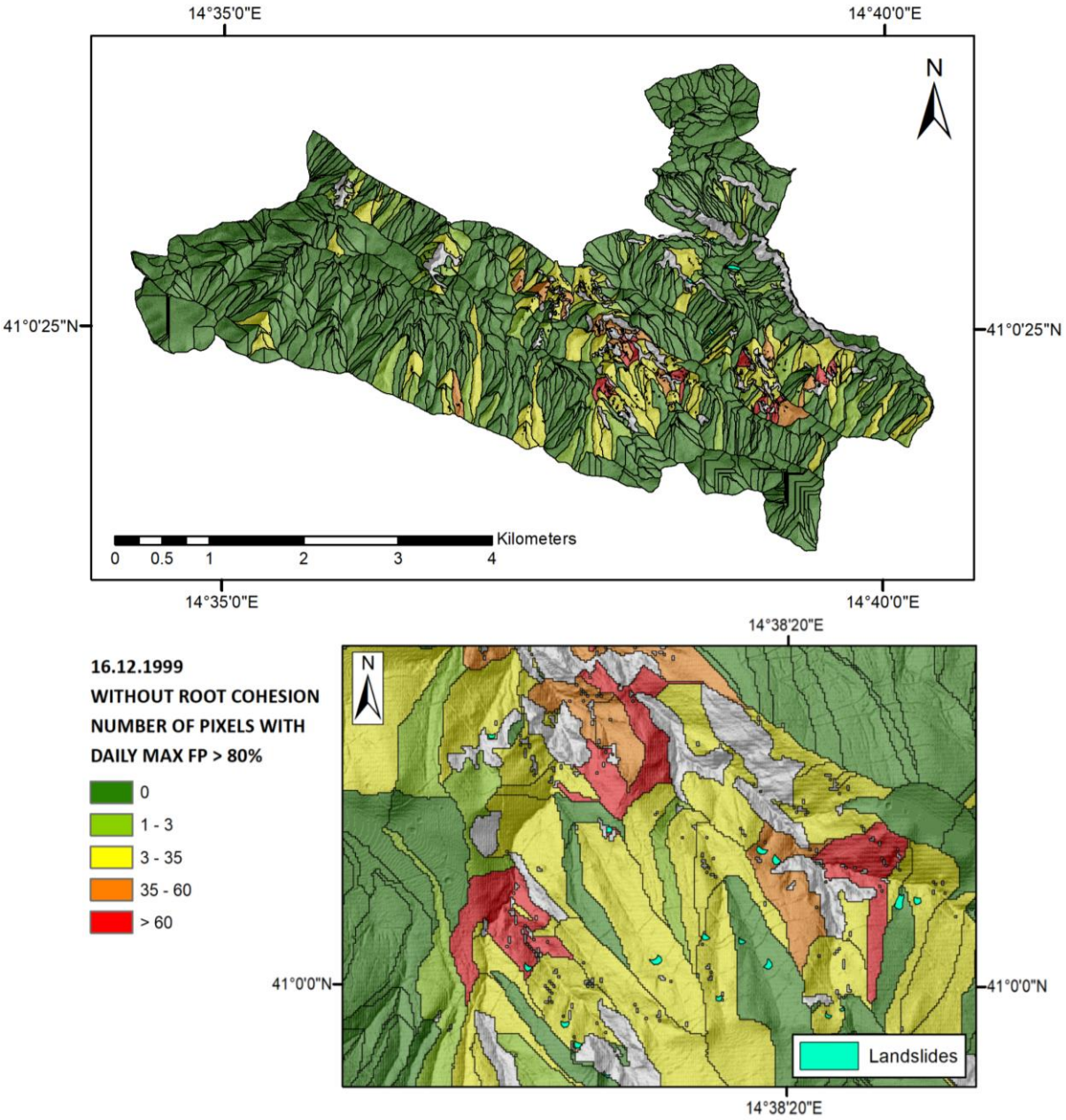

Figure 72. Cervinara case study, 16.12.1999 simulation without the root cohesion: basins number of pixels with daily max failure probability (FP) higher than 80%.

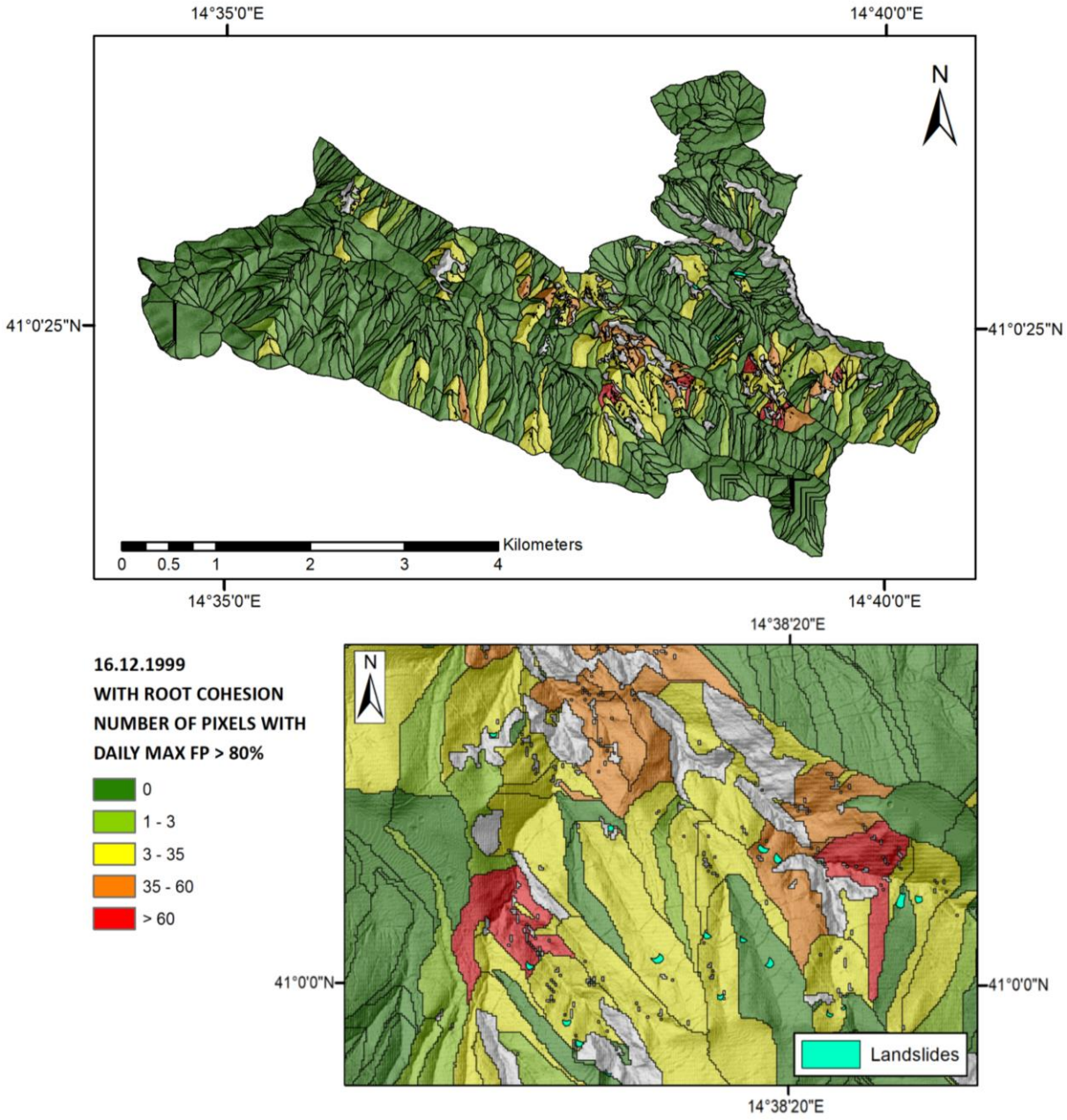

Figure 73. Cervinara case study, 16.12.1999 simulation with the root cohesion: basins number of pixels with daily max failure probability (FP) higher than 80%.

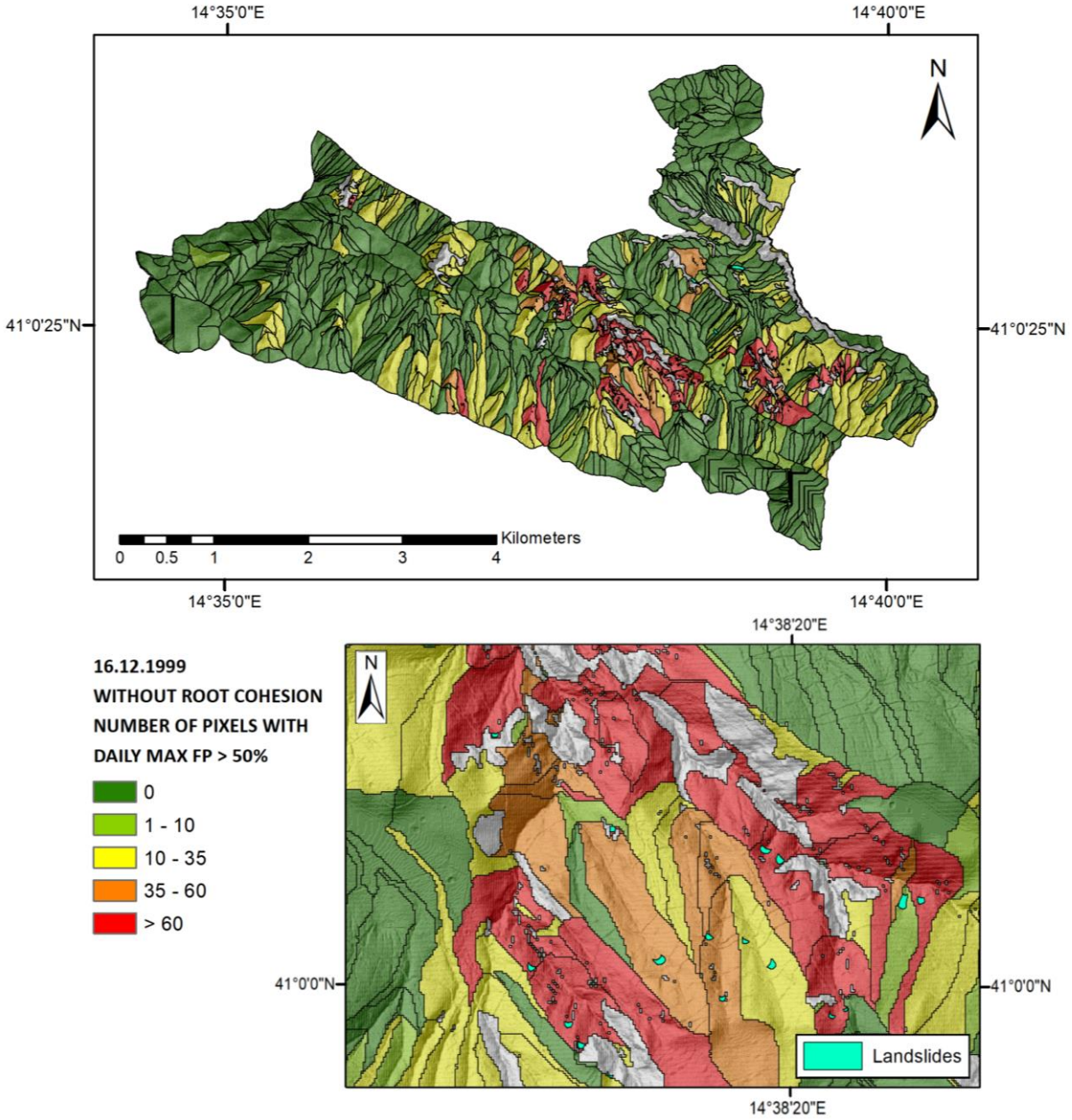

Figure 74. Cervinara case study, 16.12.1999 simulation without the root cohesion: number of pixels with the daily max failure probability (FP) higher than 50%.

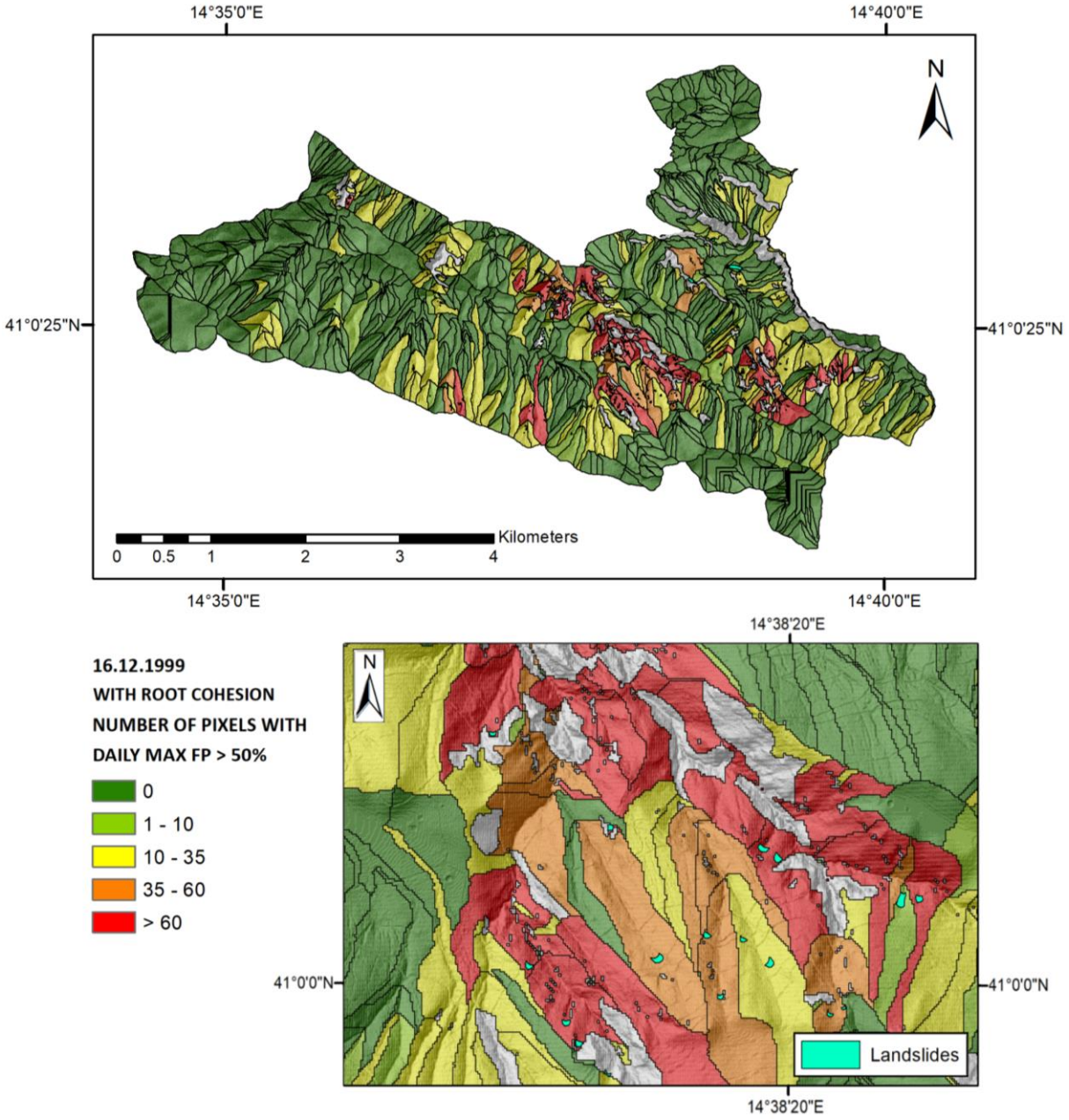

Figure 75. Cervinara case study, 16.12.1999 simulation with the root cohesion: basins number of pixels with the daily max failure probability (FP) higher than 50%.

a)

FP/pixels number	forecast landslides	TP	FN	TN	FP
80/1	92,8% (65/70)	68% (34/50)	32% (16/50)	89,7% (1519/1693)	10,3% (174/1693)
80/3	88,6% (62/70)	60% (30/50)	40% (20/50)	91,6% (1551/1693)	8,4% (142/1693)
60/5	78.6% (55/70)	54% (27/50)	46% (23/50)	94,5 (1600/1693)	5,6% (93/1693)
50/10	85,7% (60/70)	60% (30/50)	40% (20/50)	92,2% (1560/1693)	7,8% (133/1693)
45/15	84,3% (59/70)	60% (30/50)	40% (20/50)	90,3% (1529/1693)	9,7% (164/1693)
45/25	77,1% (54/70)	50% (25/50)	50% (25/50)	92 % (1557/1693)	8% (136/1693)

b)

FP/pixels number	forecast landslides	TP	FN	TN	FP
80/3 without RC	88,6% (62/70)	60% (30/50)	40% (20/50)	91,6% (1550/1693)	8,4% (143/1693)
80/3 with RC	88,6% (62/70)	60% (30/50)	40% (20/50)	91,6% (1551/1693)	8,4% (142/1693)
50/10 without RC	85,7% (60/70)	60% (30/50)	40% (20/50)	92,2% (1560/1693)	7,8% (133/1693)
50/10 with RC	85,7% (60/70)	60% (30/50)	40% (20/50)	92,2% (1560/1693)	7,8% (133/1693)

Table 8. **Validation results, where: "RC" is root cohesion; "FP" is failure probability; "FP/pixels number" represents the combination between the thresholds of failure probability and number of pixels to consider a basin as unstable (i.e. at least x pixels with a failure probability higher than y); "forecast landslides" is the number of landslides whose perimeter is at least partially overlaid with unstable basins of the model simulation; "TP" is the true positive percentage (correct alarms) i.e. the unstable areas correctly localized by the simulation (the number of unstable basins found by the model with at least one landslide inside it with respect to the actual total unstable basins); "FN" is the false negative percentage (missing alarms) i.e. the unstable areas not localized by the model (the number of the stable basins found by the model with at least one actual landslide inside it with respect to the total actual unstable basins); "TN" is the true negative percentage (correct non-alarms) i.e. the areas correctly defined stable by the model (the basins found stable by the model without landslides inside it compared to the actual total stable basins); "FP" is the false positive percentage (incorrect alarms) i.e. the areas incorrectly defined stable by the model (unstable basins found by the model without landslides inside it compared to the total actual stable basins).**
a) Validation results of the simulation with the root cohesion for different combinations of FP/pixels number; b) Comparison of the validation results between the simulation without the root cohesion and the simulation with the root cohesion.

In Table 8 the results of a comparative validation analysis are presented. The resulting maps of the simulations with and without the root cohesion for the rainy day 16.12.1999 were elaborated to analyse the forecasting capabilities of the model in the two cases. To perform the validation analysis, the pixels FP was aggregated into basins based on thresholds of number of pixels with the FP higher

than a certain value. In greater detail, the combination of FP and number of pixels chosen as threshold for the instability and perform the comparative analysis were at least 3 pixels with a FP higher than 80%, and at least 10 pixels with a FP higher than 50%. Other combinations previously explored (with the results of the simulation with the root cohesion) comparing the basins found beyond the threshold with the distribution of the landslides were 80%/1 pixel, 60%/5 pixels, 45%/15 pixels, 45%/25 pixels (Cuomo et. al., 2020). All the combinations have good values of correct alarms and incorrect alarms (Table 8a). The combinations 80%/3 pixels and 50%/10 pixels were chosen for the comparative validation analysis since considered the best compromises between correct alarms (true positives) and incorrect alarms (false positives) (Table 8a).

The differences between the simulations are so little that the percentages of correct and incorrect alarms are the same (with one digit of decimals) in the two cases, confirming what was emerged in the previous analyses.

9.5 Further developments

Based on what emerged from the data analyses and discussions, the further developments will be first of all concentrated on changing the root cohesion model to assume, to insert its contribution in the HIRESSS model. Indeed, we presume considering the findings of the present research that for the shallow landslides, in areas with the characteristics of the study (geotechnical parameters, plant species, rainfall trend), the root cohesion modelized as described does not impact enough (considered the universally recognised influence of the root reinforcement on the shallow landslides) the results of the slope stability analyses by HIRESSS in terms of failure probabilities.

Once found the most appropriate method to model the root reinforcement in the physical structure of the simulator, the research will move the attention on improving the assessing of the vegetation distribution and density, exploiting remote sensors installed on unmanned air vehicles (UAVs, or drones) as laser scanner to evaluate volume of the above parts of the plants or infrared sensors to perform detailed NDVI (Normalized Difference Vegetation Index) measures.

Successively, the project to further develop HIRESSS includes the insertion in the physical model of other significative effects of the vegetation on the hillslope stability, starting from the interception of the rainfall by the canopies.

10 Conclusions

The present study aim was to try overcoming two main lacks in the field of the distributed slope stability analyses: the lack of a distributed slope stability model capable of a very quick processing in which the root reinforcement is considered; an efficient approach to estimate the root cohesion that it has been tested in very wide areas and simulating long periods.

The comparative analyses carried out on the results of the simulations performed inserting or not the root reinforcement into the selected and modified model highlighted that the impact of this parameter is more evident in the results of the no rainy days, in terms of failure probabilities of large areas.

We attribute this finding to the modelisation adopted to insert the root cohesion into the simulator and to the fact that the results are analysed in terms of failure probabilities and not in terms of pure factor of safety values. The insertion of the values of additional cohesion of the present study undoubtedly produces higher values of factor of safety considering the equations on which the model is based on. But concerning the failure probabilities obtained through the Monte Carlo iterations, the root cohesion has presumably a lower impact compared to other variables, and this behaviour is particularly clear when the saturated conditions are reached in the simulations.

The little differences found in the failure probabilities between the simulations performed inserting or not the root cohesion have not allowed performing a validation of the results considering actual landslides events, to evaluate the eventual improvements of the forecasting capabilities of HIRESSS and the approach adopted to estimate the root reinforcement at the regional scale.

Thanks to the work carried out during the present research, it was possible to test a commonly adopted modelisation of the root cohesion in a distributed slope stability model, finding that a different model is preferable in the context of the shallow landslides, in areas similar to the ones of the study, and working in terms of failure probabilities.

This different model should represent the component of the cohesion due to the roots as following a law of decreasing with the increase of the soil water content different from the ones of the other components of the soil cohesion. In this perspective, further studies (besides the ones already done) on the relation between the root cohesion and the soil moisture will be extremely useful.

Regarding the further developments of the present research, one found the most appropriate (to our purposes) method to model the root reinforcement, the project will concentrate the efforts on improving the assessing of vegetation distribution and density, and including in HIRESSS other effects exerted by the vegetation on the hillslope stability.

References

Aleotti, P. (2004). A warning system for rainfall-induced shallow failures. *Engineering Geology*, *73*(3-4), 247-265.

Anderson, C. J., Coutts, M. P., Ritchie, R. M., & Campbell, D. J. (1989). Root extraction force measurements for Sitka spruce. *Forestry: An International Journal of Forest Research*, 62(2), 127-137.

Annunziati, A., Focardi, A., Focardi, P., Martello, S., & Vannocci, P. (2000). Analysis of the rainfall thresholds that induced debris flows in the area of Apuan Alps-Tuscany, Italy (19 June 1996 storm). In *Proc. EGS Plinius Conf. on Mediterranean Storms, Maratea, Italy* (pp. 485-493).

Arboleda RA, Martinez ML (1996) - 1992 lahars in the Pasig- Potrero River system. In: Fire and mud: eruptions and lahars of Mount Pinatubo (Newhall CG, Punongbayan RS, eds). Philippine Institute of Volcanology and Seismology. Seattle: Quezon City and University of Washington Press, 1126 pp.

Arnone, E., Caracciolo, D., Noto, L. V., Preti, F., & Bras, R. L. (2016). Modeling the hydrological and mechanical effect of roots on shallow landslides. *Water Resources Research*, *52*(11), 8590-8612.Baum et al., 2002

Baum, R. L., Godt, J. W., Harp, E. L., McKenna, J. P., & McMullen, S. R. (2005). Early warning of landslides for rail traffic between Seattle and Everett, Washington, USA. In *Landslide Risk Management* (pp. 741-750). CRC Press.

Beaudoin, J. J. (1990). Handbook of fiber-reinforced concrete. Principles, properties, developments and applications.

Bicocchi, G., D'Ambrosio, M., Rossi, G., Rosi, A., Tacconi-Stefanelli, C., Segoni, S., Nocentini, M., Vannocci, P., Tofani, V., Casagli, N., & Catani, F. (2016). Shear strength and permeability in situ measures to improve landslide forecasting models: a case study in the Eastern Tuscany (Central Italy). *Landslides and engineered slopes. Experience, theory and practice*, 419-424.;

Bilotta, E., Cascini, L., Foresta, V., & Sorbinow, G. (2005). Geotechnical characterisation of pyroclastic soils involved in huge flowslides. *Geotechnical & Geological Engineering*, 23(4), 365-402.

Bischetti, G. B., Chiaradia, E. A., Epis, T., & Morlotti, E. (2009). Root cohesion of forest species in the Italian Alps. *Plant and Soil*, 324(1-2), 71-89.;

Bischetti, G.B., Chiaradia, E.A., Simonato, T., Speziali, B., Vitali, B., Vullo, P., Zocco, A., 2005. Root strength and root area ratio of forest species in Lombardy (northern Italy). *Plant and Soil*, 278. pp. 11–22.

Bistacchi, A., Dal Piaz, G., Massironi, M., Zattin, M., & Balestrieri, M. (2001). The Aosta–Ranzola extensional fault system and Oligocene–Present evolution of the Austroalpine–Penninic wedge in the northwestern Alps. *International Journal of Earth Sciences*, 90(3), 654-667.

Böhm W. (1979). Methods of Studying Root systems, *Ecological Series* No. 33. Springer-Verlag, Berlin.

Bolley, S., & Oliaro, P. (1999). Analisi dei debris flows in alcuni bacini campione dell'Alta Val Susa. *Geoingegneria Ambientale e Mineraria*, Marzo, 69-74.

Bonnard, C., & Noverraz, F. (2001). Influence of climate change on large landslides: Assessment of long-term movements and trends. In *International Conference on Landslides: Causes, Impacts and Countermeasures* (No. CONF, pp. 121-138). VGE.

Brunetti, M. T., Peruccacci, S., Rossi, M., Luciani, S., Valigi, D., & Guzzetti, F. (2010). Rainfall thresholds for the possible occurrence of landslides in Italy. *Natural Hazards and Earth System Sciences*, 10(3), 447-458.

Burylo, M., Hudek, C., & Rey, F. (2011). Soil reinforcement by the roots of six dominant species on eroded mountainous marly slopes (Southern Alps, France). *Catena*, 84(1-2), 70-78.

Caine, N. (1980). The rainfall intensity-duration control of shallow landslides and debris flows. *Geografiska annaler: series A, physical geography*, 62(1-2), 23-27.

Calcaterra, D., Parise, M., Palma, B., & Pelella, L. (2000). The influence of meteoric events in triggering shallow landslides in pyroclastic deposits of Campania, Italy. *In Landslides in Research, Theory and Practice: Proceedings of the 8th International Symposium on Landslides held in Cardiff on 26–30 June 2000 (pp. 1-209).* Thomas Telford Publishing.

Campbell, R. H. (1974). Debris flows originating from soil slips during rainstorms in Southern California. *Quarterly Journal of Engineering Geology*, 7(4), 339-349.

Campbell, R. H. (1975). *Soil slips, debris flows, and rainstorms in the Santa Monica Mountains and vicinity, southern California* (Vol. 851). US Government Printing Office.

Cannon, S. H., & Gartner, J. E. (2005). Wildfire-related debris flow from a hazards perspective. In *Debris-flow hazards and related phenomena* (pp. 363-385). Springer, Berlin, Heidelberg.

Cardinal, M., Galli, M., Guzzetti, F., Ardizzone, F., Reichenbach, P., & Bartoccini, P. (2006). Rainfall induced landslides in December Southwestern Umbria, Central Italy. *Natural Hazards and Earth System Sciences*, 6, 237-260.

Carslaw, H. S. and Jaeger, J. C. (1959): *Conduction of Heat in Solids*, Oxford Univ. Press, New York.

Casadei, M., Dietrich, W. E., & Miller, N. L. (2003). Testing a model for predicting the timing and location of shallow landslide initiation in soil-mantled landscapes. *Earth Surface Processes and Landforms: The Journal of the British Geomorphological Research Group*, 28(9), 925-950.

Casagrande, A. (1976). Liquefaction and cyclic deformation of sands-a critical review. *Harvard Soil Mechanics Series, Harvard University, Cambridge, Massachusetts.,* (88).

Cascini, L., Bonnard, C., Corominas, J., Jibson, R., & Montero-Olarte, J. (2005). Landslide hazard and risk zoning for urban planning and development. *In Landslide risk management* (pp. 209-246). CRC Press.

Cascini, L., Cuomo, S., & Della Sala, M. (2011). Spatial and temporal occurrence of rainfall-induced shallow landslides of flow type: A case of Sarno-Quindici, Italy. *Geomorphology*, 126(1-2), 148-158

Cascini, L., Cuomo, S., & Guida, D. (2008). Typical source areas of May 1998 flow-like mass movements in the Campania region, Southern Italy. *Engineering Geology*, 96(3-4), 107-125.

Catani, F., Segoni, S., & Falorni, G. (2010). An empirical geomorphology-based approach to the spatial prediction of soil thickness at catchment scale. *Water Resources Research*, 46(5).

Chave, J., Coomes, D., Jansen, S., Lewis, S. L., Swenson, N. G., & Zanne, A. E. (2009). Towards a worldwide wood economics spectrum. *Ecology letters*, 12(4), 351-366.

Chiang, S. H., & Chang, K. T. (2011). The potential impact of climate change on typhoon-triggered landslides in Taiwan, 2010–2099. *Geomorphology,* 133(3-4), 143-151

Chien-Yuan, C., Tien-Chien, C., Fan-Chieh, Y., & Sheng-Chi, L. (2005). Analysis of time-varying rainfall infiltration induced landslide. *Environmental Geology*, 48(4-5), 466-479.Chleborad, 2003

Cislaghi, A., Chiaradia, E. A., & Bischetti, G. B. (2017). Including root reinforcement variability in a probabilistic 3D stability model. *Earth Surface Processes and Landforms*, 42(12), 1789-1806.

Coppin, N. J., & Richards, I. G. (Eds.). (1990). Use of vegetation in civil engineering (pp. 23-36). *London: Construction Industry Research and Information Association.*

Costa, C., Dwyer, L. M., Hamilton, R. I., Hamel, C., Nantais, L., & Smith, D. L. (2000). A sampling method for measurement of large root systems with scanner-based image analysis. *Agronomy Journal*, 92(4), 621-627.

Costa, J. E. (1984). Physical geomorphology of debris flows*. In Developments and applications of geomorphology* (pp. 268-317). Springer, Berlin, Heidelberg.

Crosta, G. (1998). Rainfall threshold regionalization: an aid for landslide susceptibility zonation. *Environmental Geology*, 35(2/3), 131-145.

Crosta, G. B., & Frattini, P. (2008). Rainfall-induced landslides and debris flows. *Hydrological Processes: An International Journal*, 22(4), 473-477.

Crozier, M. J. (1997). The climate-landslide couple: a southern hemisphere perspective. *Rapid mass movement as a source of climatic evidence for the Holocene*, 333-354.

Cuomo, S., & Foresta, V. (2015). Penetration tests in shallow layered unsaturated pyroclastic soil deposits of Southern Italy. In *From Fundamentals to Applications in Geotechnics: Proceedings of the 15th Pan-American Conference on Soil Mechanics and Geotechnical Engineering, 15–18 November 2015, Buenos Aires, Argentina* (p. 454). IOS Press.

Cuomo, S., & Iervolino, A. (2016). Investigating the role of stratigraphy in large-area physically-based analysis of December 1999 Cervinara shallow landslides. *Journal of Mountain Science*, 13(1), 104-115.

Cuomo, S., Masi, E. B., Tofani, V., Moscariello, M., Rossi, G., & Matano, F. (2020) Short- and long-term slope stability analysis in a large area of unsaturated pyroclastic soils. *In preparation.*

Damiano, E., Olivares, L., & Picarelli, L. (2012). Steep-slope monitoring in unsaturated pyroclastic soils. *Engineering Geology*, 137, 1-12.

De Baets, S., Poesen, J., Reubens, B., Wemans, K., De Baerdemaeker, J., & Muys, B. (2008). Root tensile strength and root distribution of typical Mediterranean plant species and their contribution to soil shear strength. *Plant and soil*, 305(1-2), 207-226.

Del Soldato, M., Segoni, S., De Vita, P., Pazzi, V., Tofani, V., & Moretti, S. (2016). Thickness model of pyroclastic soils along mountain slopes of Campania (southern Italy). *Landslides and Engineered Slopes. Experience, Theory and Practice; Aversa, S., Cascini, L., Picarelli, L., Scavia*, C., Eds, 797-804.

Denlinger, R. P., & Iverson, R. M. (1990). Limiting equilibrium and liquefaction potential in infinite submarine slopes. *Marine Georesources & Geotechnology*, 9(4), 299-312.

Dhakal, A. S., & Sidle, R. C. (2003). Long-term modelling of landslides for different forest management practices. Earth Surface Processes and Landforms: *The Journal of the British Geomorphological Research Group*, 28(8), 853-868.

Dietrich, W. E., de Asua, R. R., Coyle, J., Orr, B., & Trso, M. (1998). A validation study of the shallow slope stability model, SHALSTAB, in forested lands of Northern California. *Stillwater Ecosystem, Watershed & Riverine Sciences. Berkeley, CA*.

Docker, B. B., & Hubble, T. C. T. (2008). Quantifying root-reinforcement of river bank soils by four Australian tree species. *Geomorphology*, 100(3-4), 401-418.

Dowdy, R. H., Smucker, A. J. M., Dolan, M. S., & Ferguson, J. C. (1998). Automated image analyses for separating plant roots from soil debris elutriated from soil cores. *Plant and soil*, 200(1), 91-94.

Ellen, S. (1988). Description and mechanics of soil slip/debris flow in the storm of january 3-5, 1982, in the the san francisco bay region, california. *US Geological Survey Professional Paper*, 1434, 64-111.

Ellen, S. D., & Fleming, R. W. (1987). Mobilization of debris flows from soil slips, San Francisco Bay region, California. *Debris F10ws/Avalanches: Process, Recognition, and Mitigation. Geological Society of America, Boulder*, CO, 31-40.

Ennos, A. R. (1990). The anchorage of leek seedlings: the effect of root length and soil strength. *Annals of Botany*, 65(4), 409-416.

Fan, C. C., & Su, C. F. (2008). Role of roots in the shear strength of root-reinforced soils with high moisture content. *Ecological Engineering*, 33(2), 157-166.

Fiorillo, F., & Guadagno, F. (2011). Rainfall initiation of debris avalanche-flows in Campania (Italy): a two-phase analysis. *In 5th International Conference on Debris-Flow Hazards Mitigation* (pp. 53-62).

Fiorillo, F., & Wilson, R. C. (2004). Rainfall induced debris flows in pyroclastic deposits, Campania (southern Italy). *Engineering Geology*, 75(3-4), 263-289.

Fiorillo, F., Guadagno, F., Aquino, S., & De Blasio, A. (2001). The December 1999 Cervinara landslides: further debris flows in the pyroclastic deposits of Campania (southern Italy). *Bulletin of Engineering Geology and the Environment*, 60(3), 171-184.

Floris, M., Mari, M., Romeo, R. W., & Gori, U. (2004). Modelling of landslide-triggering factors-A case study in the northern Apennines, Italy. *In Engineering geology for infrastructure planning in Europe* (pp. 745-753). Springer, Berlin, Heidelberg.

Forbes, K., & Broadhead, J. (2013). Forests and landslides: The role of trees and forests in the prevention of landslides and rehabilitation of landslide-affected areas in Asia. *Rap Publication*, (2013/02).

Fredlund, D. G. (1987). Slope stability analysis incorporating the effect of soil suction. *Slope Stability,* 113-144.

Fredlund, D. G., & Rahardjo, H. (1993). Soil mechanics for unsaturated soils. John Wiley & Sons.

Fredlund, D. G., Morgenstern, N. R., & Widger, R. A. (1978). The shear strength of unsaturated soils. Canadian geotechnical journal, 15(3), 313-321.

Gan, J. K. M., Fredlund, D. G., & Rahardjo, H. (1988). Determination of the shear strength parameters of an unsaturated soil using the direct shear test. *Canadian Geotechnical Journal*, 25(3), 500-510.

Gao, T., Xu, B., Yang, X., Jin, Y., Ma, H., Li, J., & Yu, H. (2013). Using MODIS time series data to estimate aboveground biomass and its spatio-temporal variation in Inner Mongolia's grassland between 2001 and 2011. *International Journal of Remote Sensing*, 34(21), 7796-7810.;

Genet, M., Kokutse, N., Stokes, A., Fourcaud, T., Cai, X., Ji, J., & Mickovski, S. (2008). Root reinforcement in plantations of Cryptomeria japonica D. Don: effect of tree age and stand structure on slope stability. *Forest ecology and Management*, 256(8), 1517-1526.

Genet, M., Li, M., Luo, T., Fourcaud, T., Clément-Vidal, A., & Stokes, A. (2010). Linking carbon supply to root cell-wall chemistry and mechanics at high altitudes in Abies georgei. *Annals of botany*, 107(2), 311-320.

Genet, M., Stokes, A., Salin, F., Mickovski, S. B., Fourcaud, T., Dumail, J. F., & Van Beek, R. (2005). The influence of cellulose content on tensile strength in tree roots. *Plant and soil*, 278(1-2), 1-9.

Giadrossich, F., Guastini, E., Preti, F., & Vannocci, P. (2010). Metodologie sperimentali per l'esecuzione di prove di taglio diretto su terre rinforzate con radici Experimental methodologies for the direct shear tests on soils reinforced by roots.

Giannecchini, R. (2005). Rainfall triggering soil slips in the southern Apuan Alps (Tuscany, Italy).

Gray, D. H., & Leiser, A. T. (1982). Biotechnical slope protection and erosion control. Van Nostrand Reinhold Company Inc.

Gray, D. H., & Ohashi, H. (1983). Mechanics of fiber reinforcement in sand. *Journal of Geotechnical Engineering,* 109(3), 335-353.

Gray, D. H., & Sotir, R. B. (1996). Biotechnical and soil bioengineering slope stabilization: a practical guide for erosion control. John Wiley & Sons.

Grayston, S. J., Vaughan, D., & Jones, D. (1997). Rhizosphere carbon flow in trees, in comparison with annual plants: the importance of root exudation and its impact on microbial activity and nutrient availability. *Applied soil ecology*, 5(1), 29-56.

Green, W. H., & Ampt, G. A. (1911). Studies on Soil Phyics. *The Journal of Agricultural Science*, 4(1), 1-24.

Greenway, D.R. (1987). Vegetation and slope stability. In: *Anderson, M.G., Richards, K.S. (Eds.), Slope Stability. Wiley, Chichester,* pp. 187–230.

Guzzetti, F., Peruccacci, S., Rossi, M., & Stark, C. P. (2008). The rainfall intensity–duration control of shallow landslides and debris flows: an update. *Landslides*, 5(1), 3-17.

Hales, T. C. (2018). Modelling biome-scale root reinforcement and slope stability. *Earth Surface Processes and Landforms*, 43(10), 2157-2166.

Hales, T. C., & Miniat, C. F. (2017). Soil moisture causes dynamic adjustments to root reinforcement that reduce slope stability. *Earth Surface Processes and Landforms*, 42(5), 803-813.

Hales, T. C., Cole-Hawthorne, C., Lovell, L., & Evans, S. L. (2013). Assessing the accuracy of simple field based root strength measurements. *Plant and soil*, 372(1-2), 553-565.

Hales, T. C., Ford, C. R., Hwang, T., Vose, J. M., & Band, L. E. (2009). Topographic and ecologic controls on root reinforcement. *Journal of Geophysical Research: Earth Surface*, 114(F3).

Hong, Y., Hiura, H., Shino, K., Sassa, K., Suemine, A., Fukuoka, H., & Wang, G. (2005). The influence of intense rainfall on the activity of large-scale crystalline schist landslides in Shikoku Island, Japan. *Landslides*, 2(2), 97-105.

Hungr, O., Evans, S. G., & Hutchinson, I. N. (2001). A Review of the Classification of Landslides of the Flow Type. *Environmental & Engineering Geoscience*, 7(3), 221-238.

Hungr, O., Leroueil, S., & Picarelli, L. (2014). The Varnes classification of landslide types, an update. *Landslides*, 11(2), 167-194.

Hwang, T., Band, L. E., Hales, T. C., Miniat, C. F., Vose, J. M., Bolstad, P. V., Miles, B. & Price, K. (2015). Simulating vegetation controls on hurricane-induced shallow landslides with a distributed ecohydrological model. Journal of Geophysical Research: *Biogeosciences*, 120(2), 361-378.

Innes, J. L. (1983). Debris flows. *Progress in Physical Geography,* 7(4), 469-501.

Iverson, R. M. (1997). The physics of debris flows. *Reviews of geophysics*, 35(3), 245-296.

Iverson, R. M. (2000). Landslide triggering by rain infiltration. *Water resources research*, 36(7), 1897-1910.

Iverson, R. M. (2003). The debris-flow rheology myth. *Debris-flow hazards mitigation: mechanics, prediction, and assessment*, 1, 303-314.

Iverson, R. M., & LaHusen, R. G. (1989). Dynamic pore-pressure fluctuations in rapidly shearing granular materials. *Science*, 246(4931), 796-799.

Iverson, S. J., Frost, K. J., & Lowry, L. F. (1997). Fatty acid signatures reveal fine scale structure of foraging distribution of harbor seals and their prey in Prince William Sound, Alaska. *Marine Ecology Progress Series*, 151, 255-271.

Jiang, W., Yuan, L., Wang, W., Cao, R., Zhang, Y., & Shen, W. (2015). Spatio-temporal analysis of vegetation variation in the Yellow River Basin. *Ecological Indicators*, 51, 117-126.

Jibson, R. W. (1989). Debris flows in southern Puerto Rico. Landslide processes of the eastern United States and Puerto Rico, *Geological Society of America special paper*, 236, 29-55

Johnson, A. M., & Rodine, J. R. (1984). *Slope instability. Wiley*, 535, 257-361.

Keim, R. F., & Skaugset, A. E. (2003). Modelling effects of forest canopies on slope stability. *Hydrological Processes*, 17(7), 1457-1467.

Kim, J., Jeong, S., Park, S., & Sharma, J. (2004). Influence of rainfall-induced wetting on the stability of slopes in weathered soils. *Engineering Geology*, 75(3-4), 251-262.

Krahn, J. (2004). Seepage modeling with SEEP/W: An engineering methodology. *GEO-SLOPE International Ltd. Calgary, Alberta, Canada*.

Krahn, J., Fredlund, D. G., & Klassen, M. J. (1989). Effect of soil suction on slope stability at Notch Hill. *Canadian Geotechnical Journal*, 26(2), 269-278.

Larsen, M. C., & Simon, A. (1993). A rainfall intensity-duration threshold for landslides in a humid-tropical environment, Puerto Rico. *Geografiska Annaler: Series A, Physical Geography*, 75(1-2), 13-23.

Leung, A. K., Garg, A., & Ng, C. W. W. (2015). Effects of plant roots on soil-water retention and induced suction in vegetated soil. *Engineering Geology*, 193, 183-197.

Mahannopkul, K., & Jotisankasa, A. (2019). Influence of root suction on tensile strength of Chrysopogon zizanioides roots and its implication on bioslope stabilization. *Journal of Mountain Science*, 16(2), 275-284.

Mao, Z., Saint-André, L., Genet, M., Mine, F. X., Jourdan, C., Rey, H., Courbaud, B., & Stokes, A. (2012). Engineering ecological protection against landslides in diverse mountain forests: choosing cohesion models. *Ecological Engineering*, 45, 55-69.

Mercalli, L., & Berro, D. C. (2016). Cambiamenti climatici e impatti sui territori montani. *Scienze del Territorio*, 4, 44-57.

Montgomery, D. R., & Dietrich, W. E. (1994). A physically based model for the topographic control on shallow landsliding. *Water resources research*, 30(4), 1153-1171.

Montgomery, D. R., Schmidt, K. M., Greenberg, H. M., & Dietrich, W. E. (2000). Forest clearing and regional landsliding. *Geology*, 28(4), 311-314.

Moser, M., & Hohensinn, F. (1983). Geotechnical aspects of soil slips in Alpine regions. *Engineering Geology*, 19(3), 185-211.

Ng, C. W., & Pang, Y. W. (2000). Influence of stress state on soil-water characteristics and slope stability. *Journal of geotechnical and geoenvironmental engineering*, 126(2), 157-166.

Niklas, K. J. (1992). Plant biomechanics: an engineering approach to plant form and function. University of Chicago press

Norris, J. E. (2005). Root reinforcement by hawthorn and oak roots on a highway cut-slope in Southern England. *Plant and Soil*, 278(1-2), 43-53.

Okimura, T., & Ichikawa, R. (1985). A prediction method for surface failures by movements of infiltrated water in a surface soil layer. *Natural Disaster Science*, 7(1), 41-51.

O'Loughlin, C. L. (1974). The effect of timber removal on the stability of forest soils. New Zealand Forest Service.

Operstein, V., & Frydman, S. (2000). The influence of vegetation on soil strength. *Proceedings of the Institution of Civil Engineers-Ground Improvement*, 4(2), 81-89.

Osman, N., & Barakbah, S. S. (2011). The effect of plant succession on slope stability. *Ecological Engineering*, 37(2), 139-147.

Pack, R. T., Tarboton, D. G., & Goodwin, C. N. (1998, September). The SINMAP approach to terrain stability mapping*. In 8th congress of the international association of engineering geology, Vancouver, British Columbia, Canada* (Vol. 21, p. 25)

Pack, R. T., Tarboton, D. G., & Goodwin, C. N. (2001). Assessing terrain stability in a GIS using SINMAP.

Pan, W. B., Bolton, R. P., Lundquist, E. J., & Hiller, L. K. (1998). Portable rhizotron and color scanner system for monitoring root development. In *Root Demographics and Their Efficiencies in Sustainable Agriculture, Grasslands and Forest Ecosystems* (pp. 745-756). Springer, Dordrecht.

Paronuzzi, P., & Gnech, D. (2007). Frane di crollo indotte da piogge intense: la casistica del Friuli-Venezia Giulia (Italia NE). *Giornale di Geologia Applicata*, 6, 55-64.

Paronuzzi, P., Coccolo, A., & Garlatti, G. (1998). Eventi meteorici critici e debris flows nei bacini montani del Friuli. La Acqua, *Sezione I-Memorie*, 39-50.

Phillips, C. J., & Watson, A. J. (1994). Structural tree root research in New Zealand, a review. *Landcare Research Science Series 7*.

Pierson, T. C. (1980). Piezometric response to rainstorms in forested hillslope drainage depressions. *Journal of Hydrology* (New Zealand), 1-10.

Pierson, T. C. (1983). Soil pipes and slope stability. *Quarterly Journal of Engineering Geology and Hydrogeology*, 16(1), 1-11.

Pollen, N. (2007). Temporal and spatial variability in root reinforcement of streambanks: accounting for soil shear strength and moisture. *Catena,* 69(3), 197-205.

Pollen, N., & Simon, A. (2005). Estimating the mechanical effects of riparian vegetation on stream bank stability using a fiber bundle model. *Water Resources Research*, 41(7).

Pollen, N., Simon, A., & Collison, A. (2004). Advances in assessing the mechanical and hydrologic effects of riparian vegetation on streambank stability. *Riparian vegetation and fluvial geomorphology*, 8, 125-139.

Pollen-Bankhead, N., & Simon, A. (2010). Hydrologic and hydraulic effects of riparian root networks on streambank stability: Is mechanical root-reinforcement the whole story?. *Geomorphology*, 116(3-4), 353-362.

Pradel, D., & Raad, G. (1993). Effect of permeability on surficial stability of homogeneous slopes. *Journal of geotechnical engineering*, 119(2), 315-332.

Rahardjo, H., Lim, T. T., Chang, M. F., & Fredlund, D. G. (1995). Shear-strength characteristics of a residual soil. *Canadian Geotechnical Journal*, 32(1), 60-77.

Rao, S. M. (1996). Role of apparent cohesion in the stability of Dominician allophane soil slopes. *Engineering Geology*, 43(4), 265-279.

Rawls, W. J., Brakensiek, D. L., & Saxtonn, K. E. (1982). Estimation of soil water properties. *Transactions of the ASAE*, 25(5), 1316-1320.

Reichenbach, P., Cardinali, M., De Vita, P., & Guzzetti, F. (1998). Regional hydrological thresholds for landslides and floods in the Tiber River Basin (central Italy). *Environmental Geology*, 35(2-3), 146-159.

Reneau, S. L., & Dietrich, W. E. (1987). Size and location of colluvial landslides in a steep forested landscape. IN: *Erosion and Sedimentation in the Pacific Rim. IAHS Publication*, (165).

Reubens, B., Poesen, J., Danjon, F., Geudens, G., & Muys, B. (2007). The role of fine and coarse roots in shallow slope stability and soil erosion control with a focus on root system architecture: a review. *Trees*, 21(4), 385-402.

Rhynsburger, D. (1973). Analytic delineation of Thiessen polygons. *Geographical Analysis,* 5(2), 133-144.

Riestenberg, M. M. (1994). Anchoring of thin colluvium by roots of sugar maple and white ash on hillslopes in Cincinnati *(Vol. 2059)*. US Government Printing Office.

Rigon, R., Bertoldi, G., & Over, T. M. (2006). GEOtop: A distributed hydrological model with coupled water and energy budgets. *Journal of Hydrometeorology*, 7(3), 371-388.

Ritter, J. B. (2004). Landslide and slope stability analysis: using an infinite slope model to delineate areas susceptible to translational sliding in the cincinnati, oh area, computational science module, dept. of geol. Wittenberg U., Springfield, OH.

Romero, E., Gens, A., & Lloret, A. (1999). Water permeability, water retention and microstructure of unsaturated compacted Boom clay. *Engineering Geology*, 54(1-2), 117-127.,

Rossi, G. (2010). A physically based distributed slope stability simulator to analyze shallow landslides triggering in real time and on a large scale. *Doctoral dissertation*, University of Florence.

Rossi, G., Catani, F., Leoni, L., Segoni, S., & Tofani, V. (2013). HIRESSS: a physically based slope stability simulator for HPC applications. *Natural Hazards and Earth System Sciences*, 13(1), 151-166.

Rouse Jr, J., Haas, R. H., Schell, J. A., & Deering, D. W. (1974). Monitoring vegetation systems in the Great Plains with ERTS. *NASA special publication*, 351, 309.

Salciarini, D., Fanelli, G., & Tamagnini, C. (2017). A probabilistic model for rainfall—induced shallow landslide prediction at the regional scale. *Landslides*, 14(5), 1731-1746.

Salciarini, D., Godt, J. W., Savage, W. Z., Conversini, P., Baum, R. L., & Michael, J. A. (2006). Modeling regional initiation of rainfall-induced shallow landslides in the eastern Umbria Region of central Italy. *Landslides*, 3(3), 181.

Salciarini, D., Tamagnini, C., Conversini, P., & Rapinesi, S. (2012). Spatially distributed rainfall thresholds for the initiation of shallow landslides. *Natural hazards*, 61(1), 229-245.

Salvatici, T., Tofani, V., Rossi, G., D'Ambrosio, M., Stefanelli, C. T., Masi, E. B., Rosi, A., Pazzi, V., Vannocci, P., Petrolo, M., Catani, F., Ratto, S., Stevenin, H., & Casagli, N. (2018). Application of a physically based model to forecast shallow landslides at a regional scale. *Natural Hazards and Earth System Sciences*, 18(7), 1919-1935.

Sassa, K. (1984). The mechanism starting liquefied landslides and debris flows. *Proc. 4th Int. Sym. on Landslides, Toronto, Canada*, 1984, 2, 349-354.

Sassa, K. (1985). The mechanism of debris flows. In Proc. *XI Int'l Conf. on Soil Mechanism and Foundation Engineering,* (Vol. 3, pp. 1173-1176).

Scanlan, C. A., & Hinz, C. (2010, August). Insights into the processes and effects of root-induced changes to soil hydraulic properties. In *2010 19th World Congress of Soil Science, Soil Solutions for a Changing World* (pp. 1-6).

Schenk, H. J., & Jackson, R. B. (2002). Rooting depths, lateral root spreads and below-ground/above-ground allometries of plants in water-limited ecosystems. *Journal of Ecology*, 90(3), 480-494.

Schmidt, K. M., Roering, J. J., Stock, J. D., Dietrich, W. E., Montgomery, D. R., & Schaub, T. (2001). The variability of root cohesion as an influence on shallow landslide susceptibility in the Oregon Coast Range. *Canadian Geotechnical Journal*, 38(5), 995-1024.

Scholl, P., Leitner, D., Kammerer, G., Loiskandl, W., Kaul, H. P., & Bodner, G. (2014). Root induced changes of effective 1D hydraulic properties in a soil column. *Plant and soil*, 381(1-2), 193-213.

Schwarz, M., Cohen, D., & Or, D. (2010). Root-soil mechanical interactions during pullout and failure of root bundles. Journal of Geophysical Research: *Earth Surface*, 115(F4).

Selby, M. J. (1982). Hillslope materials and processes. Oxford University Press, Oxford, (480).

Sidle, R. C., & Swanston, D. N. (1982). Analysis of a small debris slide in coastal Alaska. *Canadian Geotechnical Journal*, 19(2), 167-174.

Simoni, S., Zanotti, F., Bertoldi, G., & Rigon, R. (2008). Modelling the probability of occurrence of shallow landslides and channelized debris flows using GEOtop-FS. *Hydrological Processes: An International Journal*, 22(4), 532-545.

Stokes, A., & Mattheck, C. (1996). Variation of wood strength in tree roots. *Journal of Experimental Botany*, 47(5), 693-699.

Stokes, A., Atger, C., Bengough, A. G., Fourcaud, T., & Sidle, R. C. (2009). Desirable plant root traits for protecting natural and engineered slopes against landslides. *Plant and soil*, 324(1-2), 1-30.

Stone, E. L., & Kalisz, P. J. (1991). On the maximum extent of tree roots. *Forest Ecology and Management*, 46(1-2), 59-102.

Subedi, K. D., Ma, B. L., & Liang, B. C. (2006). New method to estimate root biomass in soil through root-derived carbon. *Soil Biology and Biochemistry*, 38(8), 2212-2218.

Takahashi, T. (1981). Debris flow. *Annual review of fluid mechanics*, 13(1), 57-77.

Taleisnik, E., Peyrano, G., Cordoba, A., & Arias, C. (1999). Water retention capacity in root segments differing in the degree of exodermis development. *Annals of Botany*, 83(1), 19-27.

Terlien, M. T. (1998). The determination of statistical and deterministic hydrological landslide-triggering thresholds. *Environmental geology*, 35(2-3), 124-130.

Todd, S. W., Hoffer, R. M., & Milchunas, D. G. (1998). Biomass estimation on grazed and ungrazed rangelands using spectral indices. *International journal of remote sensing*, 19(3), 427-438.

Tofani, V., Bicocchi, G., Rossi, G., Segoni, S., D'Ambrosio, M., Casagli, N., & Catani, F. (2017). Soil characterization for shallow landslides modeling: a case study in the Northern Apennines (Central Italy). *Landslides*, 14(2), 755-770.

Tofani, V., Dapporto, S., Vannocci, P., & Casagli, N. (2006). Infiltration, seepage and slope instability mechanisms during the 20-21 November 2000 rainstorm in Tuscany, central Italy. *Natural Hazards and Earth System Sciences* 6 1025– 1033

Tosi, M. (2007). Root tensile strength relationships and their slope stability implications of three shrub species in the Northern Apennines (Italy*). Geomorphology,* 87(4), 268-283.

Traoré, O., Groleau-Renaud, V., Plantureux, S., Tubeileh, A., & Boeuf-Tremblay, V. (2000). Effect of root mucilage and modelled root exudates on soil structure. *European journal of soil science*, 51(4), 575-581.

Tsai, T. L. (2008). The influence of rainstorm pattern on shallow landslide. *Environmental Geology*, 53(7), 1563-1569

Tsai, T. L., & Yang, J. C. (2006). Modeling of rainfall-triggered shallow landslide. *Environmental Geology*, 50(4), 525-534;

Van Genuchten, M. T. (1980). A closed-form equation for predicting the hydraulic conductivity of unsaturated soils 1. *Soil science society of America journal*, 44(5), 892-898.

Vanapalli, S. K., Fredlund, D. G., Pufahl, D. E., & Clifton, A. W. (1996). Model for the prediction of shear strength with respect to soil suction. *Canadian Geotechnical Journal*, 33(3), 379-392.

Veenhof, R., & Wu, W. (2019). Behaviour of Reinforced Sand with Synthetic Fibres in a Centrifuge. *In Recent Advances in Geotechnical Research* (pp. 197-209). Springer, Cham.

Vergani, C., & Graf, F. (2016). Soil permeability, aggregate stability and root growth: a pot experiment from a soil bioengineering perspective. *Ecohydrology*, 9(5), 830-842.

Waldron, L. J. (1977). The shear resistance of root-permeated homogeneous and stratified soil 1. *Soil Science Society of America Journa*l, 41(5), 843-849.

Waldron, L. J., & Dakessian, S. (1981). Soil reinforcement by roots: calculation of increased soil shear resistance from root properties. *Soil science*, 132(6), 427-435.

Wieczorek, G. F. Landslide triggering mechanisms in Turner, AK and Schuster, RL (eds.), 1996, Landslides Investigation and Mitigation, Special Report 247. *Transportation Research Board, National Research Council, Washington, DC*, 672p, 8.

Wu, T. H., McKinnell III, W. P., & Swanston, D. N. (1979). Strength of tree roots and landslides on Prince of Wales Island, Alaska. *Canadian Geotechnical Journal*, 16(1), 19-33.

Wu, W., & Sidle, R. C. (1995). A distributed slope stability model for steep forested basins. *Water resources research*, 31(8), 2097-2110.

Zêzere, J. L., de Brum Ferreira, A., & Rodrigues, M. L. (1999). The role of conditioning and triggering factors in the occurrence of landslides: a case study in the area north of Lisbon (Portugal). *Geomorphology*, 30(1-2), 133-146.

Zêzere, J., Trigo, R. M., & Trigo, I. F. (2005). Shallow and deep landslides induced by rainfall in the Lisbon region (Portugal): assessment of relationships with the North Atlantic Oscillation. *Natural Hazards and Earth System Sciences*, 5(3), 331-344.

Zhang, C., Chen, L., Jiang, J., & Zhou, S. (2012). Effects of gauge length and strain rate on the tensile strength of tree roots. *Trees*, 26(5), 1577-1584.